ANUL XLII **1997**

S T U D I A
UNIVERSITATIS BABEŞ-BOLYAI
PHYSICA
2

Editorial Office: 3400 CLUJ-NAPOCA, Gh. Bilaşcu no.24 ♦ Tel. 194315; int. 167

SUMAR - CONTENTS - SOMMAIRE

I. Solid State Physics

II. Spectroscopy

III. Theoretical Physics

IV. Liquid State Physics

STUDIA UNIVERSITATIS BABEŞ-BOLYAI,PHYSICA, XLII, 2, 1997

EPR AND MAGNETIC SUSCEPTIBILITY INVESTIGATIONS OF TeO_2-B_2O_3-SrO-Fe_2O_3 GLASSES

I. ARDELEAN[1], M. PETEANU[1], V. SIMON[1], F. CIORCAS[1]

ABSTRACT. Glasses of the $xFe_2O_3\cdot(100-x)[70TeO_2\cdot25B_2O_3\cdot5SrO]$ system were investigated by means of electron paramagnetic resonance (EPR) and magnetic susceptibility measurements, within $0 < x \leq 20$ mol %. Several structural units involving Fe^{3+} ions were revealed. Fe^{2+} ionic species were also detected within $1 \leq x \leq 20$ mol %. Isolated Fe^{3+} ions in sites of strongly distorted octahedral symmetry, and clustered formations containing both Fe^{3+} and Fe^{2+} species were evidenced.

1. INTRODUCTION

Structural investigation of vitreous matrices may be performed by means of EPR of paramagnetic ions. Among the most thoroughly studied probes in glasses are Fe^{3+} ions, their EPR spectra being typified by the resonance lines at $g \approx 4.3$ and 2.0 that arise from the isotropic transitions within the Kramers doublets [1-4]. Several site symmetries of the Fe^{3+} ions reveal as appropriate to split the $^6S_{5/2}$ state ground level into three doublets. General conditions for the occurrence of an isotropic g-tensor with value of 4.3 were obtained in terms of the spin-Hamiltonian parameters for high-spin d^5 systems [5-10].

The magnetic behaviour of iron ions in vitreous systems was studied to determine the type and strength of interactions involving them and their valence state on various compositional ranges [11-18].

Our interest in the tellurite systems study [16-18] concerns now the $70TeO_2\cdot25B_2O_3\cdot5SrO$ one. Iron ions were chosen as probes in exploing the structure and properties of this vitreous system. The paper

---

[1] Faculty of Physics, Babeş-Bolyai University, 3400 Cluj-Napoca, Romania

aims to present our data obtained by means of EPR and magnetic susceptibility investigations.

2. EXPERIMENTAL

Glasses of the system xFe_2O_3·(100-x)[70TeO_2·25B_2O_3·5SrO] were prepared for $0 \leq x \leq 20$ mol %. Pure reagent TeO_2, H_3BO_3, $SrCO_3$ and Fe_2O_3 were used. The melting was performed in an electrical furnace at 1000°C, during 10 minutes. Sintered corundum crucibles were used. The quenching was performed at room temperature by pouring the molten material on a stainless steel plate. Typical glasses were obtained having the characteristic coloration corresponding to iron ions.

The structure of samples was tested by means of X-ray diffraction analysis. Crystalline phases were not detected up to 20 mol% Fe_2O_3.

EPR measurements were performed at room temperature with a JEOL-type spectrometer, in the X frequency band (9.45 GHz), with a 100 kHz field modulation.

Magnetic susceptibility measurements were realised by using a Faraday-type balance, in the temperature range of 80-300 K.

3. RESULTS

3.1. EPR investigations

Electron paramagnetic resonance spectra typical for Fe^{3+} ($3d^5$) paramagnetic ions were obtained (Fig. 1). They attest the presence of iron ions in the (3+) valence state for all the investigated samples. The spectra structure mainly consists in absorption lines centered at $g \approx 4.3$ and $g \approx 2.0$. Their prevalence and characteristics (line-width, intensity) depend on the Fe_2O_3 content of the sample and reflect the Fe^{3+} ions distribution on different structural units building the matrix. Unresolved lines of low relative intensity were also detected at $g \approx 9.7$ for samples with low Fe_2O_3 content.

The absorption lines evolution when increasing x concentration was revealed by following the concentration dependence of the EPR parameters, namely the line-width ΔH, and intensity approximated as $J = I \cdot (\Delta H)^2$, where I is the absorption line amplitude. The line-width ΔH, of the $g \approx 4.3$ absorption line increases within $0.3 \leq x \leq 10$ mol % evidencing dipolar broadening (Fig. 2.a). The slope of the

ΔH = f(x) curve changes at about 1 mol % Fe_2O_3 as a result of decreasing number of ions implied in dipolar interactions. This observation is supported by the line-intensity evolution (Fig. 2b). The intensity of the g ≈ 4.3 absorption line increases within a short concentration range ($0.3 \leq x \leq 1$ mol % Fe_2O_3), abruptly decreases for $x > 1$ mol % and vanishes for samples with $x > 10$ mol % (Fig. 2.b). The g ≈ 4.3 absorption failure reflects changes in the matrix structure occurred at rising concentration.

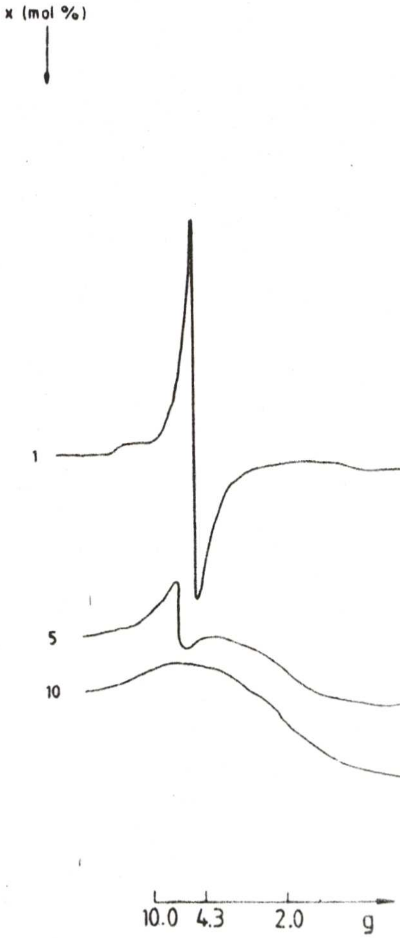

Fig. 1. Some representative EPR absorption spectra of Fe^{3+} ions in $xFe_2O_3\cdot(100-x)[70TeO_2\cdot25B_2O_3\cdot5SrO]$ glasses

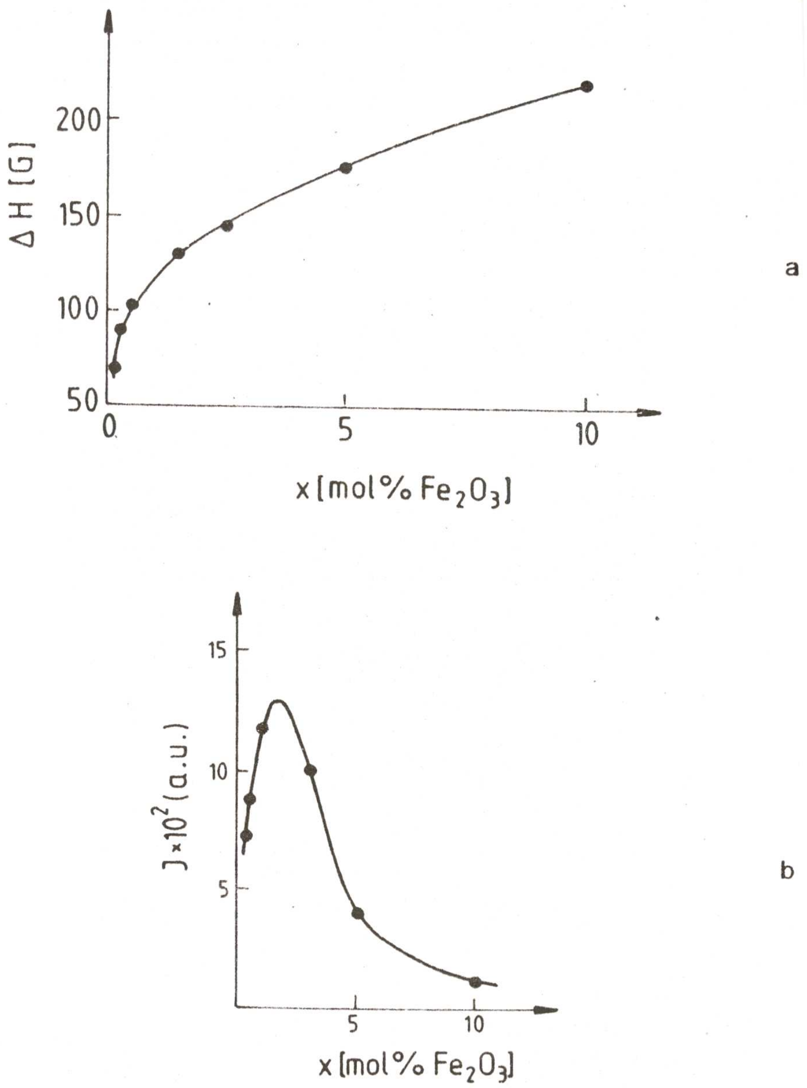

Fig. 2. Concentration dependence of the g ≈ 4.3 line-width (a) and line-intensity (b)

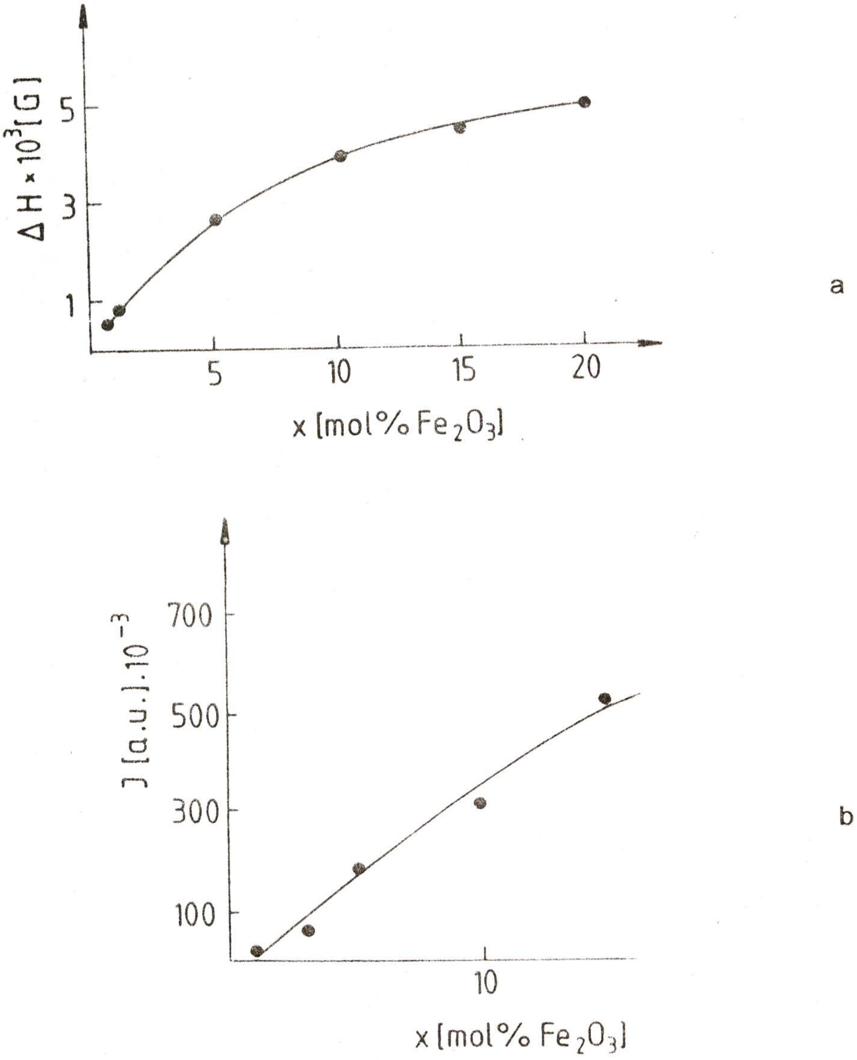

Fig. 3. Concentration dependence of the $g \approx 2.0$ line-width (a) and line-intensity (b)

The line-width corresponding to the $g \approx 2.0$ resonance line show an increasing within $1 \leq x \leq 20$ mol % Fe_2O_3 but its evolution reflects the competition between the broadening mechanisms (dipolar broadening and interactions between ions in mixed valence states) and narrowing mechanisms (superexchange interactions) (Fig. 3.a). The intensity of the line increases without following linearly the Fe_2O_3 content of the sample. The increasing is attenuated mainly for samples having x > 5 mol % Fe_2O_3 (Fig. 3.b). This suggests (2+) valence states of iron progressively entering the matrix during the impurifying process. These ionic species do not show resonance absorption but may affect the Fe^{3+} paramagnetic ions spectra when interact together.

3.2. Magnetic susceptibility data

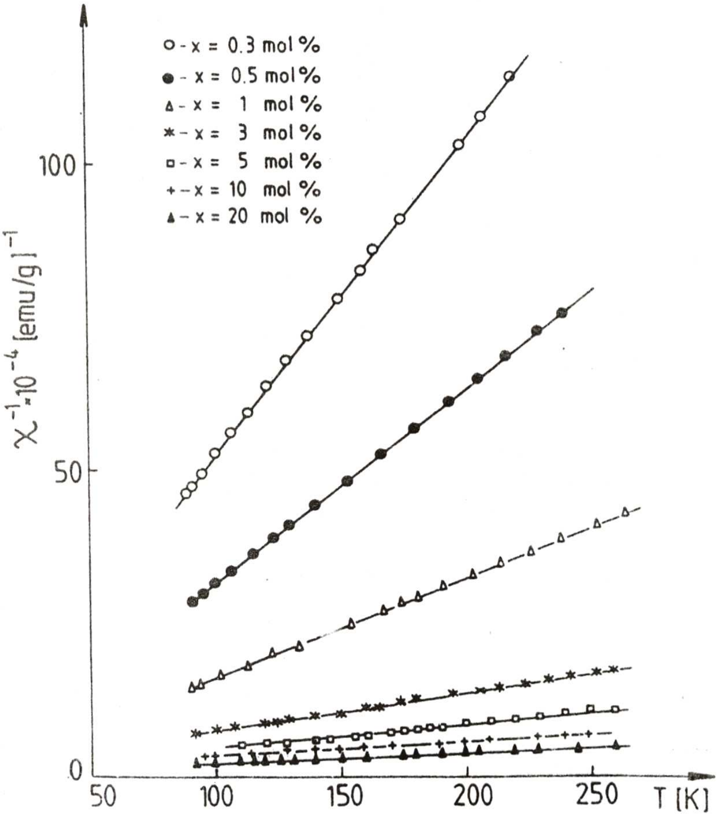

Fig. 4. Temperature dependence of the reciprocal magnetic susceptibility of several glasses of the $xFe_2O_3 \cdot (100-x)[70TeO_2 \cdot 25B_2O_3 \cdot 5SrO]$ vitreous system

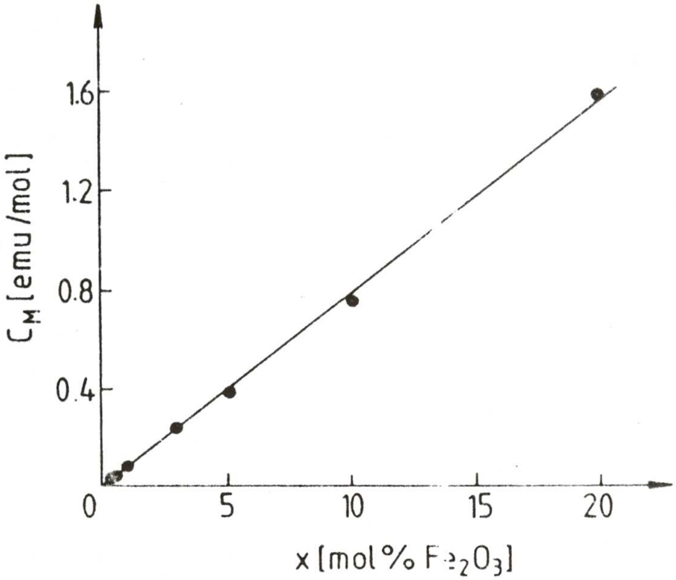

Fig. 5. Concentration dependence of the molar Curie constants

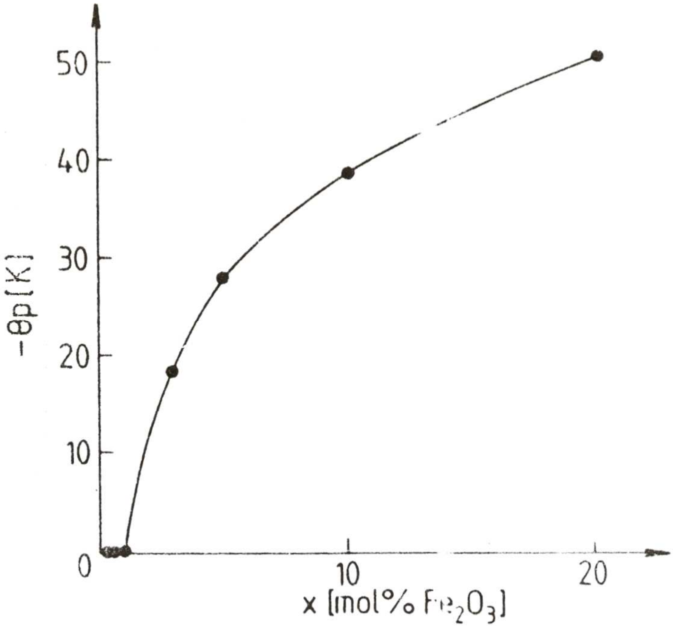

Fig. 6. Concentration dependence of the paramagnetic Curie temperature

The temperature dependence of the reciprocal magnetic susceptibility (Fig.4) show a Curie type behaviour, $\chi = C/T$, for samples with $x \leq 1$ mol % Fe_2O_3, typical for magnetic ions involved only in dipole-dipole interactions, which do not participate at exchange interactions. For $x > 1$ mol % the Curie-Weiss law, $\chi = C/(T-\theta_p)$, is obeyed with negative paramagnetic Curie temperature, θ_p. This behaviour is characteristic for antiferromagnetically coupled ions by means of superexchange interactions. By using the $1/\chi = f(T)$ dependence the molar Curie constant, C_M, was calculated for each sample. According to Fig. 5 the C_M values increase with the Fe_2O_3 content but for samples with $x > 1$ mol % Fe_2O_3 the obtained C_M have values comprised between the two extrema calculated by supposing that all iron ions are in the (2+) valence state or in the (3+) one. This results suggest the Fe^{3+} and Fe^{2+} ionic species simultaneously present in our samples. The molar fractions of iron ions in these two valence states were calculated in first approximation by using the equations:

$$x\mu_{exp}^2 = x_1\mu_{Fe^{3+}}^2 + x_2\mu_{Fe^{2+}}^2 ,$$
$$x = x_1 + x_2 ,$$

where $\mu_{exp}=2.83(C_M/2x)^{1/2}$ is the effective magnetic moment obtained from experimental data; x_1 and x_2 are the molar fractions of the iron ions in the (3+) and (2+) valence states; $\mu_{Fe^{3+}}$ and $\mu_{Fe^{2+}}$ were approximated by the values corresponding to free states of these ions, namely $\mu_{Fe^{3+}} = 5.92\mu_B$ and $\mu_{Fe^{2+}} = 4.90\mu_B$ which usually is accepted in glasses or paramagnetic salts. The obtained data are given in Table 1. The x_1 and x_2 values increase with increasing Fe_2O_3 content but their proportion differs. For $x \geq 10$ mol % the x_2/x ratio value exceeds 0.5 showing the prevalence of Fe^{2+} ionic species. By comparing this behaviour to that detected for $70TeO_2 \cdot 25B_2O_3 \cdot 5PbO$ glasses previously studied [17] we observe a more pronounced tendency in accumulating the Fe^{2+} species when rising the Fe_2O_3 content in lead containing samples. According to [17] the values of x_2/x increase from 0.53 to 0.60 within $3 \leq x \leq 20$ mol %.

Table 1.

Molar fractions of Fe^{3+} and Fe^{2+} ions in glasses of the system Fe_2O_3-TeO_2-B_2O_3-SrO.

x [mol % Fe_2O_3]	x_1 $\left[mol\% Fe_2^{3+}O_3\right]$	x_2 $\left[mol\% Fe_2^{2+}O_3\right]$	x_2/x
0.3	0.30	-	-
0.5	0.50	-	-
1.0	0.83	0.13	0.13
3.0	2.20	0.80	0.26
5.0	3.20	1.80	0.36
10.0	4.70	5.30	0.53
20.0	7.00	13.0	0.65

The absolute value of paramagnetic Curie temperature increases for x > 1 mol % Fe_2O_3 (Fig. 6) reflecting the increasing of the exchange integral when rising the paramagnetic ions concentration in the matrix.

The data agree with those obtained by means of EPR as will be described below.

4. DISCUSSIONS

The $g \approx 4.3$ absorption line is due to isolated paramagnetic ions, in distorted octahedral symmetric sites, subjected to strong crystal field effects. This resonance line may result due to transitions between the median Kramers doublet lines when the site symmetry is rhombic [1-4] or the transition may be induced between the lines of the lowest doublet, in the case of tetragonal sites [8] or cubic tetragonally distorted sites [9, 10]. When the site symmetry is rhombic the transitions inside the extra Kramers doublets (when populated) result in anisotropic absorption lines at $g_{eff} \approx 0.608; 9.677; 0.857$ values. According to Fig. 1 the $g \approx 4.3$ absorption line is accompanied by the feature at $g \approx 9.7$ which has low intensity relative to that at $g \approx 4.3$ due to its anisotropy.

The evolution of the $g \approx 9.7$ line, in the low concentrations range is similar to that of the $g \approx 4.3$ line, and have the origin in the same ionic environment. The paramagnetic Fe^{3+} ions in site of rhombic symmetry seems, therefore, to have the major contribution to absorptions resulting in $g \approx 4.3$ lines of our spectra. According to the evolution of the EPR parameters corresponding to the $g \approx 4.3$ resonance line (Fig. 2) there is a relatively narrow range of concentration where the above specified structural units involving Fe^{3+} ions may really exist as distinct and independent configurations.

Absorption lines at $g \approx 2.0$ are due to paramagnetic Fe^{3+} in slightly distorted structural units at very low Fe_2O_3 content (up to 1 mol%) and clustered formations for higher concentrations. The mixed valence states revealed by magnetic investigations explain both the EPR parameters dependence of the resonance line whith increasing concentration (Fig. 3) and the magnetic behaviour of samples. The Fe^{3+} - Fe^{2+} interactions are broadening mechanisms for the EPR absorption line [19]. According to Table 1 there are large amounts of Fe^{2+} ions for $x \geq 10$ mol % Fe_2O_3. Consequently the line-width broadening due to dipolar interactions and Fe^{3+} - Fe^{2+} interactions is appreciable. This broadening is balanced by the superexchange mechanisms evidenced by means of magnetic investigations, due to the antiferomagnetically coupled pairs of Fe^{3+} ions and to Fe^{3+} - Fe^{2+} pairs. The increasing amount of Fe^{2+} ionic species explains the poor effect of rising the Fe_2O_3 content on the line-intensity (Fig. 3.b).

5. CONCLUSIONS

Glasses of the $xFe_2O_3 \cdot (100-x)[70TeO_2 \cdot 25B_2O_3 \cdot 5SrO]$ system show EPR absorption spectra due to Fe^{3+} ions, within $0 < x \leq 20$ mol %.

Magnetic measurements revealed Fe^{3+} ions as simultaneously present with the Fe^{2+} ions, for $1 \leq x \leq 20$ mol %. The Fe^{2+} species are preponderant in samples with $x \geq 10$ mol % .

Isolated Fe^{3+} ions in rhombically distorted octahedral sites subjected to strong crystal field effects were detected up to 5 mol % Fe_2O_3. Clustered formations containing both Fe^{3+} and Fe^{2+} ions were detected within $1 \le x \le 20$ mol %. Superexchange interactions for the antiferromagnetically coupled Fe^{3+} - Fe^{3+} and Fe^{3+} - Fe^{2+} pairs were evidenced. Mechanisms due to the Fe^{3+} - Fe^{2+} interactions explain the particular evolution of the EPR parameters of the absorption lines.

REFERENCES

1. T.Castner, G.S.Newell, W.C.Holton, C.P.Slichter, J. Chem. Phys. 32, 668 (1960).
2. H.H.Wickman, M.P.Klein, D.A.Shirley, J. Chem. Phys. 42, 2113 (1965).
3. R.W.Kedzie, D.H.Lyons, M.Kestigian, Phys. Rev. 138A, 918 (1965).
4. D.Loveridge, S.Parke, Phys. Chem. Glasses 12, 19 (1971).
5. D.L.Griscom, R.E.Griscom, J. Chem. Phys. 47, 2711 (1967).
6. R.D.Dowsing, J.F.Gibson, J. Chem. Phys. 50, 294 (1969).
7. M.Ya Shcherbakova, V.E.Istomin, Phys. Stat. Sol. (b) 67, 461 (1975).
8. M.Peteanu, Al.Nicula, Studii şi Cercet. de Fizică 33(1), 29 (1981); ibid 34(1), 15 (1982).
9. V.Cerny, B.Petrova, M.Frumar, J. Non-Cryst. Solids 125, 17 (1990).
10. V.Cerny, B.Frumarova, J.Rosa, I.L.Licholit, M.Frumar, J. Non-Cryst. Solids 192 & 193, 165 (1995).
11. G.Sperlich, P.Urban, Phys. Stat. Sol. (b) 61, 475 (1974).
12. E.J.Friebele, N.C.Koon, L.K.Wilson, D.L.Kinser, J. Ceram. Am. Soc. 57, 237 (1974).
13. I.Ardelean, E.Burzo, I.Pop, *Solid State Commun*. 23, 211 (1977).
14. B.Kumar, C.H.Chen. J. Appl. Phys. 75, 6760 (1994).
15. E.Burzo, I.Ardelean, *Phys. Chem. Glasses* 20, 15 (1979).
16. I.Ardelean, Gh.Ilonca, O.Cozar, G.Mureşan, Studia Univ. Babes-Bolyai, *Physica* 2, 37 (1989)
17. I.Ardelean, M.Peteanu, S.Filip, V.Simon, G.Györffy, *Solid State Commun.* 102, 4 (1997)
18. M.Peteanu, I.Ardelean, V.Simon, S.Filip, G.Györffy, Studia Univ. Babes-Bolyai, Physica 1, 17 (1996)
19. C.Kittel, E.Abrahams, Phys. Rev. 90, 238 (1963).

STUDIA UNIVERSITATIS BABEŞ-BOLYAI, PHYSICA, XLII, 2, 1997

MAGNETIC AND RAMAN SPECTROSCOPIC BEHAVIOR OF $0.10[xGd_2O_3(1\text{-}x)Y_2O_3]\cdot 0.90Na_2B_4O_7$ GLASSES

E. CULEA[1], R. ORDEAN[2], T. RISTOIU[1], I. MILEA[1], I. CHICINAS[1]

ABSTRACT. Glasses of $0.10[xGd_2O_3(1\text{-}x)Y_2O_3]\ 0.90Na_2B_4O_7$ composition, with $0 \le x \le 1$, were investigated using electron paramagnetic resonance (EPR), magnetic susceptibility and Raman spectroscopic measurements. EPR spectra were obtained due to the presence of Gd^{3+} ions in the studied glasses. These ions are distributed in low symmetry sites in the host glass matrix. Weak antiferromagnetic interactions take place between the Gd^{3+} ions, as shown by the magnetic susceptibility data. Raman spectroscopic features change by modifying the Gd_2O_3/Y_2O_3 content of the glasses evidentiating the network modifying role of the gadolinium and yttrium ions.

INTRODUCTION

Glasses containing rare earth ions has been extensively studied in the past two decays due to their important optical, magnetic and mechanical properties [1]. Considerable interest was accorded to glasses containing gadolinium ions. Recent electron paramagnetic resonance (EPR) and magnetic susceptibility investigations reveal important aspects concerning the distribution of the gadolinium ions in the glass matrix and the nature of magnetic interactions between these ions [2-7]. Raman spectroscopic investigations performed on glasses containing gadolinium ions permited to obtain information concerning their basic structural groups and evidentiated the network modifier role played by the gadolinium ions in the host glass matrix [8-11].

---

[1] Technical University of Cluj-Napoca, Department of Physics, Romania
[2] Institute of Isotopic and Molecular Technology, Cluj-Napoca, Romania

In order to extend the available information concerning glasses containing gadolinium ions, in this work we investigated the $0.10[xGd_2O_3(1\text{-}x)Y_2O_3]\ 0.90Na_2B_4O_7$ glass system with $0 \leq x \leq 1$ using EPR, magnetic susceptibility and Raman spectroscopy measurements. This glass system is interesting because contains two type of rare earth ions, Gd^{3+} and Y^{3+}, which are expected to ocuppy the same sites in the glass matrix due to their similarity [2], but having a different magnetic behavior (magnetic for Gd^{3+} and diamagnetic for Y^{3+}).

EXPERIMENTAL

Samples of the $0.10[xGd_2O_3(1\text{-}x)Y_2O_3]\ 0.90Na_2B_4O_7$ composition (noted xGYB) with x = 0, 0,3, 0,5, 0,7 and 1 were obtained using reagent grade $Na_2B_4O_7\cdot 10H_2O$ (Reactivul, Romania), Gd_2O_3 and Y_2O_3 (Fluka, Switzerland). First, the base borate glass of $Na_2B_4O_7$. composition was prepared by melting dehydrated borax at 1000^{o}C for 1 hour. The melt was quenched on a refractory steel block. The obtained base glass was crushed and powdered. Appropriate amounts of Gd_2O_3, Y_2O_3 and base glass were mixed and milled in an agate ball mill for 2 hours. Then, the mixtures were melted at 1200^{o}C for 15 minutes. The glass samples were obtained by pouring the melts on stainless steel. Some of the samples, destinated to Raman spectroscopic investigation, were obtained as slabs (20x8x3 mm^3) by pouring the melts on stainless steel having an appropriate groove.

X-ray diffraction investigation of the samples did not reveal crystallyne phases.

Magnetic susceptibility measurements were performed on a Faraday type balance between 80 and 300 K.

EPR measurements were performed on a standard SE/X 2543 equipment in the X-band, at room temperature.

Raman spectra were recorded on a GDM 1000 double-monocromator instrument equipped with ILA 120-1 argon-ion laser. The emission line from 488nm was used for excitation. Spectra were scanned for a Raman shift of 400 to 1650cm^{-1}.

RESULTS AND DISCUSSION

The EPR spectra recorded for the xGYB glasses are due to the Gd^{3+} ions in the glass matrix [2-7]. Blank samples (no Gd^{3+} ions) of $Na_2B_4O_7$ and $0.10Y_2O_30.90Na_2B_4O_7$ compositions showed no EPR absorption at the gain levels used on the rest of the samples.

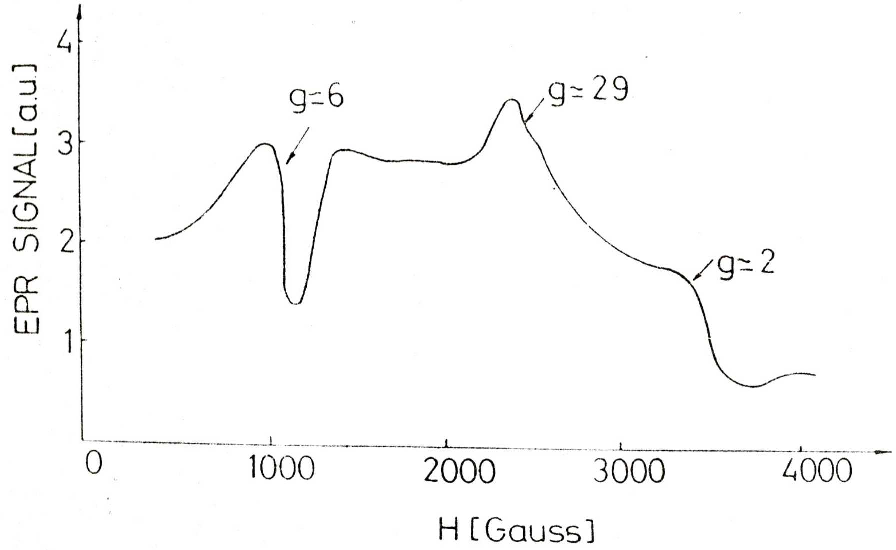

Fig. 1. The EPR spectrum of the xGYB glass with x=0.3.

Fig. 1 presents an EPR spectrum characteristic of xGYB glasses, namely that of the sample with x=0.3. This spectrum exhibits three proeminent features with effective g-values of 2, 2. 9 and 6, where g is defined by $g=h\nu/\mu_BH$, h is the Planck constant, ν is the microwave frequency, μ_B is the Bohr magneton and H is the value of the external applied magnetic field at the resonance line position. We note that the EPR features are broad leading to a large range of uncertainty in g value designation. Such spectra were previously reported for Gd^{3+} ions in different borate, phosphate and silicate glasses [2-7]. Some authors

[2-4, 6] suggested that the features appearing in the EPR spectra of the glasses containing gadolinium are due to Gd^{3+} ions located at sites with different symmetries. However, computer simulations have unambiguously shown that this type of EPR spectrum (Fig. 1) may originate from a S-state rare earth ion in a single low-symmetry glassy site with a broad and unimodal distribution of the spin-Hamiltonian term B^0_2, centered around 0.055 cm^{-1}, and a very broad distribution of the asymmetry parameters B^2_2 [5]. Such glassy sites correspond to a high coordination number estimated to be 8 or 9. Thus, even in homogeneous glass matrices there are possible different sites for the gadolinium ions because the vitreous matrices impose no specific site symmetry on the rare-earth ion having as result that the rare-earth ions can coordinate with a large number of irregular ligands. Thus the Gd^{3+} ions occupy in the glass matrix sites surrounded by polyhedra of more or less irregularly distributed ligands with high coordination numbers [5].

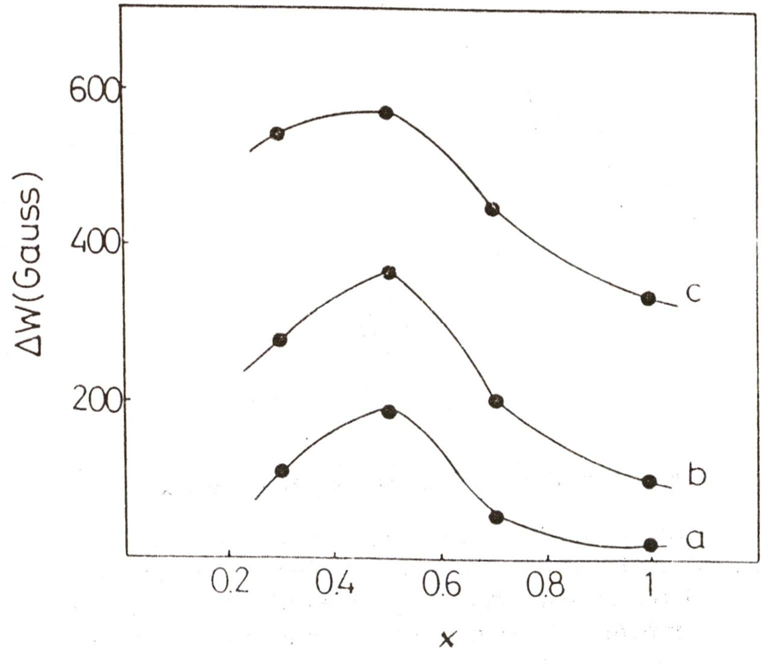

Fig. 2. Variation of the EPR linewidths ΔW of xGYB glasses as function of x where (a) corresponds to g≈6, (b) to g≈2. 9 and (c) to g≈2.

In several studies involving complex resonances of smaller paramagnetic ions (i. e. , Fe^{3+}, Mn^{2+}), the paramagnetic ions were found to be located at both network forming and network modifying sites. However, due to the large ionic radius of the Gd^{3+} ion ($r \approx 0.93$ Ĺ), it is unreasonable to assume that it can substitute for the smaller boron ion ($r \approx 0.20$ Ĺ) in the BO_3 or BO_4 structural units characteristic of the $Na_2B_4O_7$ glass. Thus, we assumed that in the xGYB glasses the Gd^{3+} ions occupy network modifying sites.

Fig. 2 presents the variation of the EPR linewidths ΔW of xGYB glasses as functions of x, where x is related to the Gd_2O_3 content of the samples, 0. 10x. Increasing x in the range of $0 < x \leq 0 .5$ produced the dipole-dipole broadening of the spectra, while for $x > 0.5$ produced the narrowing of the spectra due to exchange interactions.

Fig. 3 presents the dependence of the inverse magnetic susceptibility as function of temperature. The data collapse to straight lines indicating that the susceptibility per mole of magnetic ion follows a Curie-Weiss type behavior

$$\chi^{-1} =(T-\theta_p)/C \qquad (1)$$

where C is the molar Curie constant and θ_p is the paramagnetic Curie temperature. The solid lines in Fig. 3 represent the computer fit of experimental data according to relation (1). Parameters derived from the plot of χ^{-1} as a function of temperature, namely θ_p and μ_{eff} (the effective magnetic moment per gadolinium ion), are presented in Fig. 4. We mention that the μ_{eff} values were calculated using the experimentally determined C values.

The paramagnetic Curie temperature θ_p is a rough indicator of magnetic interaction between Gd^{3+} ions. In the case of Gd^{3+} ions, although the magnetic moment on the localized ion is large, the magnetic susceptibility measurements had shown that the interaction is weak($/\theta_p/ \leq 6$ K). The small negative values of θ_p (Fig. 4) suggest the weak antiferromagnetic nature of the interaction between Gd^{3+} ions. The antiferromagnetic nature of the interaction between the Gd ions is also supported by the μ_{eff} valies (Fig. 4) that are less than the magnetic moment of the free gadolinium ion, 7. 98 μ_B [12]. Note also that the effective gadolinium moments are not composition dependent for the studied scale of x values.

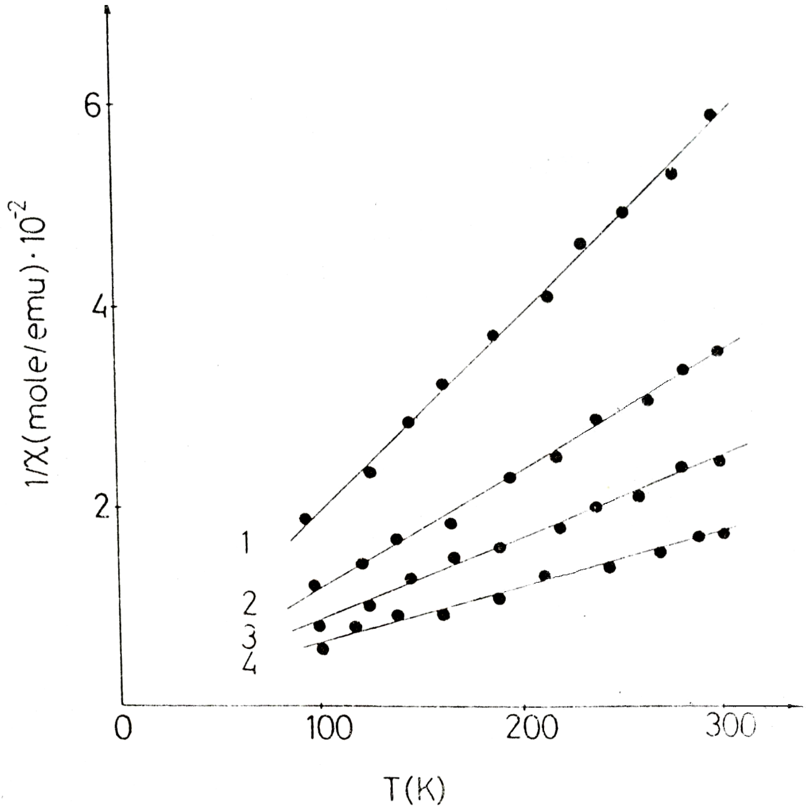

Fig. 3. Dependence of the inverse magnetic susceptibility of xGYB glasses as function of temperature, where (1) x=0. 3, (2) x=0.5, (3) x=0.7 and (4) x=1.

The EPR and magnetic susceptibility data obtained for the 0.10[xGd_2O_3(1-x)Y_2O_3] 0.90$Na_2B_4O_7$ glasses are in agreement with those previously reported for other glasses containing gadolinium ions [4-7].

Some of the representative Raman spectra obtained for the xGYB glasses are shown in Fig. 5. The main spectroscopic features evidentiated by these spectra are characteristic of alkali borate glasses. The spectrum of Fig. 5a corresponds to the base $Na_2B_4O_7$ glass and its spectroscopic features are close to those previously reported by Konijnendijk and Stevels[13] for this glass. Authors [13] established that the $Na_2B_4O_7$ glass network is mainly built up of diborate structural groups, but small number of metaborate and orthoborate groups and "loose" BO_3 and BO_4 structural units are probably present, too.

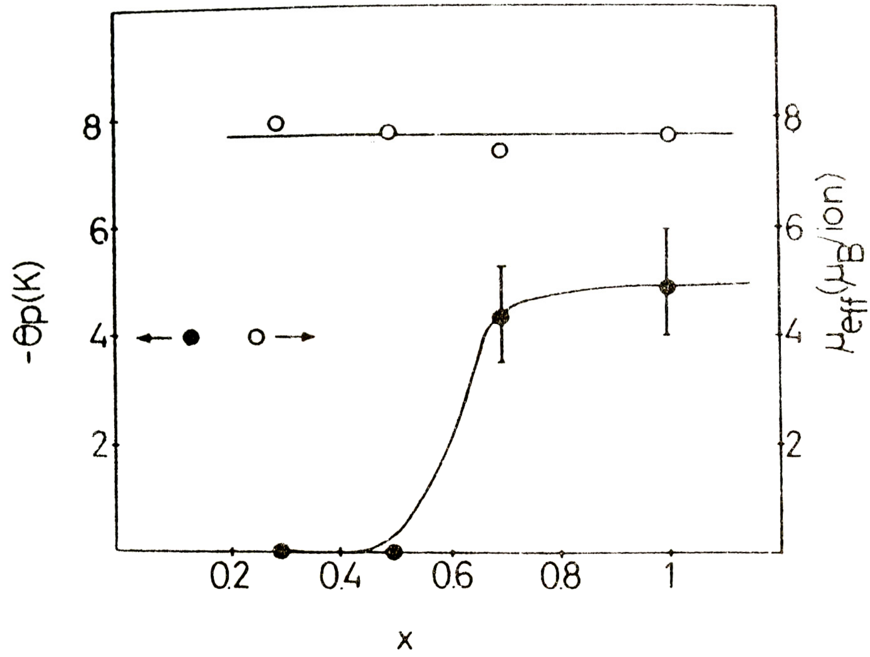

Fig. 4. Composition dependence of the Curie constant C and of the paramagnetic Curie temperature θ_p of xGYB glasses.

The Raman features evidentiated in the spectra recorded for the xGYB glasses were assigned as follows, based on previously published data:

- at 480÷490cm^{-1}, assigned to symmetric stretching vibration of "loose" BO_4 units[14];
- at 700÷730cm^{-1}, assigned to chain type metaborate groups[13];
- about 800cm^{-1} assigned to boroxol groups[13, 15, 16];
- at 910÷930cm^{-1}, assigned to asymmetric stretching vibration of "loose" BO_4 units[8];
- about 940cm^{-1}, assigned to orthoborate groups[15];

- at 1020÷1050cm^{-1}, assigned to diborate groups[13];
- about 1250cm^{-1}, assigned to boroxol groups[15];
- at 1310-1320cm^{-1}, assigned to B-O$^-$ vibrations[8];

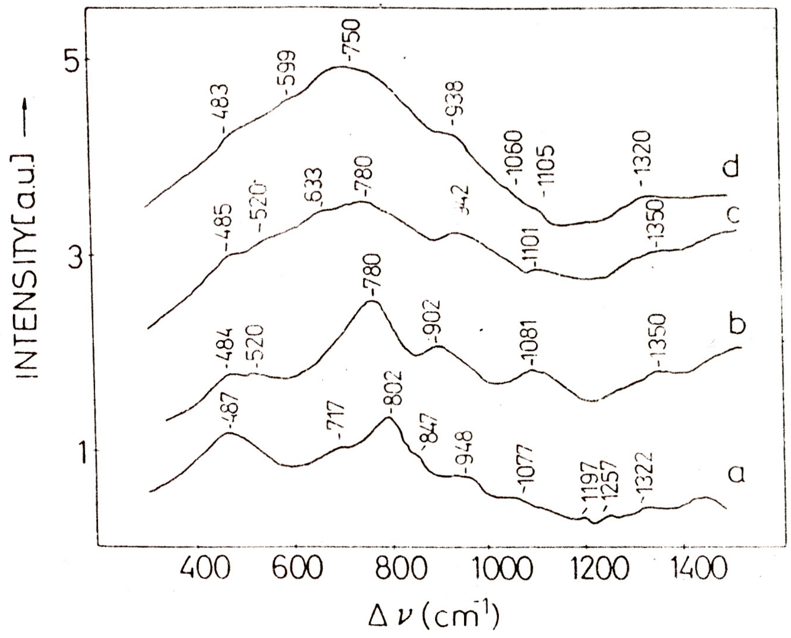

Fig. 5. Raman spectra of vitreous $Na_2B_4O_7$(a) and xGYB glasses with x=0. 3 (b), x=0. 5 (c) and x=1 (d).

Fig. 5 shows that increasing x (increasing the Gd_2O_3 content of the samples by replacing their Y_2O_3 content) generates changes of the spectral features. This is in agreement with the network modifier role that was previously reported for both Gd [9-11] and Y [11] ions in borate glasses.

Thus, the Raman bands at 480÷490cm^{-1} decrease with increasing x. This suggests the decrease of the number of BO_4 units with increasing x.

The Raman bands at about 717 cm^{-1}, 1020-1050cm^{-1} and 1250 cm^{-1} appears only in the spectrum of the base $Na_2B_4O_7$ glass but no in those of xGYB, suggesting that the xGYB glasses contain no metaborate, diborate and boroxol structural groups.

The Raman peak at 802 cm^{-1} decrease in intensity and shifts toward smaller $\Delta\nu$ values with increasing x, that may suggest a decrease of the number of boroxol groups.

The Raman peak at about 940cm^{-1} appears only for the samples with x= 0 and 1 suggesting that the samples with x=0.3, 0.5 and 0.7 contain no orthoborate structural groups.

The Raman peak at 1322 cm^{-1} was evidentiated for the base glass. Increasing x it will shift to 1350 cm^{-1} for x=0. 3 and 0. 5, while for x=1 is located to 1320 cm^{-1}. This may be interpreted considering that increasing x will modify the structural groups in the xGYB glasses leading to the modification of the length of B-O^- links, where O^- represents non-bridging oxygens.

CONCLUSIONS

The EPR investigation of the xGYB glasses indicated the presence of Gd^{3+} ions located at low-symmetry glassy sites having high coordination numbers.

Magnetic susceptibility and EPR measurements evidentiated that for $x \leq 0.05$ the Gd^{3+} ions behave as isolated species, while for $x > 0.05$ small antiferromagnetic interactions takes place between these ions.

Raman data prove that the Gd^{3+} and Y^{3+} ions play the role of network modifiers in the studied glasses.

REFERENCES

1. K. Moorjani, J. M. D. Coey, *Magnetic Glasses*, Elsevier Publishers, Amsterdam,1984.
2. R. C. Nicklin, J. K. Johnstone, R. G. Barnes, D. R. Wilder, *J. Chem. Phys*. 59 (1973) 1652.
3. M. A. Valente, S. K. Mendiratta, *Phys. Chem. Glasses* 33, 4 (1992) 149.
4. I. Ardelean, E. Burzo, D. Mitulescu-Ungur, S. Simion, *J. Non-Cryst. Solids* 146 (1992) 256.
5. B. Sreedhar, P. Indira, A. K. Bhatnagar, *Indian J. Pure & Appl. Phys*. 33 (1995) 353-356.
6. E. Culea, A. Pop, I. Cosma, *J. Magn. & Mag. Mat* 157/158 (1996) 163-164.

7. E. Culea, I. Milea, *J. Non-Cryst. Solids* 189 (1995) 246-250.
8. B. N. Meera, A. K. Sood, N. Chandrabhas, N. Ramakrishna, *J. Non-Cryst. Solids* 126, 224 (1990).
9. T. Iliescu, S. Simon, D. Maniu, I. Ardelean, *J. Mol. Structure* 294 (1993) 201.
10. T. Iliescu, I. Ardelean, S. Simon, *Solid State Commun*. 90, 8 (1994) 507.
11. I. Milea, E. Culea, T. Iliescu, *Balkan Phys. Let*. 2 (1994) 285.
12. E. Burzo*, Fizica Fenomenelor Magnetice,* vol. 1, Editura Academiei, 1979.
13. W. L. Konijnendijk, J. M. Stevels, *Borate Glasses*, Mat. Sci. Res. 1 2, 254 Plenum Press, New York (1977);Philips Res. Rep. Suppl. 1 (1975).
14. E. I. Kamitsos, M. A. Krakassides, G. D. Chryssikos, *J. Chem. Phys.* 91 (1983) 1073.
15. F. L. Galeener, G. Lucovsky, J. C. Mikkelsen, *Phys. Rev*. B 22, 8 (1980) 3983.
16. F. L. Galeener, *Solid State Commun*. 44 (1982) 1037.
17. E. I. Kamitsos, M. A. Krakassides, G. D. Chryssikos, *Phys. Chem. Glasses* 30 (1989) 229.

STUDIA UNIVERSITATIS BABEŞ-BOLYAI, PHYSICA, XLII, 2, 1997

UV VIS STUDY ON LEAD BORATE GLASSES INCORPORATING NEODYMIUM

I. ARDELEAN[1], I. MILEA[2], V. SIMON[1], S. ZAMFIRA[3]

ABSTRACT. $xNd_2O_3(100-x)[2B_2O_3\cdot PbO]$ glasses with $0 \le x \le 50$ mol % are investigated. Ultraviolet-visible absorption results regarding the effect of matrix as well as the effect of increasing Nd_2O_3 content on the room temperature absorption spectra are presented.

INTRODUCTION

Glasses containing trivalent lanthanide ions emmiting in the near infrared region are of current interest because of their potentiality as materials for high power lasers and optical amplifiers for fiber communications [1-5]. Oxide glasses have advantages of compositional diversity to optimise their physical properties [6]. It is well known that good quality borate glasses are produced easily and cheaply. The application of these glasses requires the evaluation of spectroscopic properties. This paper aims to report room temperature absorption results obtained in ultraviolet-visible (UV VIS) range from neodymium introduced in a lead-borate glass matrix, having in view that such a system could be interesting as laser medium or for other of the above mentioned applications.

EXPERIMENTAL

The investigated samples belong to $xNd_2O_3(100-x)[2B_2O_3\cdot PbO]$ glass system with $0 \le x \le 50$ mol %. They were obtained from reagent purity grade H_3BO_3, PbO and Nd_2O_3 in two stages. First was prepared the

---

[1] Babeş-Bolyai Unbiversity, Faculty of Physics, 3400 Cluj-Napoca, Romania

[2] Technical University, Department of Physics, 3400 Cluj-Napoca, Romania

[3] Transilvania University, Department of Physics, 2200 Bra¿ov, Romania

$2B_2O_3 \cdot PbO$ glass matrix in sintered corundum crucibles directly introduced at 1250^oC in an electric furnace with superkanthal bars, maintained for 30 minutes at this temperature and quickly poured onto stainless steel plates at room temperature. The crushed matrix was mixed with Nd_2O_3 in corresponding amounts to obtain the desired compositions, then the resulting admixtures were introduced again at 1250^oC. After 30 minutes equilibration time at this temperature the samples were undercooled at room temperature. X-ray analysis carried out on the obtained samples by using the cooper radiation K_a (l=1. 54 Å) in the angular range from 3^o to 113^o did not reveal any crystalline phase. The room temperature absorption spectra were measured in the visible and ultraviolet regions by means of a Specord M-40 spectrometer on plate samples of identical diameter and approximately same thickens.

RESULTS AND DISCUSSION

The absorption spectra recorded in the wave number range from 10000 cm^{-1}to 30000 cm^{-1}for the lead borate glass matrix and for the investigated lead-borate glasses incorporating different contents of neodynium oxide are presented in Fig. 1. One remarks absorption lines at 11350, 12500, 13400, 14600, 16000, 17200, 19000, 19400, 21100, 21600, 23200, 26150, 27100, 27900 and 28550 cm^{-1}. A weak absorption line around 24000 cm^{-1} occurs only for samples containing more than 30 mol % Nd_2O_3. As may be observed the glass matrix gives rise to two very weak bands centered around 26150 and 27100 cm^{-1}. All the other bands are assigned to the neodymium ions. The ground state of Nd^{3+} ion is $^4I_{9/2}$. The assignments for the f Æ f transitions in the absorption spectrum obtained at room temperature from Nd^{3+} ions in a zinc-borate glass [5] are given in Table 1. The position of the bands recorded from the investigated samples are very close to that summarised in Table 1.

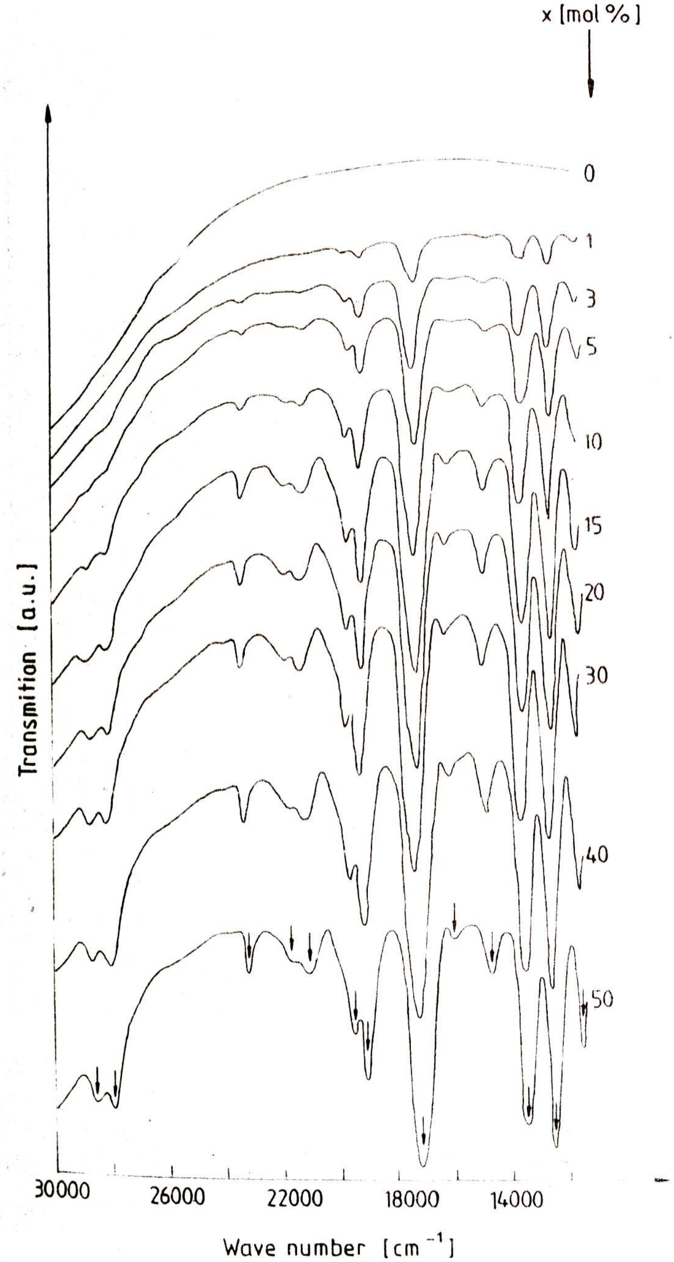

Fig. 1. UV VIS absorption spectra of $xNd_2O_3(100-x)[2B_2O_3\cdot PbO]$ glass samples.

Table 1

Assignement of the fÆf transitions in the absorption spectrum of Nd^{3+} ions in a borate glass matrix [5].

Excited state	Band center (cm^{-1})
$^4F_{3/2}$	11417
$^4F_{5/2}$, $^2F_{9/2}$	12465
$^4S_{3/2}$, $^4F_{7/2}$	13439
$^4F_{9/2}$	14686
$^2H_{11/2}$	15921
$^2G_{7/2}$, $^4G_{5/2}$	17186
$^2K_{13/2}$, $^4G_{7/2}$, $^4G_{9/2}$	19220
$^2K_{15/2}$, $^2G_{9/2}$, $^2(D,P)_{3/2}$,$^4G_{11/2}$	21366
$^2P_{1/2}$	23210
$^4D_{3/2}$, $^4D_{5/2}$, $^2I_{11/2}$,$^4D_{1/2}$,$^2L_{15/2}$	28216

The absorption bands obtained from the Nd_2O_3-B_2O_3-PbO glasses mainly correspond to the bands recorded from Nd_2O_3-B_2O_3-ZnO glasses. The difference is that instead of the absorption bands obtained in Nd_2O_3-B_2O_3-ZnO glass system at 19200 cm^{-1}, 21366 cm^{-1} and 28216 cm^{-1} for the Nd_2O_3-B_2O_3-PbO glasses were recorded doublets that consist of lines at 19000 cm^{-1} and 19400 cm^{-1}, 21100 cm^{-1} and 21600 cm^{-1}, respectively at 27900 cm^{-1} and 28550 cm^{-1}.

The position of the absorption bands from 13400 and 17200 cm^{-1} is the same for all samples in the investigated concentration range. The other bands are shifted to higher wave numbers as Nd_2O_3 content increases with the remark that the intense lines centered around 27900 cm^{-1} and 28550 cm^{-1} are shifted to larger wave numbers with increasing Nd_2O_3 content up to 30 mol % and come back to shorter wave numbers for $30 < x \leq 50$ mol %, as illustrated in Fig. 2.

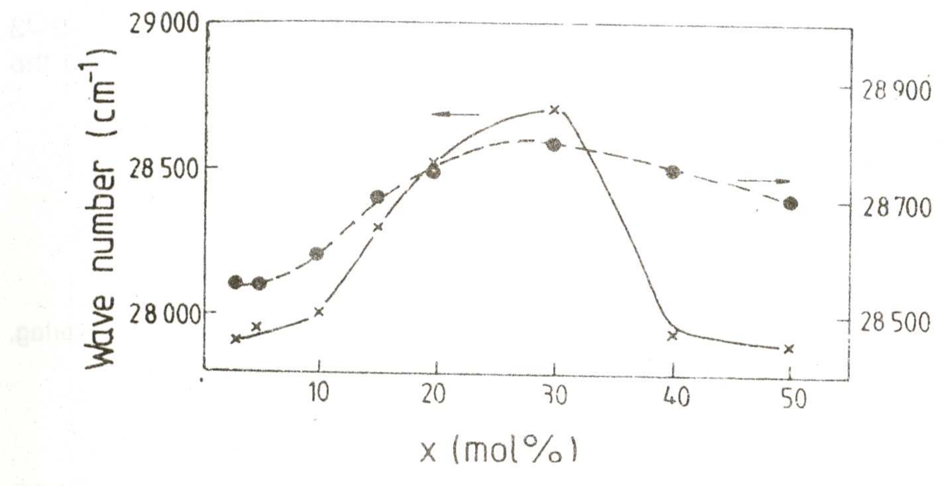

Fig. 2. Composition dependence of the shift of absorption lines centered around 27900 $^{cm-1}$(x) and 28550 $^{cm-1}$(∑).

The addition of Nd_2O_3 to lead- borate glasses [7] determines structural modifications in the glass samples. Due to the influence of the local crystalline field surrounding the lanthanide ions on their electronic shells and therefore on the radiative and nonradiative transition probabilities the optical properties of Nd^{3+} ions depend on the matrix wherein they are incorporated [8, 9].

CONCLUSIONS

The UV VIS absorption spectra of $xNd_2O_3(100-x)[2B_2O_3 \cdot PbO]$ glass samples consist of two very weak bands centered at 26150 cm^{-1} and 27100 cm^{-1} arising from the lead borate glass matrix and absorption lines around 11350, 12500, 13400, 14600, 16000, 17200, 19000, 19400, 21100, 21600, 23200, 26150, 27100, 27900 and 28550 cm^{-1} assigned to fÆf transitions of neodymium ions. The lines centered around 19000, 19400 cm^{-1} respectively 21100, 21600 cm^{-1} and 27900, 29500 cm^{-1} arise from absorption bands splited in doublet lines. Excepting the 13400 cm^{-1} and 17200 cm^{-1} bands all the other corresponding to the neodymium ions are shifted to higher wave numbers in the entire composition range when x increases, with the remark that the doublet of 27900 cm^{-1} and 28550 cm^{-1} exhibit an maximum for x = 30 mol %. The split of some absorption bands in doublet lines as well as the shift of the absorption bands as the Nd_2O_3 content increases denote the influence of the lead-borate matrix on the lanthanide ion.

REFERENCES

1. G. Fuxi, *Optical and Spectroscopic properties of Glass*, Springer Verlag, Shangai Scientific Technical Pub., Shanghai (1991).
2. M. J. Weber, *J. Non-Cryst. Solids*, 123, 208 (1990).
3. W. J. Miniscalco, J. Lightwave Technol., 9, 234 (1991).
4. J. D. Byun**,** B. H. Kim, K. S. Hong, J. H. Jung, S. W. Lee, K. S. Ryoo, A. A. Izyneev,V. B. Kravchenko, *Jpn. J. Appl. Phys.*, 33, 4907 (1994).
5. G. Pozza, D. Ajo, N. Bettinelli, A. Speghini, M. Casarin, *Solid State Commun.*, 97, 6, 521 (1996).
6. H. Takebe, T. Murata, H. Nishida, D. W. Hewak, K. Morinaga, *J. Cheram. Soc. Jap.*, 104, 3, 234 (1996).
7. T. Iliescu, I. Ardelean, V. Simon, D. Maniu, *J. Matt. Sci. Lett.*, 14, 393 (1995).
8. T. Kokubo, Y. Inaka, S. Sakka, *J. Non-Cryst. Solids,* 80, 518 (1986).
9. Y. Nageno, H. Takebe, K. Morinaga, *J. Am. Cheram. Soc.*, 76, 3081 (1993).

STUDIA UNIVERSITATIS BABEŞ-BOLYAI, PHYSICA, XLII, 2, 1997

LOCAL STRUCTURE INVESTIGATIONS OF SOME CU(II)-THEOPHYLLINE COMPLEXES

E. FORIZS[1], O. COZAR[2], L. DAVID[2],
D. RISTOIU[2], C. CRĂCIUN[2], C. BĂLAN[2]

ABSTRACT. The $CuT_2L_2 \cdot 2H_2O$ complexes [T=Theophylline (1,3-dimethylxanthine), L=NH_3, n-propylamine (npa] were prepared and investigated by IR and ESR spectroscopies. IR spectra indicate the coordination of the metallic ion at the N(7) atom of the theophylline and at the amine's nitrogen atoms. Powder ESR spectrum of $CuT_2(NH_3)_2 \cdot 2H_2O$ is axial (g_{II}=2. 255, $g_{\perp}$=2. 059). ESR spectrum of $CuT_2(npa)_2 \cdot 2H_2O$ is a superposition of one axial (g_{II}=2. 299, $g_{\perp}$=2. 064) and one isotropic component ($g_0 \approx$2. 100). The axial spectra of the former complexes are due to a static Jahn-Teller effect ($E_{JT} \approx 2880$ cm^{-1}). The local symmetries around the Cu(II) ions remain unchanged by DMF solvating, the adsorption of these solutions on NaY zeolite or by lowering the temperature.

INTRODUCTION

The copper (II) complexes with organic ligands are studied intensely in the last years owing to theirs medical implications [1]. The biological activity of these compounds is influenced by the manner in which the copper (II) ions coordinate the ligand's molecules. Theophylline (T=1,3-dimethylxantine) (Fig. 1) and their metallic complexes have an important role for the stimulation of the nervous centre and also in some cardiovascular issues. In previous papers, the theophylline (T=1,3-dimethylxantine) (Fig. 1) was studied as a model for guanine-metal ion interactions, of great importance in problems concerning the division and replication of DNA molecules [2,3].

In order to obtain further information on the local structure and the influence of the amine type in former compounds, we have prepared and

---

[1] Babeş-Bolyai Univ., Dept. of Chemistry, 3400 Cluj-Napoca, Romania
[2] Babeş-Bolyai Univ., Dept. of Physics, 3400 Cluj-Napoca, Romania

investigated the $CuT_2L_2{\cdot}2H_2O$ (L: NH_3, npa=n-propylamine) complexes by IR and ESR spectroscopies.

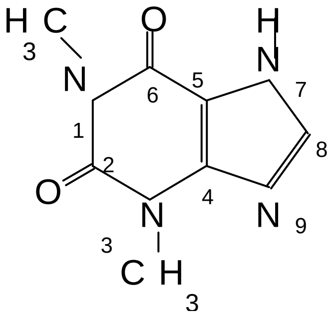

Fig. 1. The molecular structure of theophylline

EXPERIMENTAL

The $CuT_2L_2{\cdot}2H_2O$ compounds were prepared according to the procedure described in paper [3,4]. Infared spectra were recorded in the 4000-400 cm^{-1} range with a Bio-Rad-Digilab_FTS 65A/896 spectrometer by the KBr pellet technique. Far-IR spectra in the range 500-100 cm^{-1} were recorded on a bio-Rad FTS-40V using polythylene pellets. ESR measurements were performed at 9. 4 GHz (X band) using a standard JEOL-JES-3B equipment.

RESULTS AND DISCUSSIONS

The manner in which the Cu(II) ion coordinates the theophylline and the amine molecules results by comparing the IR spectra of the metallic compounds with that of the theophylline [5]. The most important IR bands are presented in Table 1.

In all spectra of complexes the symmetric and antysymmetric ν(NH) vibrations of free amine ligands are shifted to lower wave numbers after the coordination.

The two distinct ν(C=O) stretching vibrations theophylline are lowered by 22-32 cm^{-1} and 7-27 cm^{-1} respectively in theirs metal complexes. These changes are due to the involving of the exocyclic O(6) atom of the theophylline in the hydrogen bonds with the water molecules of the complexes [6,7].

The wide bands of the vibration for the amine's (NH_3) group appear in 3300-3000 cm^{-1} region. In the case of $CuT_2(NH_3)_2{\cdot}2H_2O$ compound, the double degenerate δ_{as}(HNH) frequency is also resolved in 1640-1620 cm^{-1}

domain. The bands which appear in the theophylline IR spectrum, in the region 3000-2600 cm^{-1}, can be attributed to ν(C-H) (2710, 2790 cm^{-1}) and ν(CH_3) (2820 cm^{-1}) vibrations. These bands are widely in the spectrum of the metal complexes in the region 3000-2100 cm^{-1}.

The shifts of the ν(C=N) stretching frequency in the studied compounds given the pure theophylline are due to the coordination of the Cu(II) ion at N(7) atom, which influences indirectly the vibrations of the imidazolic ring's groups.

The IR spectra of both complexes show absorptions in the 3350-3500 cm^{-1} region due to the presence of hydrogen bonded water molecules.

The distinct mode in which the amine molecules influence the local structure of the Cu(II)-theophylline complexes appears clearly in the ESR measurements. Both complexes were investigated in powdered samples and in DMF solutions in the 143-293 K temperature range and also in DMF solutions adsorbed on NaY zeolite.

Powder ESR spectrum of the $CuT_2(NH_3)_2\cdot 2H_2O$ (Fig. 2) is axial (g_{II}=2. 255, $g_{\perp}$=2. 059) and suggests a compressed pseudotetrahedral symmetry around the metallic ion.

Table 1. IR spectroscopic data (cm^{-1}) of the ligand (T) and Cu(II)-theophylline complexes

Compound	**ν(N-H)**	**ν(C=O)**	**ν_s(C=N)**	**δ(N-H)**
T	3111 (as)* 3072 (s)	1717 (s)1667 (as)	1450	1100
$CuT_2(NH_3)_2$	3350 (as) 3270 (s)	1690 (s) 1660 (as)	1410	1100
$CuT_2(npa)_2$	3315 (as) 3260 (s)	1685 (s) 1640 (as)	1412	1110

- *s=symmetrical vibration; as=antisymmetrical vibration*

The 4. 5 value of the G parameter (G=(g_{II}-2. 0023)/($g_{\perp}$-2. 0023)), inside of the usually interval (4÷5), indicates that the experimental data suit to molecular g values. The shape of the spectrum and the **g** tensor values remain unchanged by lowering the temperature to 143K.

Powder ESR spectrum of $CuT_2(npa)_2\cdot 2H_2O$ complex (Fig. 3) shows a superposition between an axial (g_{II}=2. 299, $g_{\perp}$=2. 064) and isotropic

(g_0=2. 100) components [8]. The **g** values remain unchanged when the temperature decreases to T=143 K, while the amplitude of the isotropic spectrum decreases too.

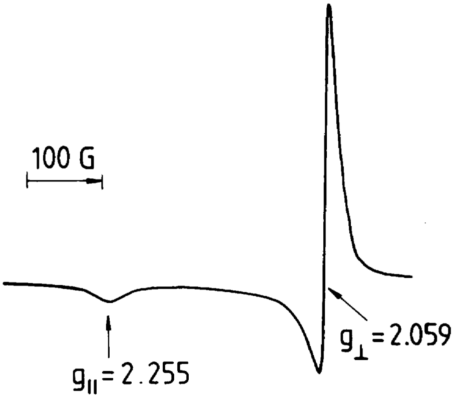

Fig. 2. Powder ESR spectrum of $CuT_2(NH_3)_2{\cdot}2H_2O$ complex at room temperature

The axial spectra of the powder complexes containing (NH_3) and (npa) are due to the compression of the CuN_4 tetrahedron lengthwise of one S_4 axis owing to a static Jahn-Teller effect

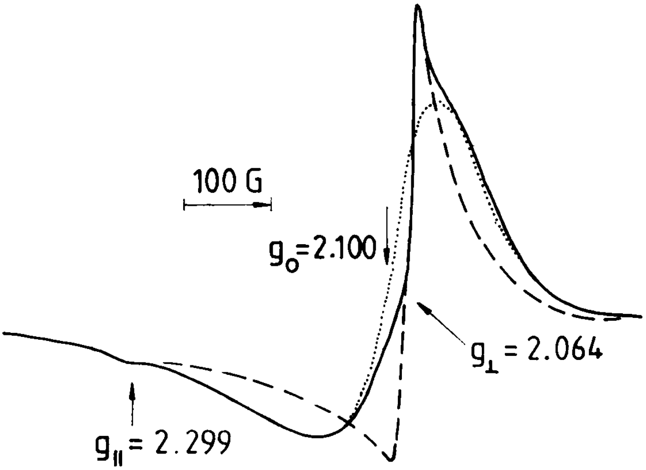

Fig. 3. Powder ESR spectrum of $CuT_2(npa)_2{\cdot}2H_2O$ complex at room temperature

(resulting a flattened tetrahedral local configuration). This effect appears by the vibronical coupling between the electronic states of T_2 symmetry and the active E vibration mode in the cubic group [9]. The isotropic spectrum which appears for $CuT_2(npa)_2 \cdot 2H_2O$ complex corresponds to one trigonal specie compressed lengthwise a C_3 axis owing to a dynamic Jahn-Teller effect ($T_2 \otimes T_2$ vibronical coupling). The amplitude of thus spectrum decreases with the lowering of the temperature because of the diminution of the tunnel effect between the three paraboloid of the potential surface (the probability of this effect $P \approx \exp(-3E_{JT}/k_B T)$, where E_{JT} is the Jahn-Teller energy) [9,10].

The monomeric compressed pseudotetrahedral species are present in DMF solutions too (Fig. 4). The isotropic values g_0=2. 106, A_0=62 G for $CuT_2(npa)_2 \cdot 2H_2O$ and g_0=2. 125, A_0=64 G for $CuT_2(NH_3) \cdot 2H_2O$ and the shape of the spectra are similar to those obtained for other reported Cu(II)-proteins and Cu(II)-enzymes with the metallic ion surrounded by four nitrogen atoms [11].

Both complexes present axial symmetries around the metallic ion in DMF solutions adsorbed on NaY zeolite (Fig. 5). The g_{II} values correspond to a dominant square-planar local symmetry (or strong compressed pseudotetrahedral symmetries) and the $|A_{II}|$ values are typical to a $CuN_2N^*_2$ chromophore (Table 1).

The average of the g values is the same in powder, DMF solutions and DMF solutions adsorbed on NaY zeolite for the compressed pseudotetrahedral species, this fact suggesting the stability of the complexes in solutions. In $g_\perp$ region of $CuT_2(npa)_2 \cdot 2H_2O$ spectrum there are resolved

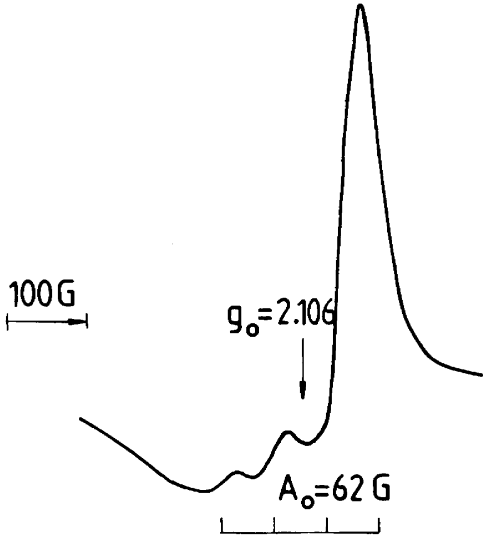

Fig. 4. ESR spectrum of $CuT_2(npa)_2 \cdot 2H_2O$ in DMF solution at room temperature

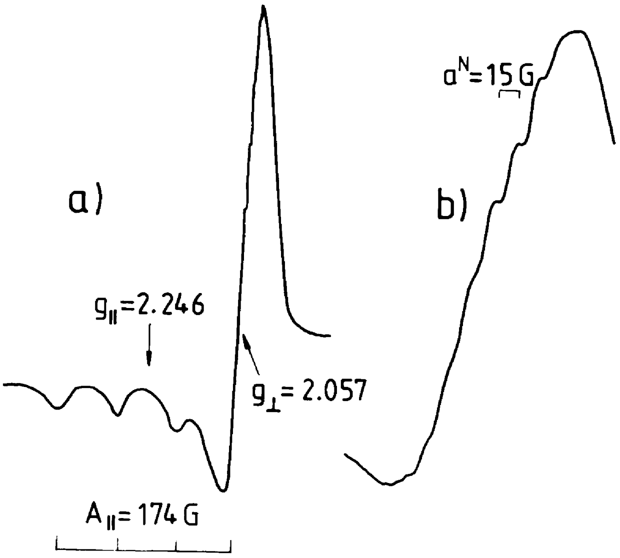

Fig. 5. ESR spectrum of DMF $CuT_2(npa)_2$ solution adsorbed on NaY zeolite at room temperature(a). Extended perpendicular absorption (b)

nine superhyperfine lines owing to the interaction of the paramagnetic electron with four magnetic equivalent nitrogen atoms (a^N=15 G). For $CuT_2(NH_3)_2\cdot 2H_2O$ complex, the superhyperfine structure is not resolved and the signals of the parallel band are broader then those given the previous case. This is a result of the small dimension of the (NH_3) molecules which allows the existence of dipolar interactions between the metallic ions.

Table 1. ESR parameters of DMF Cu(II)-theophylline solutions adsorbed on NaY zeolite at room temperature

Compound	g_{II}	$g_{\perp}$	$\lvert A_{II}\rvert$(G)	***R(cm)***	α(°)	α^2	β^2	δ^2
$CuT_2(NH_3)_2$	2. 254	2. 060	178	121	30	0. 83	0. 61	0. 60
$CuT_2(npa)_2$	2. 246	2. 057	174	124	36	0. 81	0. 61	0. 60

The degree of the pseudotetrahedral compression lengthwise of the S_4 axis of the CuN_4 configuration can be evaluated using the interpolation of R(ω) ratio [12], where R(cm)=$g_{II}/|A_{II}|$ and ω is the dihedral angle between each of the two coordination planes defined by a CuN_2 moiety [13]. The value of the angle ω varies from 0° at 90° with changes in stereochemistry from square-planar to tetrahedral geometry. Also, for square-planar structure R ratio has the typical values 105-135 cm^{-1} and greater ones for dominant pseudotetrahedral symmetry. The obtained R values (Table 1) show a dominant square-planar local structure around the Cu(II) ion. The distortion angle ω shows only a small deviation (≈15°) of the Cu-N bonds out of the xOy plane. This strongly compression of the tetrahedron can be understood in terms of first order vibronic coupling effects of the Jahn-Teller type [9]. The lowering of the ground state by the tetragonal distortion (along an S_4 axis) can be estimated using the following expression [10]:

$$2E_{JT}=\frac{1}{3}e_{\sigma}(5-18\cos^2\theta+9\cos^4\theta)-\frac{9}{4}e_{\pi}(2-9\cos^2\theta+9\cos^4\theta) \qquad (1)$$

where the energy values e_σ and e_π in the Angular Overlap Model (hole formalism) are determined from the diffuse reflectance spectra and the angle θ between one Cu-N bond and the Oz axis from the interpolations of the electronically transitions $\Delta_{II}=\Delta(d_{xy}-d_{x^2-y^2})$ and $\Delta_{\perp}=\Delta(d_{xy}-d_{xz,yz})$ as a function of this angle [12]. Using the approximated values Δ_{II}=13400 cm^{-1} and $\Delta_{\perp}$=15400 cm^{-1} for the compounds containing (NH_3) and (npa) [12], $\theta \approx 73°$ and the relation between e_σ, e_π and Δ_{II}, $\Delta_{\perp}$ [14] a value of ≈2880 cm^{-1} results for the Jahn-Teller energy E_{JT}, in good agreement with the other reported values [17]. Owing to the small value of the spin-orbit coupling energy (≈800 cm^{-1}) comparative with the former, the lowering of the ground state is induced especially by static Jahn-Teller effect.

In the case of species presenting a static Jahn-Teller effect, the molecular coefficients (α, β, δ) have been evaluated with the help of LCAO-MO procedure typical for square-planar configuration [22]. The obtained values (Table 1) show a dominant ionic character of the σ bond in the (xOy) plane and a covalent character of the π bonds in or out of the plane.

CONCLUSIONS

For the Cu(II)-theophylline complexes with some amine ligands the local symmetry around the Cu(II) ion is strongly influenced by the amines nature.

The studied complexes are monomeric, but owing to the packing structure the superexchange and dipolar interactions between the Cu(II) ions appears too. The $CuT_2(npa)_2 \cdot 2H_2O$ and $CuT_2(NH_3)_2 \cdot 2H_2O$ complexes has a compressed pseudotetrahedral local symmetry.

Two different structural species appear in the $CuT_2(npa)_2 \cdot 2H_2O$ due to the vibronical coupling by the static or dynamic Jahn-Teller effect. These species, one stable and another unstable with the temperature (and not only), could have different biological effects.

In the case of $CuT_2(NH_3)_2 \cdot 2H_2O$ complex the great difference between the dimension of the amine and theophylline molecules lead to the stabilization of one state respect to the other, the resulting chromophore being $CuN_2N^*_2$. The difference between ligand nitrogen atoms is even more reduced in $CuT_2(npa)_2 \cdot 2H_2O$ complex and the local environment is CuN_4.

Concluding, one may state that the geometry of Cu^{2+} polyhedra is determined by steric and electronic effects. While the former may stabilize the square-pyramidal geometry the latter induces the expected bond length anomalies.

REFERENCES

1. J. R. J. Sorenson "Metal Ions in Biological Systems", Ed. H. Sigel, vol. 14, Marcel Dekker, New York, 1982.
2. M. Fuente, O. Cozar, L. David, R. Navarro, A. Hernanz, I. Bratu, Molec. and Biomolec. Spectr. , Spectrochimica Acta A, 53,637(1997).
3. P. Bombicz, J. Madarasz, E. Forizs, I. Foch, *Polyedron*, 16, 20, 3601(1997).
4. W. J. Birdsall, Inorg. Chim. Acta, 99, 59)1985).
5. K. Nakamoto, "Infrared and Raman Spectra of Inorganic Coordination Compounds", 3th Ed. Wiley, New York, 1978.
6. T. J. Kistenmacher, D. J. Szalda, L. G. Marzilli, Inorg. Chem. , 7, 14(1975).
7. A. R. Norris, R. Kumar, E. Buncel, Journal of Inorg. Biochem. , 21, 277(1984).
8. O. Cozar, V. Znamirovschi, *Czech. J. Phys*. B 33, 1357(1983).
9. A. Abragam, B. Bleaney, *Electron Paramagnetic Resonance of Transition Ions*, Clarendon Press, Oxford, 1970.
10. D. Reinen, *Comments Inorg. Chem*. , 2, 227(1983).
11. S. A. Chizhanov, V. I. Volkov, A. V. Vorobiev, V. V. Valuev, Russian *Journal of Physical Chemistry*, 7, 67(1993).
12. J. Gouteron, S. Jeannin, Y. Jeannin, J. Livage, C. Sanchez, *Inorg. Chem*. , 23, 3387(1984).
13. H. Yokoi, A. W. Addison, *Inorg. Chem*. , 6, 16(1977).
14. A. B. P. Lever, *Inorganic Electronic Spectroscopy*, 2nd Ed. Elsevier, New York, 1984.
15. D. Kivelson, R. Neiman, *J. Chem. Phys*. , 35, 149(1961).

STUDIA UNIVERSITATIS BABEŞ-BOLYAI, PHYSICA, XLII, 2, 1997

AN IMPROVED PERFORMANCES HOMOGENEOUS MAGNETIC FIELD MASS SPECTROMETER FOR POLLUTANT ANALYZE

P. ARDELEAN[1], C. CUNA[1]

ABSTRACT. A 90^o deflection sector field differentially pumped mass spectrometer with homogeneous magnetic field is described. The analyzing sector has straight boundaries and the mean radius of curvature is 250 mm. Some details of the main parts of the apparatus are given. The resolving power is high enough to allow the testing measurements on the m/e = 28 doublet ($^{14}N_2^+$ and $^{12}C^{16}O^+$) and on the m/e = 29 triplet ($^{13}C^{16}O^+$, $^{14}N^{15}N^+$ and $^{12}C_2H_5^+$). A peak half height resolving power of 5900 was obtained at an ion current intensity of $1.1*10^{-12}$ A, for a final ion acceleration slit of 0.01 mm. For a slit width of 0.02 mm the resolving power was 4800 at an ion current intensity of $2.3*10^{-12}$ A. The intensity of the ion current was $3.5*10^{-12}$ A at a peak half height resolving power of 4200 for a final acceleration slit of 0.03 mm.

INTRODUCTION

The fossil fuels are, as it knows, one of the more important energy sources in nowadays [1]. But the combustion of the fossil fuels produces, among others, nitrogen oxides and carbon oxides which pollute the atmosphere. Taking into account the importance of NO, CO and CO_2 in the chemistry of the atmosphere [2, 3], and in the Earth's radiation budget [2, 4, 5], as well as for the influence on the public health [6], the measurement of theirs concentration levels is very important.

The analytical purposes for environmental samples implies many times quite high precision at a low concentration levels. Mass

---

[1] Institute for Isotopic and Molecular Technology, P.O. Box 700, 3400 Cluj-Napoca 5, Romania

spectrometry could have, for this reason, an important place taking into account its selectivity and sensitivity.

Here is described an improved performances mass spectrometer designed for pollutant concentration and isotopic concentration measurements. It can be used in the mass range from 1 to 300 mass units for gases and volatile liquids. The ion main path curvature radius is 250 mm.

DESCRIPTION

The mass spectrometer is a homogeneous magnetic field one, with 90^o deflecting sector field.

The sampling system is a standard one, allowing the simultaneous attachment of two samples. For to introduce the sample from container into the ion source a capillary tube is used.

The mass spectrometer ion source was derived from the modified Nier design [7]. It consists (fig.1), from an ionization chamber (IC) with the electron gun (EG), electron collector (EC) and ion repeller (IR), the half plates (HP), the cylindrical lens (CL), the z deflector (ZD) and the final ion beam acceleration slit (AS). It was observed that the relative position of the cylindrical lens in the ion gun and its polarization is critical, in order to obtain a well focused beam. The energy of the ionizing electrons could be varied in the range 40-100 eV [8]. The intensity of the ionizing current measured on the collector is established under 10 μA for to avoid space charge effects. The ion source is also provided with an auxiliary collimating magnetic field for electron beam focusing.

The analyzer is a 90^o linear boundary homogeneous magnetic sector field, with normal incidence. The magnetic analyzer sector position can be regulated by screw. For to positionate the analyzing field sector the fringing fields were taken into account [9].

The ion detection system use a variable grounded slit and a Faraday cage or, alternatively, an ion multiplier, for to increase the sensibility. The use of an alternative detection system ensure a large dynamic range of the detection, theoretically over 10^7.

The vacuum system is a double one permitting the differentially pumping of the mass spectrometer, the ion source housing being connected to the analyzer tube by a small conductance slot.

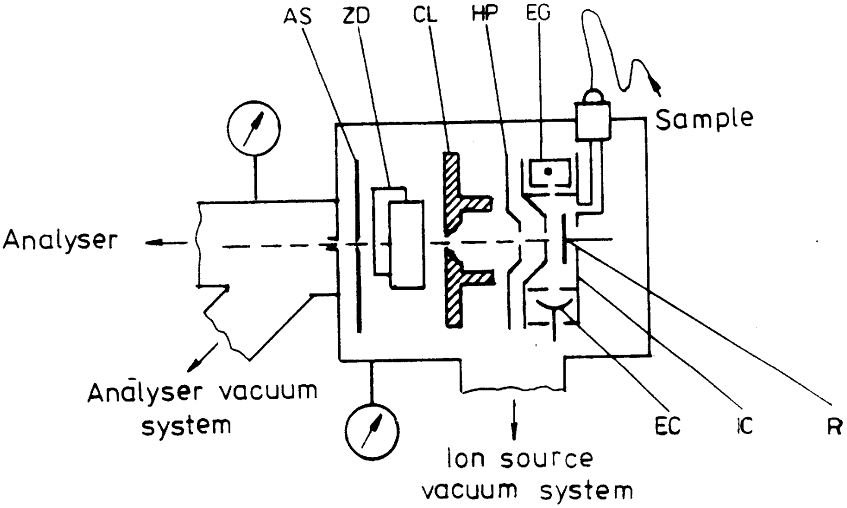

Fig. 1

The diagram of the ion source.

EXPERIMENTAL RESULTS AND DISCUSSIONS

The measurements were performed on the m/e = 28 doublet ($^{14}N_2^+$ and $^{12}C^{16}O^+$) and respectively on the m/e =29 triplet ($^{13}C^{16}O^+$, $^{14}N^{15}N^+$ and $^{12}C_2{}^1H_5{}^+$) obtained for a mixture of air and CO_2. This was because the resolving power is high enough for to be better reflected by the small shift m between the peaks.

The half height resolving power obtained for a 0.03 mm wide final acceleration slit was 4200, at an ion current intensity of $3.5*10^{-12}$ A. The intensity of the ionizing current was 8 µA, and the accelerating voltage was 5 kV.

The selectivity and sensibility of the mass spectrometer are very important in the pollutant concentration analyze.

In orde to obtain improved performances, the supplementary aberrations arising from machining, mounting and alignment errors were taken into account. These supplementary aberrations are proportional with the angular aperture α_0 and with the energy dispersion of the beam issuing from the ion source [10].

In this respect the use of a small width final acceleration slit was used for to reduce the angular aperture.

For the case of an final ion beam acceleration slit width of 0.02 mm, a resolving power at peak half height of 4800 (fig. 2) at an ion current intensity of 2.3*10^{-12} A was obtained.

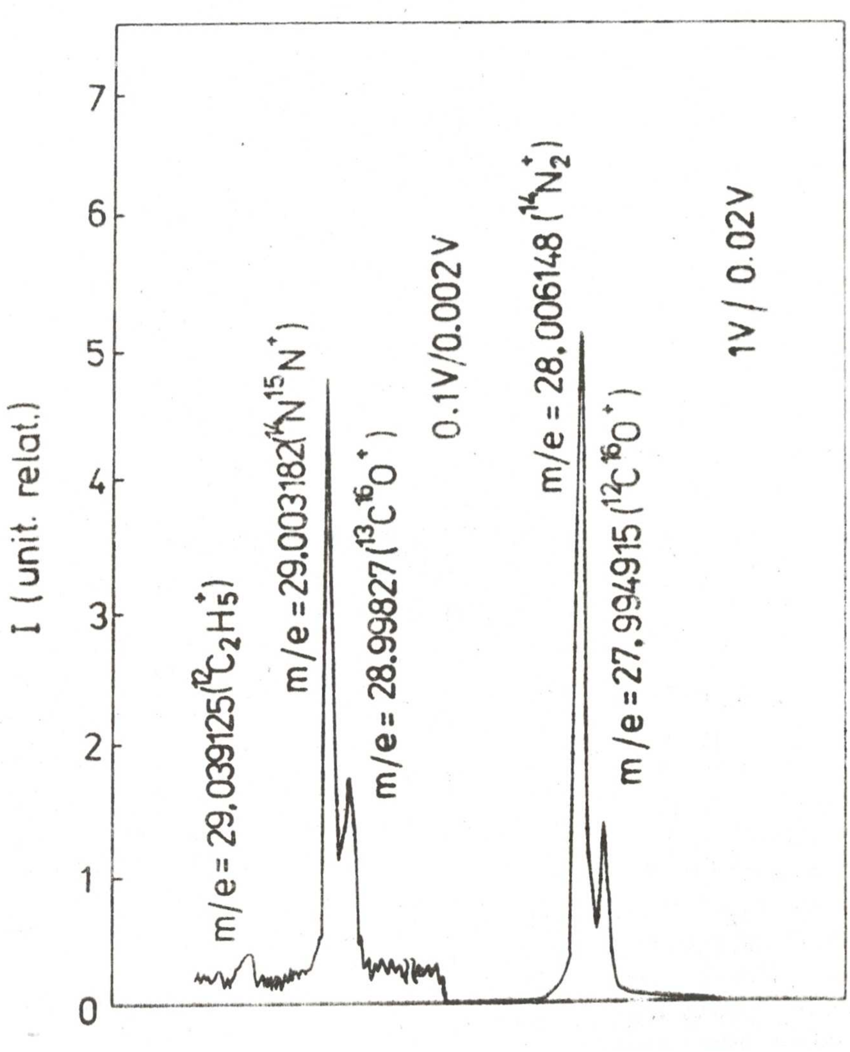

Fig. 2. The mass spectrum of the m/e = 28 doublet and of the m/e = 29 triplet for a final slit width of 0.02 mm.

For to allow a correct location of the analyzing sector field relative to the ion source and to the collector, measurements of the resolving power and of the ion current intensity were made versus the analyzing field sector position (fig. 3). As it can be observed the measurements showed that the resolving power depend critically by a correct iono-optical alignment. So, the resolving power could decrease for an incorrect alignment for over 2 times, and the obtaining of the resolving power maximal value is possible only for a quite slight area around the exact alignment position (fig. 4). In this way a resolving power of over 5900 was reached for an accelerating slit width of 0.01 mm at an ion current intensity of $1.1*10^{-12}$ A.

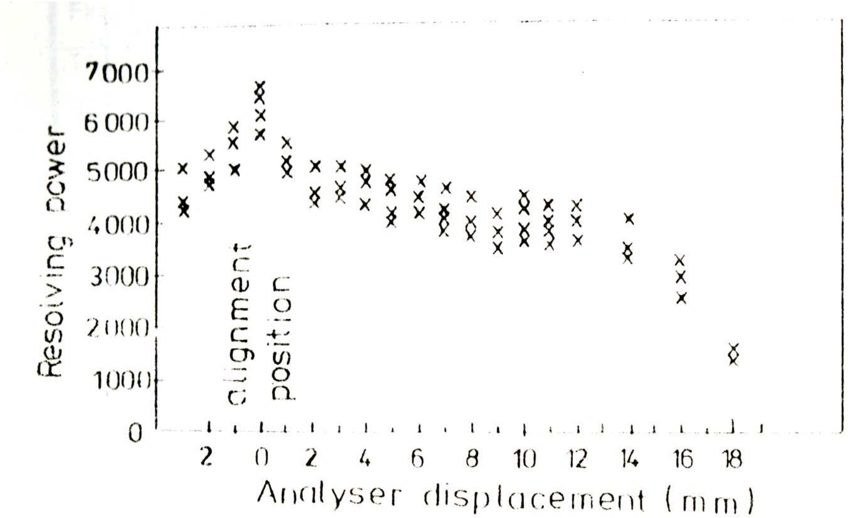

Fig. 3.The variation of the resolving power versus the analyser sector position.

The theoretical peak half height resolving power R_t can be obtained from :

$$R_t = [\, s/C + U_s/U + U_f/U + 2\, I_m/I_m \,]^{-1} \qquad (1)$$

where s is the final source acceleration slit width, C the main path radius, e U_s the difference between the energies of the ions formed at the same point of the ion source at different instants due to the high voltage short time instabilities or noise, in our case $3*10^{-5}$ of the value of the ion accelerating energy eU, e U_f the beam energy spread due to the thickness of the ionization region, typically 0.3 eV, I_m is the instability or noise of the magnet current supply, in our case $1.5*10^{-5}$, and e is the ion electric positive charge.

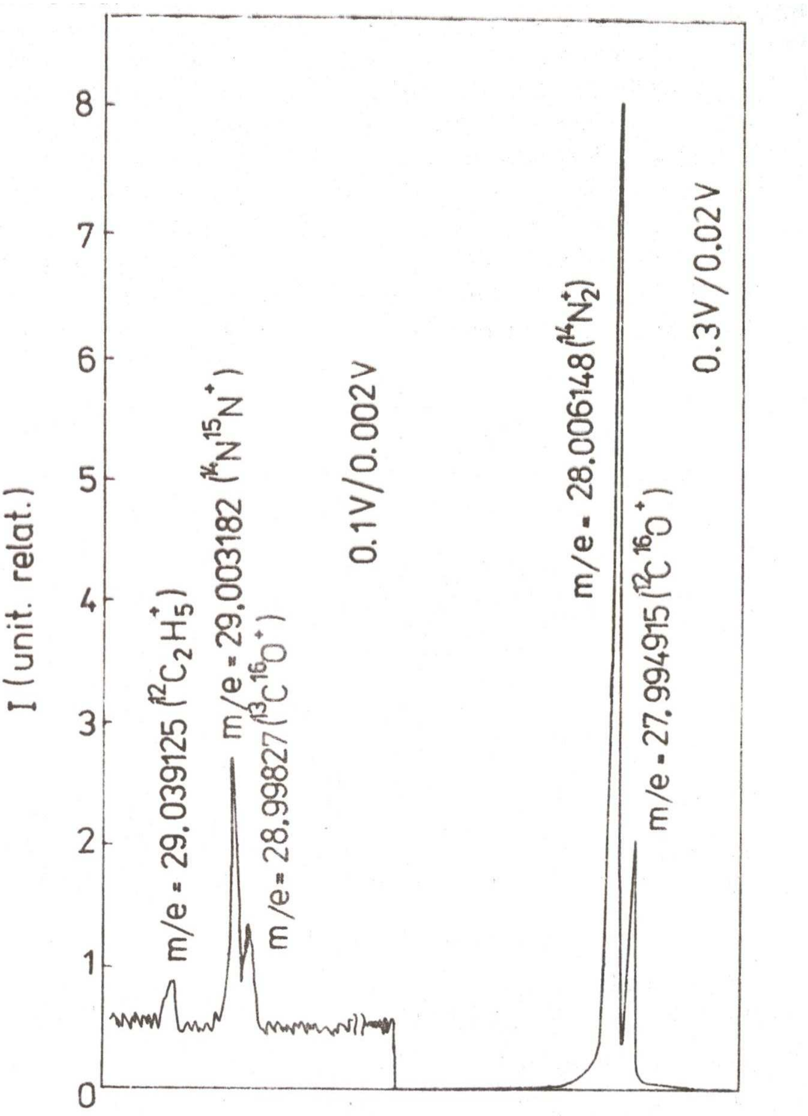

Fig. 4. The mass spectrum for a final ion source slit width of 0, 01 mm

In the table I the values obtained for the resolving power experimentally obtained from the spectra as well as the values obtained from (1) for different ion source final acceleration slit widths are given. As it can be observed the resolving power values obtained experimentally are close to the values obtained from (1), proving that the focussing properties of the ion gun allow to deliver a well focused ion beam and also that it is a correct iono-optical alignment of the apparatus.

Table I

Final ion beam acceleration slit	0.03 mm	0.02 mm	0.01 mm
Theoretical resolving power (1)	4166	5000	6250
The resolving power from spectra	4200	4800	5900

REFERENCES

1. J. M. Pacyna, S. Larsen, A. Semb, Atmos. Environ., 25A, 425 (1991).
2. E. G. Brunke, H. E. Scheel, W. Seiler, Atmos. Environ., 24A, 585 (1990).
3. G. Helas, A. Broll, K. J. Rumpel, P. Warneck, Atmos. Environ., 21, 2285 (1987).
4. D. S. Kim, V. P. Aneja, W. P. Robarge, Atmos. Environ., 28, 1129 (1994).
5. J. Weinheimer, J. G. Walega, B. A. Ridley, B. L. Gary, D. R. Blake, N. J. Blake, F. S. Rowland, G. W. Sachse, B. E. Anderson, J. E. Collins., Geophys. Res. Lett., 21, 2583 (1994).
6. M. Luria, R. Weisinger, M. Peleg, Atmos. Environ., 24B, 93 (1990).
7. J. Barnard, *Modern Mass Spectrometry*, The Institute of Physics, London, !953, p. 60.
8. V. Mercea, P. Ardelean, D. Ioanoviciu, A. Pamula, D. Ursu, *Introducere în Spectrometria de Mas*, Edit. Tehnic, Bucure ti, 1978, p. 43.
9. H. Matsuda, H. Wollnik, Nucl. Instrum. Methods, 77, 50 (1969).
10. D. Ioanoviciu, C. Cuna, A. Mihail, Rev. Rom. Phys., 19, 963 (1974).

STUDIA UNIVERSITATIS BABEŞ-BOLYAI, PHYSICA, XLII, 2, 1997

BETA RADIOACTIVITY OF UO_3 IMMOBILIZED IN SOME BORATE GLASS MATRICES

E. CULEA[1], TANIA RISTOIU[2], C. COSMA[2]

ABSTRACT. Beta activity of (0. 95-x) $Na_2B_4O_7$-xUO_3-0. 05 M_2O_3 glasses with M=B, Al, Nd and Ho and x=0. 01, 0. 05, 0. 10 and 0. 15 was investigated. The composition dependence of the beta activity presents (excepting glasses with M=Ho) a decrease of the slope for increasing mass of M ions. The leaching in water evidenced no remarcable aqueous dissolution of the studied glasses.

INTRODUCTION

The study of glasses containing radionuclides is important since glass is used to immobilize nuclear waste [1]. Borosilicate glasses play an important role among the vitreous matrices proposed for nuclear waste disposal [2, 3]. In order to be appropriate for immobilization of nuclear waste the vitreous matrices must accomplish important requirements such as: a) to incorporate important amounts of nuclear wastes, b) to own high chemical stability and mechanical resistance, c) to present low aqueous dissolution and d) to own high level absorption of nuclear radiation.

Uranium is one of the radionuclides contained within the nuclear waste that requires secure immobilization from the environment through its storage in appropriate glass matrices. Previous studies investigated the influence of the glass composition and of the parameters of glass processing on the spectroscopic behavior of uranium ions incorporated in some borosilicate [2, 3], borate [4, 5] and phosphate glasses [6]. Studies concerning the radioactive behavior of UO_3 incorporated in borate glasses were reported, too [7, 8].

The aim of this study was to investigate the beta radioactive behavior of uranium ions immobilized in some borate glasses belonging

---

[1] Technical University of Cluj-Napoca Physics Dept., str.C.Daicoviciu nr.15, 3400 Cluj-Napoca, Romania, phone: +40 64 415051, fax: +40 64 195355, +40 64 415053, e-mail: eugen.culea@phys.utcluj.ro

[2] Babeş-Bolyai University of Cluj-Napoca

to the (0. 95-x) $Na_2B_4O_7$-xUO_3-0. $05M_2O_3$ system, where M=B, Al, Nd and Ho and x=0. 01, 0. 05, 0. 10 and 0. 15. In order to examine the possibility of using these glass matrices for nuclear waste immobilization their resistance to water leaching was also studied.

EXPERIMENTAL

Samples of the (0. 95-x) $Na_2B_4O_7$-xUO_3-0. 05 M_2O_3 systems with M=B, Al, Nd and Ho and x=0. 01, 0. 05, 0. 10 and 0. 15 were prepared. They were obtained using reagent grade $Na_2B_4O_7\cdot$ $10H_2O$, HBO_3, Al_2O_3 (Reactivul, Romania), Nd_2O_3, Ho_2O_3 (Fluka, Germany) and uranyl nitrate $UO_2(NO_3)_2$. $6H_2O$ (Chemapol, Czechoslovakia). First the $Na_2B_4O_7$ and B_2O_3 glasses were prepared by melting dehydrated borax at 1000°C for 30 minutes. Appropriate mixtures of powdered $Na_2B_4O_7$ and B_2O_3 glasses, UO_3 and M_2O_3 were milled in an agate ball mill for 1 hour and then were melted at 1200°C for 15 min. All the mixtures were molten in alumina crucibles. The glass charges were obtained as slabs (about 20x8x3 mm) by pouring the melts in stainless steel having an appropriate groove.

Chemical analysis indicated that the obtained glasses had the same compositions as the raw material mixtures introduced in the crucibles. X-ray powder diffraction ascertained the vitreous state of all the samples.

The β radioactivity of the glass slabs and of the UO_3 powder was measured. Counting rate measurements were made using a 70020 VAZ-520 proportional detector and a 20026 RFT counter. The glass slabs were measured exposing their 20x8 mm surface to the detector. To avoid the β retrodiffusion the samples were placed on a plastic sample carrier. The UO_3 powder was placed for measurement in a circular plastic box with a diammeter of 20 mm, being uniformly spreaded on the available surface. The sample-detector distance was 5 mm in all cases.

To study the influence of aqueous dissolution the samples were immersed in water and maintained at 50°C for 7 days. Mass measurements were performed to observe mass losses due to the leaching.

RESULTS AND DISCUSSION

All the obtained samples were yellow suggesting the presence of uranium ions mainly as U^{6+} [2,4,6].

The specific activity, Λ_S, of the samples was computed using [9]

$$\Lambda_s = \frac{4\pi n}{60\Omega m}, \tag{1}$$

where n is the counting rate of β particles (pulses/min), Ω is the solid angle (sr), and m is the mass of the samples (g). A standard computer program was used to compute the value of the solid angle according to the shape of the samples. This procedure leads to a value of Ω=3. 89 for the studied glass samples and of Ω=4. 06 for the UO_3 powder. In order to compare the β activities of the samples having different compositions the activity per mole, Λ_{mol}, was calculated for each sample. The estimated relative errors for the molar activity $\Delta\Lambda_{mol}/\Lambda_{mol}$ were less than 5% for all the samples.

Fig. 1 presents the composition dependence of the molar activities for the (0. 95-x) $Na_2B_4O_7$-xUO_3-0. 05M_2O_3 glasses. The dependence of the molar activities on the uranium oxide content of the samples, x, was linear for all the studied glass systems.

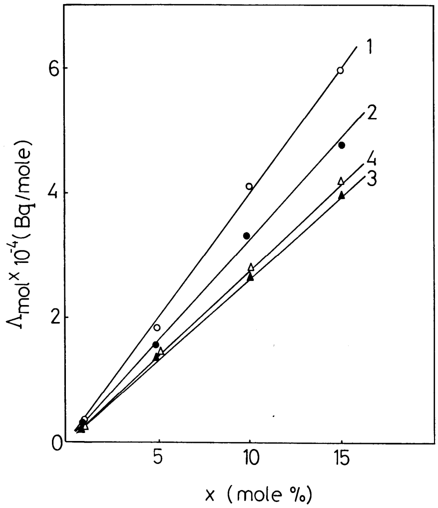

Fig. 1. Composition dependence of (0. 95-x) $Na_2B_4O_7$-xUO_3-0. 05 M_2O_3 glasses with M=B (1), Al (2), Nd (3) and Ho (4).

Specific and molar activity values of the 0. $90Na_2B_4O_7$-0. $05UO_3$-0. 05 M_2O_3 glasses with M=B, Al, Nd and Ho and of powder UO_3 are presented in Table 1. The mass of 0. 170 g choosen for UO_3 corresponds to the amount of UO_3 incorporated in the studied 0. $90Na_2B_4O_7$-0. $05UO_3$-0. 05 M_2O_3 glass samples. Thus, the activity data presented in tabel 1 offer the possibility of a relevant comparision between free and immobilized UO_3.

TABLE 1

Sample	Mass (g)	Counting rate (pulses/ min)	Λ_s (Bq/g)	Λ_{mol} (Bq/mol)	$\Delta\Lambda$ (Bq/mol)
0. $90Na_2B_4O_7$-0. $05UO_3$-0. $05B_2O_3$	2. 401	4194	94	18693	561
0. $90Na_2B_4O_7$-0. $05UO_3$-0. $05Al_2O_3$	2. 437	3306	73	14635	585
0. $90Na_2B_4O_7$-0. $05UO_3$-0. $05Nd_2O_3$	2. 461	2790	61	12944	518
0. $90Na_2B_4O_7$-0. $05UO_3$-0. $05Ho_2O_3$	2. 498	2924	63	13499	540
UO_3	0. 170	9895	3001	858367	8584

A simple examination of these data evidences a very important decrease of the activities for the glass samples with respect to that of the UO_3 powder. This suggests an efficient radioprotective effect of the glass matrices. The examination of the activity values in Fig. 1 and Table 1 leads to the conclusion that the radioprotective effect of glass matrices depends on their composition. Thus, a decrease of the slopes of the beta activities occurs with increasing mass of M ions, except for glasses containing holmium ions. The presence of heavier atoms in the glass matrix seems to improve its radiation absorbing ability. The irregular behavior observed for glasses with holmium ions (curve 4 in Fig. 1) suggests that there are other factors, too, that influence the absorption of radiation by the glass matrix. One of these factors may be related to the network modifier role played by some of the rare-earth atoms [10] incorporated in borate glass matrices having as result a more or less compact structure of these glasses.

The mass measurements of the samples submitted to the water dissolution test evidenced mass losses lower than 10^{-3}g. This suggests that the studied glasses present an acceptable dissolution resistence aqainst water.

CONCLUSIONS

The investigated glass systems were found to have the ability to incorporate UO_3 up to 15 mol %. Their beta activity decrease with increasing the mass of M ions, except the case of M=Ho. To explain the irregular radioactive behavior of glasses containing Ho and Nd ions, their network modifying role may be taken into account.

REFERENCES

1. J. L. Crandall, Scient. Basis Nucl. Waste Mgmt. 2(1980) 39.
2. H. D. Schreiber, G. B. Balazs, Phys. Chem. Glasses 23 (1982)139.
3. H. D. Schreiber, G. B. Balazs, P. L. Jamison, A. P. Shaffer, Phys. Chem. Glasses 23(1982)147.
4. E. Culea, I. Milea, I. Bratu, J. Molec. Struct. 294 (1993)271.
5. E. Culea, I. Milea, J. Non-Cryst. Solids 208 (1996) 199-203.
6. V. Simon, I. Ardelean, O. Cozar, S. Simon, J. Mat. Sci. Let. 15 (1996) 84-785.
7. E. Culea, A. Negoescu, C. Cosma, J. Nucl. Mat. 217 (1994) 220-221.
8. V. Simon, I. Ardelean, O. Cozar, S. Simon. J. Nucl. Mat. 230 (1996) 306-308.
9. K. Siegbahn, α,β and γ-Ray Spectroscopy, North-Holland, Amsterdam, 1970, p. 115.
10. W. Vogel, Glasschemie, VEB Deutscher Verlag fur Grundstoffindustrie, Leipzig 1979.

STUDIA UNIVERSITATIS BABEŞ-BOLYAI, PHYSICA, XLII, 2, 1997

$(SF_6)_2$ - Ar_m CLUSTER STRUCTURES

A. BENDE, A. HAMZA[1]

ABSTRACT. A site-site intermolecular potential model for $(SF_6)_2$-Ar_m clusters is used to determine the cluster structures for m=2,4,6,8,10,12,14,16,18,22,26,28.

INTRODUCTION

In the last years a great amount of work has been invested to understand the structure and dynamics of molecular clusters. One of the most promising experimental techniques to study van der Waals clusters is infrared photodissociation spectroscopy in molecular beams. Even though until now there have been studied the structures and vibrational spectra of homogeneous $(SF_6)_n$ and SF_6-Ar_m mixed clusters [1,2,5], there is no literature about $(SF_6)_n$-Ar_m clusters. In typical experiments, the ν_3 vibrational mode of SF_6 clusters is excited by CO_2 laser radiation and argon is used as a buffer gas. As a result of the mutual interaction of the molecules within the clusters, the spectral bands are shifted. In order to calculate the frequency shifts the cluster potential must be known and the cluster structures have to be determined by minimizing the total interaction energy of the cluster components. In the case of the mixed $(SF_6)_n$-Ar_m clusters, the vibrational shifts appear not only due to the mutual interaction of the molecules, but because of the surrounding Ar atoms, as well. For the SF_6 - SF_6 interaction we use the potential model proposed by Beu and Takeuchi [1], adding new terms to account for the Ar-S, Ar-F and Ar-Ar interactions, respectively [2,3].

---

[1] University Babeş-Bolyai, Department of Theoretical Physics 3400 Cluj-Napoca, Romania

THE INTERMOLECULAR POTENTIAL

The most important aspect for structure and frequency shift calculations is the proper choice of the intermolecular potential. Hence, the form of the potential has been chosen such as to reproduce the properties of the system and, at the same time, to take into account the computational efficiency. It has been proven that a site-site intermolecular potential, which depends only on relative atom positions, is a good choice for our purpose.

The used intermolecular potential includes exchange, dispersion, electrostatic and induction terms for the SF_6-SF_6 interaction [1]:

$$U^{exch} = \sum_{m=1}^{M-1} \sum_{m'=m+1}^{M} \sum_{i\in m} \sum_{j\in m'} A_{ij} \exp(-B_{ij} r_{ij})$$

$$U^{disp} = -\sum_{m=1}^{M-1} \sum_{m'=m+1}^{M} \sum_{i\in m} \sum_{j\in m'} \frac{C_{ij}}{r^6{}_{ij}}$$

$$U^{elec} = \sum_{m=1}^{M-1} \sum_{m'=m+1}^{M} \sum_{i\in m} \sum_{j\in m'} \frac{q_i q_j}{r_{ij}}$$

$$U^{ind} = -\frac{1}{2} \sum_{m=1}^{M} \sum_{i\in m} \alpha_i \left| \sum_{\substack{m'=1,\\ m'\neq m}}^{M} \sum_{j\in m'} \frac{q_j r_{ij}}{r^2{}_{ij}} \right|^2$$

where r_{ij} is the distance between atom i of monomer m and atom j of monomer m'. The atomic effective charges within the SF_6 monomer were determined considering the recent and accurate value μ_{01} = 0. 437 D of Kim and by imposing the condition of monomer neutrality, from: $\mu_{01} = \frac{1}{\sqrt{2}} \sum_a q_a \tilde{l}_{a\alpha}{}^n$ where a is the atom index, α is the Cartesian coordinate index, and $\tilde{l}_{a\alpha}{}^n$ are the l-matrix elements. The coefficients A_{ij},B_{ij},C_{ij} can be constructed from the coefficients A_{ii},B_{ii},C_{ii} of the individual atomic species by using the standard combination rules: $A_{ij} = \sqrt{A_{ii} A_{jj}}$, $B_{ij} = \left(B_{ii} + B_{jj}\right)/2$, and $C_{ij} = \sqrt{C_{ii} C_{jj}}$. For A_{ii} and B_{ii} there have been considered the values reported by Spackman [6] and for C_{ii} those used by Beu and Takeuchi [1]. Up to now we have considered the SF_6 clusters. The data for this potential are summarized in Table 1. In addition to this potential we have included two more terms: one for the Ar-SF_6 interaction and the other for the interactions between the argon atoms. For the Ar-SF_6 interactions we have used the potential proposed by Eichenauer and Le Roy [2] as the sum of the Ar-S interaction potential and the Ar-F interaction potential:

$$U_{Ar-SF_6}\left(R_l,\{Q_i\}\right)=U_{Ar-S}\left[R_j-r_S\left(\{Q_i\}\right)\right]+\sum_{l=1}^{6}U_{Ar-F}\left[R_j-r_{F_l}\left(\{Q_i\}\right)\right]$$

where R_j denotes the positions of the Ar atoms and $\{Q_i\}$ is the stretching coordinate of SF_6, r_S are the positions of the S atoms and r_{F_l} , (l=1,2,. . . 6) the positions of the six F atoms, from every cluster. In the second term of the expression there are included all the F atoms from one cluster. All the relevant data for the description of the potential models are summarized in Table 2 and Table 3.

Table 1. Parameters for homogeneous SF_6 cluster potential model.

	A_{ii} (kJ/mol)	$B_{ii}(A^{-1})$	$C_{ii}(kJ/molA^6)$	$q_i(e)$	$\alpha_i\,(a_0^3)$
S	540857	3. 132	8519. 6	3. 825	7. 2
F	336133	4. 128	658. 0	-0. 6375	5. 1

Table 2. Parameters of the Ar-SF_6 potential.

	Ar-S	Ar-F
A(eV)	0	15700
p	. . .	-0. 675
$b(A^{-1})$	4	4. 23
$C_6(eVA^6)$	117	5. 52
$C_8(eVA^8)$	1021	0
$C_{10}(eVA^{10})$	8437	0

Table 3. Parameters of the approximate poential for Ar-Ar.

	Ar-Ar
$A_6(eVA^6)$	-59. 7
$A_9(eVA^9)$	-6.95×10^2
$A_{12}(eV^{12})$	10.97×10^4

The Ar-F potential is anisotropic, with axial symmetry around the S-F bonds,

$$U_{Ar-F_l}(r_l,\theta_l)=A\left[1+pP_2(\cos\theta_l)\right]\exp(-br_l)-\sum_{n=3}^{5}\left[1-\exp(-br_l)\sum_{k=0}^{2n}\frac{(br_l)^k}{k!}\right]\frac{C_{2n}}{r_l^{2n}}$$

where $r_l=\left|R_j-r_{F_l}\right|$, θ_l is the angle subtended by $\left(R_j-r_{F_l}\right)$ and $\left(r_{F_l}-r_S\right)$ and $P_2(\cos\theta_l)=\left[3\cos^2\theta_l-1\right]/2$. The coefficients C_{2n}, (n=3,...5) are the dispersion constants of Pack and Valentini [4]. The $U_{Ar\text{-}S}$ potential has the same expression, with different coefficients.

Since the structure calculations based on the Ar-Ar potential proposed by Aziz and Slaman [3] turned out to be too time consuming, we have considered the approximate form of this interaction energy [3]:

$$U_{Ar-Ar}=\frac{A_{12}}{r^{12}}+\frac{A_9}{r^9}+\frac{A_6}{r^6}$$

with the parameters A_{12},A_9,A_6 determined from a least squares fit to the well region of the Ar-Ar potential of Aziz and Slaman [3].

Since the dipole-dipole interaction plays the main role for the vibrational frequency shifts of homogenous SF_6 clusters, we have considered appropriate to take into account a similar term for the mixed clusters, too. Because of its symmetry, an SF_6 molecule in its equilibrium configuration has no dipole moment. However, when displaced from equilibrium in the course of the ν_3 vibrational motion, an instantaneous electric dipole moment arises which gives rise to an electric field at the position R_j of the Ar atoms. This electric field induces a dipole-moment on the Ar atoms. So we can speak about the interaction energy between the induced dipole and the instantaneous dipole, which, knowing the effective atomic charges, has the form:

$$U_{Ar-SF_6}^{ind}=-\frac{\alpha}{2}\sum_{j=1}^{N}\sum_{m=1}^{M}\sum_{i\in m}\left|\frac{q_j r_{ij}}{r_{ij}^2}\right|^2$$

where N is the number of inert gas (Ar) atoms and M is the number of SF_6 molecules. The coefficient $\alpha=1.642\,\mathrm{A}$ is the dipole polarizability of the Ar atoms.

CLUSTER STRUCTURES

Our cluster structure calculations have been performed by minimizing the total interaction energy of the cluster components. Considering the molecules and atoms "frozen" in their equilibrium positions and minimizing the intermolecular potential with respect to their relative position one can find the global minimum.

The geometry of the system is specified by the center of mass Cartesian coordinates and the Euler angles of the molecules and atoms. The initial configuration of the system is randomly chosen, and the optimization is done by the EO4JAF routine, without any constraints. Typically, several hundreds of minimizations are required to yield the global minimum. We have been performing minimizations until in the energy spectra haven't appeared new values. The global minimum is the lowest energy value from the spectra.

We have studied cluster structures containing two SF_6 molecules and 2,4,6, 8,10,12, 14,16,18,22,26,28 Ar atoms. The result of these cluster structure calculations are summarized in Table 4 where the binding energies are shown and compared with the results for the homogeneous SF_6 dimer. At the same time it can be seen that the binding energy is decreasing as the number of the Ar atoms is increasing. It can be seen from the cluster structures depicted in Figure 2a,2b that the S_{2h} symmetry of the homogeneous SF_6 dimer is broken if we adding inert gas atoms. The S-S bond length has changed, too. In the Figure 1 we have depicted the incremental binding energy as a function of the Ar atom numbers (M).

Table 4. Calculated cluster structures. M represents the number of Ar atoms in the cluster structure and E is the total binding energy in kJ/mol.

M	E(kJ/mol)
0	-6. 68
2	-15. 17
4	-24. 93
6	-36. 02
8	-46. 30
10	-57. 35
12	-67. 27
14	-76. 89
16	-91. 44
18	-99. 87
22	-125. 02
26	-150. 34
28	-163. 89

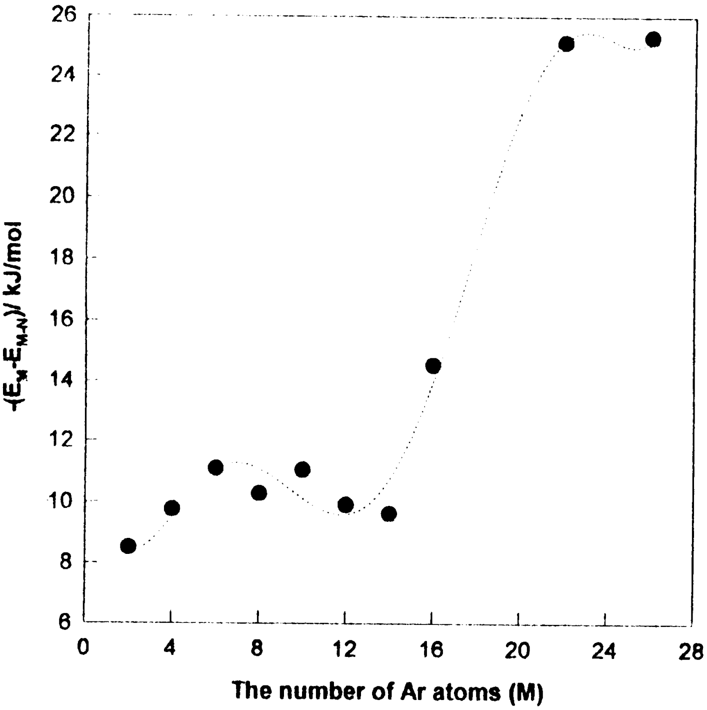

Figure 1: Incremental binding energy of $(SF_6)_2$-Ar_m mixed clusters.

In the case of 6 Ar atoms, all these atoms are situated in an almost perpendicular plane to the S-S bond, forming a hexagon in this plane. If the number of Ar atoms is increasing, the structure remains qualitatively the same, the new Ar atoms tending to form a closed shell around the SF_6 dimer. When the number of Ar atoms in the cluster reaches 18, the hexagon transforms into an octagon. For a considerable number of inert Ar atoms (around 28-30), the compact shell is realized.

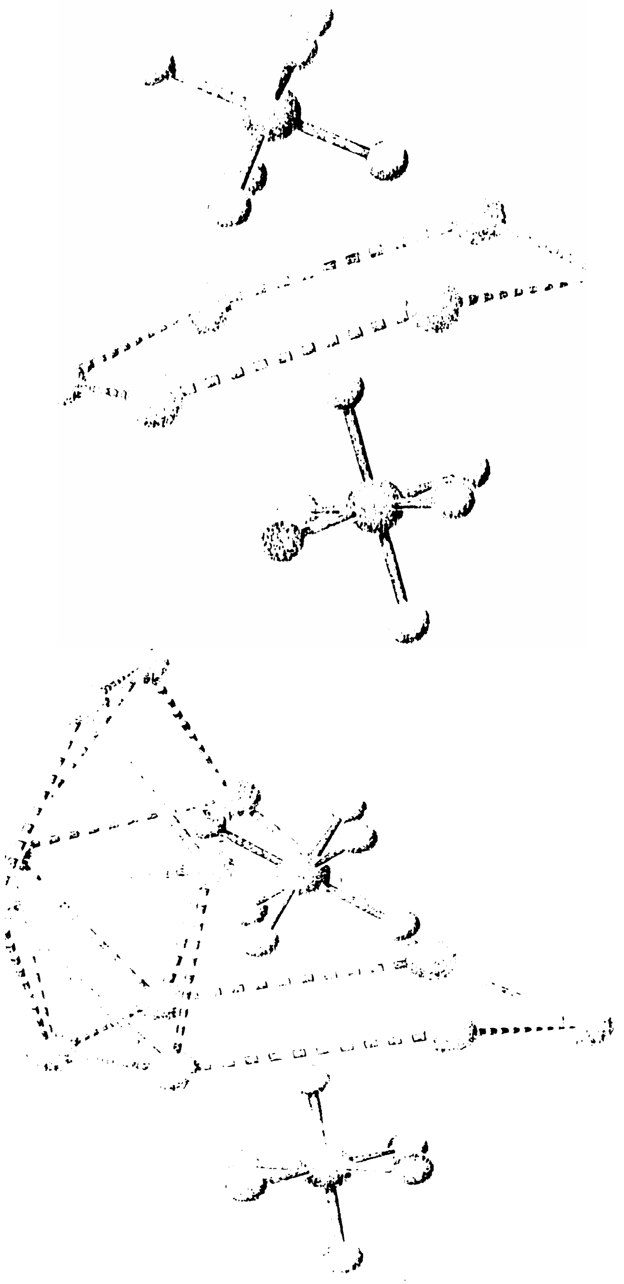

Figure 2a,: $(SF_6)_2$-Ar_m cluster structures for m=6,12.

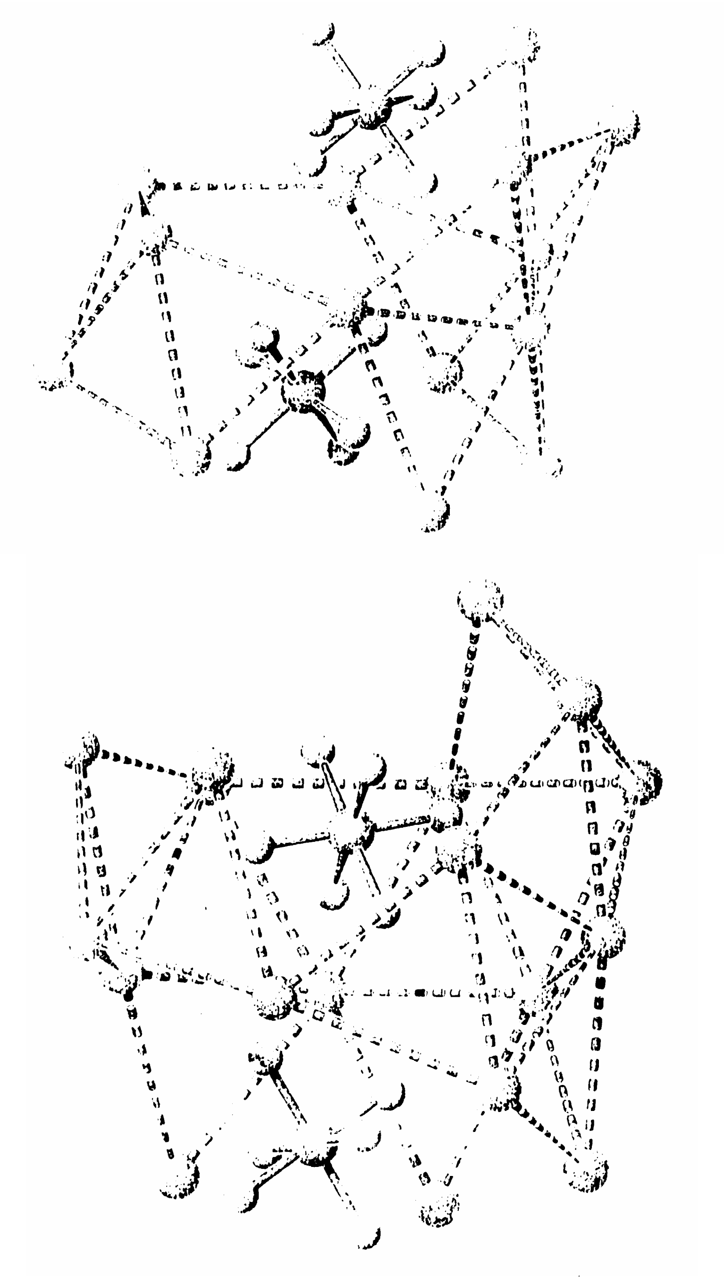

Figure 2b,: ($SF_6)_2$-Ar_m cluster structures for m=14,18.

It can be seen (Figure 1), that between M=4 and M=14 the energy increments are relatively small, and for M=16,. . . ,20 the energy increments have an increasing tendency. This increasing is due to the transition from the hexagon to the octagon in the cluster structures.

CONCLUSIONS

To the intermolecular potential model for homogenous SF_6 clusters there have added supplementary terms which describe the interaction between SF_6 molecules and Ar atoms, and between the Ar atoms. We have considered also the dipole induced dipole mechanism for SF_6-Ar clusters. This potential model is applied to compute mixed $(SF_6)_2$ -Ar_m cluster structures, which breaks the symmetry of the homogeneous SF_6 dimer. We have started our simulations with a low numbewr of Ar atoms, increasing them. When their number has reached M=28-30 they have covered the SF_6 dimer, forming a closed shell.

The $(SF_6)_2$-Ar_m are mainly bounded by the dispersion attraction, the effect of the induction interaction can be neglected. From further frequency shift calculations we have seen that the dipole-induced dipole model provides the main contribution to the frequency shifts.

REFERENCES

1. T. A. Beu, K. Takeuchi, J. Chem. Phys. 103, 6394 (1995).
2. D. Eichenauer, R. J. Le Roy, J. Chem. Phys. 88, 2899 (1988).
3. R. A. Aziz, M. J. Slaman, Mol. Phys. 58, 679 (1986).
4. R. T. Pack, J. J. Valentini, J. B. Cross, J. Chem. Phys. 77, 5486 (1982).
5. Van Bladel, J. W. I., Van der Avoird, A., J. Chem. Phys. 92, 2837 (1989).
6. M. A. Spackman, J. Chem. Phys. 85, 6579 (1986).

STUDIA UNIVERSITATIS BABES-BOLYAI, PHYSICA, XLII, 2, 1997

DOUBLE TO SINGLE ELECTRON DETACHMENT CROSS SECTIONS RATIO FOR THE H^- ION

D. BODEA[1]

ABSTRACT. A simple model for the double electron detachment from the H^- negative ion is developed as a combination of the single electron detachment model and the ionization of the atomic Hydrogen. We used the mixed model of quantum tunnelling and classical field ionization for the single electron detachment from H^- ion and the measurements of Shah el al. [1] for the ionization of the atomic hydrogen.

1. INTRODUCTION

Although the double ionization of H^- by electron impact is one of the simplest multiple ionization processes, it has not been paid attention from a theoretical point of view, nor from an experimental one.

The theoretical description of electron impact double detachment is a knotty subject in atomic physics: four free charged particles (one ion and three electrons) interact with each other via the long range Coulomb potential, so that the main difficulty lies in the correct treatment of this many-body problem. Since Tweed's tentative work [2], to the author knowledge, no decisive theoretical results has been reported.

The early simple approaches, such as the Bethe Born approximation (Byron and Joachain 1967 [3]), only gave a description of the asymptotic behaviour of cross sections for individual cases. The high energy limit of the Born approximation was nevertheless proved to be equivalent to the sudden approximation [4]. An important conclusion drawn from the Bethe Born approximation is that the cross section of the double ionization is extremely sensitive to the choice of the electron correlation terms in the target wavefunctions.

---

[1] University of Cluj, Department of Atomic Physics, 3400 Cluj-Napoca, Romania

2. THEORY

Owning the simple structure of H^-, no indirect process is expected to play any role. We choose a very simple approach as an independent electron picture. The double detachment cross section in this picture can be written:

$$\sigma_{dd} = 2\pi \int_0^\infty b\,db\,P_D(b)P_I(b) \qquad (1)$$

Here both P_D and P_I are impact-parameter-dependent detachment probabilities. P_D stand for the first electron detachment and P_I for the second electron detachment.

Because the first detachment probability does not depend effectively to much on b [5], we may obtain, as suggested by Jamison and Richard [6], a qualitative understanding in a peaking approximation:

$$\sigma_{DD}(E) \cong P_D(b=0,E)\sigma_I(E) \qquad (2)$$

where E is the impact projectile energy and $\sigma_I(E)$ is the cross section for the detachment of the second electron.

The first step to obtain the double detachment cross section is to calculate the first electron detachment probability. In order to do this, we combine the quantum tunnelling model, developed by Smirnov and Chibisov [7], with the classical escape from the barrier model, improved by Ostrovsky and Taulbjerg [8].

2.1 Quantum tunnelling model

Describing the motion of the incident particle by a classical time dependent trajectory, it is natural to represent the electron detachment process as a quasi-static decay of the initial state of the negative ion. At each moment of time the process is characterized by some decay rate Q(t). The probability $P_b(t)$ that the ionic electron remains bound is accordingly determined by the usual rate equation:

$$dP_b = -Q(t)P_b(t)dt \qquad (3)$$

The probability of electron detachment is therefore obtained as:

$$P_D = 1 - \exp(-\int_{-\infty}^{\infty} Q(t)dt) \qquad (4)$$

The expression for the quantum tunnelling rate was obtained by Smirnov and Chibisov [7] assuming that the energy of the quasi-bound state is well below the top of the potential barrier. It has the form:

$$Q_{tun}(R) = \frac{B^2}{2kR^2}\exp\left[-\frac{4}{k}f\left(\frac{1}{2}k^2R\right)\right]\theta\left(\frac{1}{2}k^2R\right) \qquad (5)$$

with

$$f(x) = x\left[\frac{\sin^{-1}\sqrt{x}}{\sqrt{x(1-x)}} - 1\right] \qquad (6)$$

and

$$\theta(x) = 1 \quad \text{for} \quad x < 1, \quad \theta(x) = 0 \quad \text{for} \quad x > 1$$

Here k is related to the electron affinity $\in$ ($\in = \kappa^2/2$) and B is a parameter in the asymptotic form of the wavefunction for the outer (weakly bound) s-electron in the negative ion [8].

In order to trace the validity of the Smirnov-Chibisov model, the essential condition is that the perturbing effect of the field of the projectile is significantly smaller than the affinity of the negative ion,

$$\frac{d}{R^2} << \varepsilon \qquad (7)$$

where 2d is a typical diameter of the ion.

2.2. Classical escape above the barrier top

The classical escape rate is given by the following expression [8]:

$$Q_{cl}(R) = \frac{1}{T}(1 - \frac{R^2}{R_{C^2}}) \qquad (8)$$

where T is the classical period of the radial electron motion.

The decay rate is obtained using the polarized core potential suggested by Cohen and Fiorentini [9],

$$V_{pc} = -\left(1+\frac{1}{r}\right)\exp(-2r) - \frac{9}{4r^4}\exp\left(\frac{-2.547}{r^2}\right) \tag{9}$$

Here the first term describes the interaction of a point charge with a hydrogenic frozen core while the second term is the polarization potential.

Accordingly to Ostrovsky and Taulbjerg there is a good matching between those two models. The tunnelling result becomes invalid below the classical effective threshold when classical escape is possible. The effective threshold for over barrier transitions is due to the Coulomb repulsion between the projectile and the negative charged ion. The classical effective threshold is given by

$$E_{th} = \sqrt{\frac{\varepsilon}{d}} = \frac{1}{R_c} \tag{10}$$

where R_C represent the classical reaction sphere.

This allowed to assume that the rate is given by quantum and classical expressions for large and small distances, respectively

$$Q = \begin{cases} Q_{tun}(R)\,\text{for}\,R > R_c \\ Q_{cl}(R)\,\text{for}\,R < R_c \end{cases} \tag{11}$$

2.3. Results and discussions

The evaluation of the quantum tunnelling rate requires a numerical integration although time propagation in the classical decay rate can be done in analytical form [8]. The ionic electron detachment cross section is obtained from the corresponding probability distribution

$$2\pi b P_D(b) \tag{12}$$

in the usual way by numerical integration over impact parameters b.

Being interested only to give a qualitative estimation of the double detachment cross sections and of the ratio between double detachment and single detachment cross sections, we approximate the cross sections for the second electron detachment with the cross sections for the ionization of the atomic Hydrogen. For those one we used in our calculation the data from Shah el al.[1].

Theoretical results for the double detachment cross section are presented in fig. 1 as a function of the impact electron energies in a range started just next to the double detachment threshold (14.6eV) and up to 1000 eV. Our theoretical prediction is compared with experimental data of D.J. Yu et al. [10]. The solid line stand for the present calculation and the circles stand for the experimental data used.

The present results are in a good agreement with the presented cross section data. We didn't consider the partial shielding of the nuclear charge. This is the reason why our evaluation give the maximum value of the cross section a little shifted to the left. It is possible to reconsider the shielding effect by assuming in our calculation an effective charge smaller than 1 experienced by the ejected electron.

This good agreement is coming to confirm that no indirect process is expected to play any role.

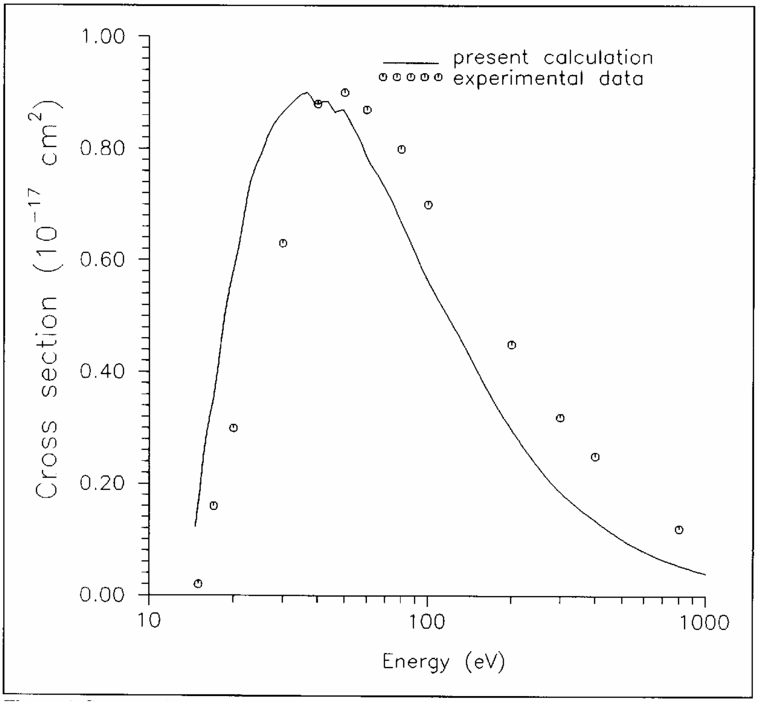

Fig.1. Cross section for the double detachment of the electrons from H^- ion as a function of the impact energy. Solid line stand for present calculation. Circles stand for D.J. Yu experimental data.

In fig. 2 we present the single to double detachment cross sections ratio as a function of the impact electron energy in a range between 14.6 and 1000 eV, together with the data of D. J. Yu el al [10]. They reported only the double detachment cross section and they used for the single to double detachment ratio the experimental results of Peart et al [11].

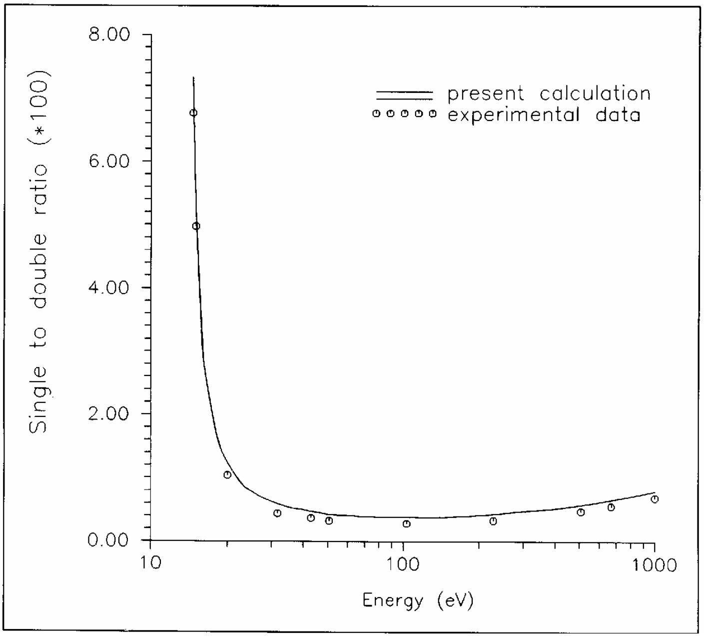

Fig.2. Single to double detachment cross section ratio for the H^- ion as a function of the impact energy. Solid line stand for present calculation. Circles stand for experimental data of D.J. Yu el al [10].

The comparison with the data is not very useful in this case, because the absolute energy scales used are coming from two different experiments. But we still notice a good agreement between our prediction and the experimental values.

We cannot affirm that this ratio approaches a constant value as predicted by the sudden approximation [12]. But this ratio is undoubtedly a slowly varying function, which is consistent with the Bette Born approximation:

$$\rho = \frac{\sigma^{+}}{\sigma^{++}} = \frac{a_1 \ln E + b_1}{a_2 \ln E + b_2} \tag{13}$$

where a_1, b_1, a_2 and b_2 are the asymptotic coefficients for the single ionization cross section, respectively for the double ionization cross section.

Acknowledgments

The author is grateful to Professor Knud Taulbjerg for many fruitful discussions.

REFERENCES

1. M. B. Shah, D. S. Elliot, H. B. Gillbody, Phys. Rev. A, 240, 431 (1981).
2. R. J. Tweed, J. Phys. B. 6, 256 (1973).
3. F. W. Byron, C. J. Joachain, Phys Rev. Lett. 16, 1139 (1966).
4. J. M. Peek, Phys. Rev. A, 160, 214 (1967).
5. A. K. Kazansky, K. Taulbjerg, J. Phys. B, 29, 4465 (1996).
6. K. A. Jamison, P. Richard, Phys. Rev. Lett, 38, 484 (1997).
7. B. M. Smirnov, M. I. Chibisov, Zh. Eksp. Teor. Fiz. 49, 841 (1966).
8. V. N. Ostrovsky, K. Taulbjerg, J. Phys. B, 29, 2573 (1996).
9. S. Cohen, G. Fiorentini, Phys. Rev. A, 5, 2144 (1968).
10. D. J. Yu, S. Rachafi, J. Jureta, P. Defrance, J. Phys. B, 25, 4593 (1992).
11. B. Peart, D. S. Walton and K. T. Dodler, J. Phys. B, 3, 1346 (1970).
12. M. H. Mittleman, Phys. Rev. Lett., 16, 498 (1966).

STUDIA UNIVERSITATIS BABES-BOLYAI, PHYSICA, XLII, 2, 1997

WHISTLER MODE PROPAGATION IN LOW TEMPERATURE MAGNETIC MIRROR CONFINED PLASMA

J. KARÁCSONY[1], L. KENÉZ[1], E. CSOMORTÁNI[2]

ABSTRACT. An anisotropic Maxwellian velocity distribution with loss cones is used to investigate propagation of whistler-mode waves in a magnetic mirror configuration. The density of electrons in the loss cones is assumed to be negligible; this implies that the particle velocity distribution function is such that $f(v_\perp, v_{//}) = 0$ for $|v_z| > v_\perp (R-1)^{1/2}$, where v_z is the component of particle velocity along the magnetic field, $v_\perp$ is the velocity transverse to the magnetic field, and R is the mirror ratio. Expressions are derived for damping and cyclotron growth coefficients of whistlers in low temperature plasma. We consider waves propagating at an angle to the external magnetic field, with the assumption that the propagation itself is unaffected by the finite electron temperature. It is found that due to the finite value of the mirror ratio the Landau damping of whistler-mode waves are more weak that the ones in a plasma with anisotropic Maxwellian distribution without loss-cones. A decreasing mirror ratio favours the cyclotron instability of the waves.

INTRODUCTION

The attention to whistler-mode waves has been mainly stimulated by the important role, which they play both in the space [1,2] and laboratory [3,4] plasmas. The most widely used model for the analysis of whistler-mode propagation was in the framework of a cold electron plasma, where the analysis is the simplest one [5,6]. In general solution of the dispersion equation for whistler-mode waves in hot plasma requires complicated numerical methods [7,8]. An alternative

---

[1] Babes-Bolyai University, Faculty of Physics, 3400 Cluj-Napoca, Romania
[2] West Virginia University, Morgantown, W.V. 26505 USA

analytical approach to the problem is possible when we impose some additional restrictions on the properties of propagating waves. The equation for the increment of instability $(\gamma > 0)$ or decrement of damping $(\gamma < 0)$ appears to be the simplest, if we assume that the plasmas finite temperature does not influence the process of wave propagation and, in particular, the value of the wave refracting index *N* [9,10]. The validity of this assumption for whistler-mode propagation in different plasma models has been extensively studied by Sazhin in a series of papers [11-14]. The expressions for the increment of instability or decrement of damping taking into account both non-zero electron temperature and anisotropy of the electron distribution function has been obtained for a bi-Maxwellian plasma by Kennel [9], and modified by Sazhin [15]. Our paper deals with the calculation of the above-mentioned coefficients for a loss-cone distribution in order to include mirror loss-cone effects. The analysis is applicable both to plasma confined in magnetic mirror configurations and in the Earth's magnetosphere.

GENERAL EXPRESSIONS FOR GROWTH AND DAMPING COEFFICIENTS

Assuming that in the plasma only plane waves are propagating, i. e. the perturbed quantities are proportional to $\exp[i(\vec{k}\vec{r} - \omega t)]$, the general dispersion equation will be written in the form [16]

$$D \equiv AN^4 + BN^2 + C = 0 \tag{1}$$

where $N = kc/\omega$ is the wave refractive index and the coefficients A, B and C are defined as:

$$A = \varepsilon_{11}\cos^2\theta + 2\varepsilon_{12}\sin\theta\cos\theta + \varepsilon_{33}\cos^2\theta \tag{2}$$

$$\begin{aligned} B = -\varepsilon_{11}\varepsilon_{33} - (\varepsilon_{22}\varepsilon_{33} + \varepsilon_{23}^2)\cos^2\theta - (\varepsilon_{11}\varepsilon_{22} + \varepsilon_{12}^2)\sin^2\theta + \\ +2(\varepsilon_{12}\varepsilon_{23} - \varepsilon_{22}\varepsilon_{13})\sin\theta\cos\theta + \varepsilon_{13}^2 \end{aligned} \tag{3}$$

$$C = \varepsilon_{33}(\varepsilon_{11}\varepsilon_{22} + \varepsilon_{12}^2) + \varepsilon_{11}\varepsilon_{23}^2 + 2\varepsilon_{12}\varepsilon_{13}\varepsilon_{23} - \varepsilon_{22}\varepsilon_{13}^2 \tag{4}$$

(is the waves normal angle and ε_{ij} (i,j=1,2,3) are the elements of the plasma dielectric tensor.

If we restrict ourself to the non-relativistic approximation (which is justified when $N^2 >> 1$ [11]) one should take into account only the electrons contribution to ε_{ij}, and assume that the electrons distribution function depends only on the parallel and perpendicular components of the electron velocity ($v_{//}$ and $v_{\perp}$). The expressions for ε_{ij} will be then written as [16]:

$$\varepsilon_{ij} = \delta_{ij} + 2\pi \sum_{n=-\infty}^{\infty} \frac{\Pi^2}{\omega^2} \left\{ \int_0^{\infty} v_{\perp} dv_{\perp} \int_{-\infty}^{\infty} dv_{//} \left[\left(\frac{\omega - k_{//} v_{//}}{v_{\perp}} \frac{\partial f}{\partial v_{\perp}} + k_{\perp} \frac{\partial f}{\partial v_{//}} \right) \frac{Q_{ij}^{(n)}}{\omega - k_{//} v_{//} - n\Omega} - \right. \right.$$
$$\left. \left. - b_{ij} \left(f + \frac{v_{//}^2}{v_{\perp}} \frac{\partial f}{\partial v_{\perp}} \right) \right] \right\} \tag{5}$$

where

$$Q_{ij}^{(n)} = \begin{pmatrix} \frac{n^2 \Omega^2}{k_{\perp}^2} j_n^2 & i v_{\perp} \frac{n\Omega}{k_{\perp}} j_n j_n' & v_{//} \frac{n\Omega}{k_{\perp}} j_n^2 \\ - i v_{\perp} \frac{n\Omega}{k_{\perp}} j_n j_n' & v_{\perp}^2 j_n'^{\,2} & - i v_{//} v_{\perp} j_n j_n' \\ v_{//} \frac{n\Omega}{k_{\perp}} j_n^2 & i v_{//} v_{\perp} j_n j_n' & v_{//}^{\,2} j_n^2 \end{pmatrix} \tag{6}$$

The arguments of the Bessel functions (j_n) are $\lambda \equiv k_{\perp} v_{\perp} / \Omega$; δ_{ij} is the Kronecker symbol; $b_{ij} = 1$ when $i=j=3$ and $b_{ij}=0$ otherwise; Π is the electron plasma frequency; Ω is the electron cyclotron frequency; f is assumed to be normalised to unity and $k_{\perp(//)}$ is the component of the wave vector in the direction perpendicular (parallel) to the magnetic field. Assuming that

$$\left| \mathrm{Im}(\omega) \right| \equiv \left| \gamma \right| << \min(\omega, \Omega - \omega) \tag{7}$$

Eq. (1) can be written as a system of two-equation [16]:

$$\mathrm{Re}\, D = 0 \tag{8}$$

$$\gamma = -\frac{\operatorname{Im} D}{\frac{\partial}{\partial \omega}(\operatorname{Re} D)} \tag{9}$$

$D \equiv D(\omega,\vec{k})$ with ω real, *ReD* and *ImD* are denoting the real and imaginary part of *D*, respectivelly. Eq. (8) describes wave propagation, while Eq. (9) gives an explicit expression for γ.

Taking into account that for whistler waves $\omega << \Omega$, $N^2>>1$ and assuming that the electron temperature does not influence the wave propagation, the expression for the wave refracting index will be derived within the cold plasma model. As a result, limiting to the second order terms with respect to $Y^{-1}\equiv(\Omega/\omega)^{-1}$, one can write the solution of Eq. (8) as [15]:

$$N^2 = X\left[\frac{1}{Y\cos\theta} + \frac{1}{Y^2\cos^2\theta}\right] \tag{10}$$

where $X=\Pi^2/\omega^2$. Furthermore, if we neglect the influence of thermal effects on the value of $\partial ReD/\partial\omega$ we obtain

$$\frac{\partial}{\partial\omega}(\operatorname{Re} D) = \frac{2X^3}{\omega Y^2}\left(1+\frac{2}{Y\cos\theta}\right) \tag{11}$$

In order to calculate *ImD* we write ε_{ij} *as* [15]

$$\varepsilon_{ij} = \varepsilon_{ij}^{(0)} + \varepsilon_{ij}^{(1)} \tag{12}$$

where $\varepsilon_{ij}^{(0)}$ results from the principal part of the integral with respect to $v_{//}$ in Eq. (15), and $\varepsilon_{ij}^{(1)}$ results from the residues of the same integral. If we neglect the influence of the thermal effects on $\varepsilon_{ij}^{(0)}$ [15] and assume that $Y>>1$ and $X>>1$, then the expressions for $\varepsilon_{ij}^{(0)}$ can be simplified:

$$\varepsilon_{ij}^{(0)} = \begin{pmatrix} \frac{X}{Y^2} & iX\left(\frac{1}{Y}+\frac{1}{Y^3}\right) & 0 \\ -iX\left(\frac{1}{Y}+\frac{1}{Y^3}\right) & \frac{X}{Y^2} & 0 \\ 0 & 0 & -X \end{pmatrix} \tag{13}$$

The expressions for $\varepsilon_{ij}^{(1)}$ follow from Eq. (15) in a straightforward way:

$$\varepsilon_{ij}^{(1)} = -i\frac{2\pi^2 X\omega}{k_{//}}\int_0^\infty dv_\perp \int_{-\infty}^{\infty} dv_{//} G \sum_{n=-\infty}^{\infty} Q_{ij}^{(n)} \delta\left(v_{//} - \frac{\omega - n\Omega}{k_{//}}\right) \tag{14}$$

where

$$G = \frac{\omega - k_{//}v_{//}}{\omega}\frac{\partial f}{\partial v_\perp} + \frac{k_{//}v_\perp}{\omega}\frac{\partial f}{\partial v_{//}} \tag{15}$$

Assuming that $|\varepsilon_{ij}^{(1)}| << |\varepsilon_{ij}^{(0)}|$, unless $\varepsilon_{ij}^{(0)}=0$ and substituting Eqs. (12) and (10) into Eq. (1) and by keeping only the first-order terms with respect to $\varepsilon_{ij}^{(1)}$ we obtain the value of *ImD*. Having substituted this value of *ImD* and $\partial ReD/\partial\omega$ defined by Eq. (11) into Eq. (9), after lenghty but straightforward calculations we obtain [15]:

$$\gamma = \frac{\pi^2\omega^2 Y^2}{k\cos\theta}\int_0^\infty dv_\perp \int_{-\infty}^{\infty} dv_{//} \sum_{n=-\infty}^{\infty} \delta\left(v_{//} - \frac{\omega - n\Omega}{k_{//}}\right) G \sum_{i=1}^{6} \chi_i \tag{16}$$

with

$$\chi_1 = \frac{n^2 v_\perp^2}{\lambda^2} j_n^2 \frac{1}{Y\cos\theta} \quad (17) \qquad \chi_2 = \frac{2v_\perp^2}{\lambda} n j_n j_n' \frac{1}{Y^2} \quad (18)$$

$$\chi_3 = \frac{2n v_{//} v_\perp}{\lambda} j_n^2 \frac{tg\theta}{Y^2} \quad (19) \qquad \chi_4 = \frac{v_\perp^2 j_n'^{\,2} \cos\theta}{Y} \quad (20)$$

$$\chi_5 = \frac{2v_{//} v_\perp j_n j_n' \sin\theta}{Y^2} \quad (21) \qquad \chi_6 = \frac{v_{//}^2 j_n^2 \sin^2\theta}{Y^3 \cos\theta} \quad (22)$$

In deriving Eq. (16) we kept only the lowermost-order terms with respect to Y^{-1} for each group of terms proportional to the elements of $Q_{ij}^{(n)}$ and we assumed that θ was not too close to the resonance cone angle (arccos(Y^{-1})). Now by keeping only the terms χ_1, χ_2 and χ_4,which are of the lowermost order with respect to Y^{-1} among all the terms χ_i, then we obtain [15]:

$$\gamma = \frac{\pi^2\omega\ \Omega}{k}\int_0^\infty v_\perp^2 dv_\perp \int_{-\infty}^{\infty} dv_{//} \sum_{n=-\infty}^{\infty} \delta\left(v_{//} - \frac{\omega - n\Omega}{k_{//}}\right) C_n G \tag{23}$$

where

$$C_n = \left[\frac{(1-\cos\theta)\, j_{n+1} + (1+\cos\theta)\, j_{n-1}}{2\cos\theta} \right]^2 \tag{24}$$

However, when we are interested in Landau damping *(n=0)* the terms χ_1, χ_2 and χ_3 are equal to zero and the term χ_6 cannot be automatically neglected in comparison with χ_4. For a low temperature plasma, when $\lambda << Y^{-1} << 1$ for most of the electrons, the term χ_6 becomes dominant with respect to λ and the term $\gamma(n=0) \equiv \gamma_0$ describing the contribution of the Landau resonance in Eq. (16) will be simplified into:

$$\gamma_0 = \frac{\pi^2 \omega^2 \sin^2\theta}{Yk\cos^2\theta} \int_0^\infty dv_\perp \int_{-\infty}^{\infty} dv_{//} v_{//}^2 G \delta\left(v_{//} - \frac{\omega}{k_{//}} \right) \tag{25}$$

Damping and growth coefficients for loss-cone distribution

In this section in order to calculate the damping and growth coefficients of the whistler modes we will consider an anisotropic Maxwellian velocity distribution for the electrons with loss cones. In this situation there is a lower limit on the perpendicular velocity for a given longitudinal velocity, and an upper limit on the longitudinal velocity classes for particles with a given transverse velocity, both depending on the mirror ratio $R = B_{max} / B_{min}$. The anisotropic Maxwellian distribution function with loss cones for a given longitudinal velocity can be written under the form [17]:

$$f_0(v_\perp, v_{//}) = f_0(v_\perp, v_{//}) H(v_\perp - v_{//}^*) \tag{26}$$

where

$$f_0(v_\perp, v_{//}) = \frac{1}{K\pi^{3/2}\alpha_\perp^2 \alpha_{//}} \exp\left\{ -\left[\left(\frac{v_\perp}{\alpha_\perp} \right)^2 + \left(\frac{v_{//}}{\alpha_{//}} \right)^2 \right] \right\} \tag{27}$$

In the above expression K is the normalization constant so that $\int f d\vec{v} = 1$, and $\alpha_{\perp(//)}$ are the electrons thermal velocities in the direction perpendicular (parallel) to the external magnetic field. $H(v_\perp - v_{//}^*)$ represents the Heaviside function, defined by

$$H(v_\perp - v_{//}^*) = \begin{cases} 1 & for \quad v_\perp > v_{//}^* \\ 0 & for \quad v_\perp < v_{//}^* \end{cases} \tag{28}$$

with

$$v_{//}^* = \frac{|v_{//}|}{(R-1)^{1/2}} \tag{29}$$

The normalization constant *K* is given by the equation

$$K = \int_{-\infty}^{\infty}\int_{v_{//}^*}^{\infty} \frac{1}{\pi^{3/2}\alpha_\perp^2\alpha_{//}} \exp\left\{-\left[\left(\frac{v_\perp}{\alpha_\perp}\right)^2 + \left(\frac{v_{//}}{\alpha_{//}}\right)^2\right]\right\} 2\,\pi v_\perp dv_\perp dv_{//} \tag{30}$$

The result of integration over the transverse and longitudinal velocities is

$$K = \left[\frac{(R-1)A_e}{(R-1)A_e + 1}\right]^{1/2} \tag{31}$$

with

$$A_e = \left(\frac{\alpha_\perp}{\alpha_{//}}\right)^2$$

Now, taking into account expression (15) for *G*, we will write the term γ_0 corresponding to the Landau resonance in the form:

$$\gamma_0 = \frac{\pi^2\omega^2\sin^2\theta}{Yk\cos^2\theta}(I_1 + I_2) \tag{32}$$

where

$$I_1 = \int_{-\infty}^{\infty} dv_{//} v_{//}^2 \frac{\omega - k_{//}v_{//}}{\omega}\delta(v_{//} - \frac{\omega}{k_{//}})\int_0^{\infty} dv_\perp \frac{\partial f}{\partial v_\perp} \tag{33}$$

$$I_2 = \int_{-\infty}^{\infty} dv_{//} v_{//}^2 \delta(v_{//} - \frac{\omega}{k_{//}})\int_0^{\infty} dv_\perp \frac{k_{//}v_\perp}{\omega}\frac{\partial f}{\partial v_{//}} \tag{34}$$

The first integral I_1 is zero. In order to evaluate the second integral I_2, due to the discontinuities at the loss cones it is convenient to split the integral into continuous part and delta distributions. Taking into account (26) and (27) the integral is written

$$I_2=I_{2c}+I_{2d} \tag{35}$$

where

$$I_{2c}=-\frac{2k_{//}}{K\pi^{3/2}\alpha_{\perp}^{2}\alpha_{//}^{3}\omega}\int_{-\infty}^{\infty}dv_{//}v_{//}^{3}\delta(v_{//}-\frac{\omega}{k_{//}})\int_{v_{//}^{*}}^{\infty}dv_{\perp}v_{\perp}\exp\left\{-\left[\left(\frac{v_{\perp}}{\alpha_{\perp}}\right)^{2}+\left(\frac{v_{//}}{\alpha_{//}}\right)^{2}\right]\right\} \tag{36}$$

$$I_{2d}=\frac{k_{//}}{K\pi^{3/2}\alpha_{\perp}^{2}\alpha_{//}^{3}\omega}\int_{-\infty}^{\infty}dv_{//}v_{//}^{2}\delta(v_{//}-\frac{\omega}{k_{//}})\int_{0}^{\infty}dv_{\perp}v_{\perp}\left[\delta(v_{//}+v_{\perp}\sqrt{R-1})-\delta(v_{//}-v_{\perp}\sqrt{R-1}\right]$$
$$*\exp\left\{-\left[\left(\frac{v_{\perp}}{\alpha_{\perp}}\right)^{2}+\left(\frac{v_{//}}{\alpha_{//}}\right)^{2}\right]\right\} \tag{37}$$

For the distribution δ, the lower limit on $v_{\perp}$ was extended to zero without changing the value of the integral. The result of the integration in Eq. (36) is

$$I_{2c}=-\frac{\omega^{2}}{K\pi^{3/2}k_{//}^{2}\alpha_{//}^{3}}\exp\left\{-\frac{\omega^{2}}{k_{//}^{2}\alpha_{//}^{2}K^{2}}\right\} \tag{38}$$

In order to evaluate the contribution in the integral due to the delta distribution, first we integrate with respect to $v_{\perp}$. In order to facilitate this operation the arguments of the delta distribution are interchanged. The integral is divided in two parts since $v_{\perp}$ is defined only for values greater then or equal to zero. Equation (37) is written

$$I_{2d}=\frac{k_{//}}{K\pi^{3/2}\alpha_{\perp}^{2}\alpha_{//}\omega}\left[\int_{-\infty}^{0}dv_{//}v_{//}^{2}\delta(v_{//}-\frac{\omega}{k_{//}})\int_{0}^{\infty}dv_{\perp}v_{\perp}\exp\left\{-\left[\left(\frac{v_{//}}{\alpha_{//}}\right)^{2}+\left(\frac{v_{\perp}}{\alpha_{\perp}}\right)^{2}\right]\right\}\delta(v_{\perp}\sqrt{R-1}+v_{//})\right]-$$
$$-\frac{k_{//}}{K\pi^{3/2}\alpha_{\perp}^{2}\alpha_{//}\omega}\left[\int_{0}^{\infty}dv_{//}v_{//}^{2}\delta(v_{//}-\frac{\omega}{k_{//}})\int_{0}^{\infty}dv_{\perp}v_{\perp}\exp\left\{-\left[\left(\frac{v_{//}}{\alpha_{//}}\right)^{2}+\left(\frac{v_{\perp}}{\alpha_{\perp}}\right)^{2}\right]\right\}\delta(v_{\perp}\sqrt{R-1}-v_{//})\right] \tag{39}$$

The result of the integration over $v_{\perp}$ is:

$$I_{2d} = \frac{k_{//}}{K\pi^{3/2}\alpha_{\perp}^{2}\alpha_{//}\omega}\left\{-\int_{-\infty}^{0} dv_{//}\delta(v_{//}-\frac{\omega}{k_{//}})\frac{v_{//}^{3}}{R-1}\exp\left[-\left(\frac{v_{//}}{\alpha_{//}K}\right)^{2}\right]-\int_{0}^{\infty} dv_{//}\delta(v_{//}-\frac{\omega}{k_{//}})\frac{v_{//}^{3}}{R-1}\exp\left[-\left(\frac{v_{//}}{\alpha_{//}K}\right)^{2}\right]\right\} \tag{40}$$

Equation (39) can now be expressed as an integral over $v_{//}$

$$I_{2d} = -\frac{k_{//}}{K\pi^{3/2}\alpha_{\perp}^{2}\alpha_{//}\omega}\int_{-\infty}^{\infty} dv_{//}\delta(v_{//}-\frac{\omega}{k_{//}})\frac{v_{//}^{3}}{R-1}\exp\left[-\left(\frac{v_{//}}{\alpha_{//}K}\right)^{2}\right] \tag{41}$$

The result of the integration over $v_{//}$ is

$$I_{2d} = -\frac{\omega^{2}}{K\pi^{3/2}\alpha_{\perp}^{2}\alpha_{//}k_{//}^{2}(R-1)}\exp\left\{-\frac{\omega^{2}}{k_{//}^{2}\alpha_{//}^{2}K^{2}}\right\} \tag{42}$$

If Eq. (42) is added to Eq. (38), the second integral becomes:

$$I_{2} = -\frac{\omega^{2}}{K\pi^{3/2}\alpha^{3}{}_{//}k_{//}^{2}}\exp\left\{-\frac{\omega^{2}}{k_{//}^{2}\alpha_{//}^{2}K^{2}}\right\} \tag{43}$$

Inserting this result in to (32) we obtain for the Landau resonance the expression

$$\gamma_{0} = -\frac{\sqrt{\pi}\omega\sin^{2}\theta}{YN^{3}K^{3}\overline{\alpha}_{//}^{3}\cos^{4}\theta}\exp\left\{-\frac{\omega^{2}}{k_{//}^{2}\alpha_{//}^{2}K^{2}}\right\} \tag{44}$$

where $\overline{\alpha_{//}} = \alpha_{//}/c$

In the limit of an infinite mirror ratio, *K=1* and Eq. (44) reduces to Sazhin's result for an anisotropic Maxwellian plasma without loss cones [15]. However, we remark that for a finite value of mirror ratio our expression for γ_0 predicts a more weak Landau damping of oblique whistler-mode waves than the one given by the corresponding expression for an anisotropic maxwellian distribution without loss-cones. As the mirror ratio approaches unity γ_0 becomes zero. No thermal velocity effects are found in this limit since any longitudinal velocity causes the particles to escape from the system.

On the other hand, having substituted expression (26) into Eq. (23) and evaluating the integrals for a low temperature plasma, when $\lambda<<1$, in a similar manner we made it above, for the contribution of the term corresponding to *n=1* we obtain:

$$\gamma_1 = -\frac{\sqrt{\pi}\,\omega Y(1+\cos\theta)^2}{4KN\overline{\alpha}_{//}\cos^2\theta}\left[Y+(1-Y)\left(\frac{\xi_1^2}{R-1}+A_e\right)\right]\exp(-\xi_1^2) \qquad (45)$$

where $\xi_1 = (\omega - \Omega)/k_{//}\alpha_{//}K$.

Expression (45) reduces to the one given by Sazhin [15] in the limit of an infinite mirror ratio.

From Eq. (45) we can deduce that γ_1 can describe either wave damping ($\gamma<0$) or growth ($\gamma>0$). Remembering that $Y>>1$ for whistler mode waves, we obtained that the waves will be damped when

$$A_e < \frac{k_{//}^2 r_L^2 (R-1)^2 - 1}{[k_{//}^2 r_L^2 (R-1)+1](R-1)} \qquad (46)$$

($r_L = \alpha_\perp / \Omega$ is the electron gyroradius).

The whistler waves propagating through low temperature plasma are amplified when

$$A_e > \frac{k_{//}^2 r_L^2 (R-1)^2 - 1}{[k_{//}^2 r_L^2 (R-1)+1](R-1)} \qquad (47)$$

and $|\gamma_1|>|\gamma_0|$.

In the limit of an infinite mirror ratio, we got a well known result for a bi-maxwellian plasma: the necessary condition for wave growth can be written as $A_e>1$, or using the more conventional notation of electron temperature, as $T_\perp>T_{//}$. The instability condition (47) shows that a decreasing mirror ratio leads to cyclotron instabilities of whistler-mode waves even in the case when $T_\perp<T_{//}$. As the mirror ratio is decreased, the system becomes more unstable due to the cyclotron instabilities of whistler mode.

CONCLUSIONS

It is pointed out that for low temperature anisotropic Maxwellian plasma including mirror loss-cone effect, the damping and growth coefficients depends on the mirror ratio. In the limit of an infinite mirror ratio our expressions for the decrement of damping and increment of instability reduces to the earlier deduced results of Sazhin [15]. Due to the finite value of mirror ratio the Landau damping of whistler-mode waves are more weak that into a plasma with anisotropic Maxwellian distribution without loss-cones. From the instability condition deduced by us results that a decreasing mirror ratio favors the cyclotron instabilities of whistler-mode waves.

Acknowledgment

One of the authors (J. Karácsony) would like to thank the Hungarian Academy of Sciences for fellowships held while the investigation in this work was being performed.

REFERENCES

1. Y. Omura, D. Nunn, H. Matsumoto, M. J. Rycroft, *J. Atomos, Terr. Phys*. 53, 351 (1991).
2. S. S. Sazhin, M. Hayakawa, K. Bullough, *Ann. Geophys*. 10, 293 (1992).
3. F. F. Chen, *Plasma Phys. Control*. Fusion 33, 339 (1991).
4. A. Komori, T. Shoji, K. Miyamoto, J. Kawai, Y. Kawai, *Phys. Fluids B.* 3, 893 (1991).
5. G. E. Stott, *J. Atmos. Terr. Phys*. 45, 219 (1983).
6. J. Heading, *J. Atmos. Terr. Phys*. 46, 1169 (1984).
7. S. S. Sazhin, A. E. Sumner, N. M. Temme, *J. Plasma Phys.* 47, 163 (1992).
8. N. M. Temme, A. E. Sumner, S. S. Sazhin, *Astrophys. Space*. *Sci*. 194, 173 (1992).
9. C. F. Kennel, *Phys. Fluids* 9, 2190 (1966).
10. S. S. Sazhin, *Ann. Geophys.* 38, 111 (1982).
11. S. S. Sazhin, *J. Plasma Phys.* 37, 209 (1987).
12. S. S. Sazhin, *Planet. Space. Sci*. 36, 663 (1988).
13. S. S. Sazhin, *Planet. Space. Sci*. 36, 667 (1988).
14. S. S. Sazhin, A. E. Summer, N. M. Temme, F. Gugic, *Plasma Phys. Control. Fusion* 35, 117 (1993).
15. S. S. Sazhin, *Ann. Geophys*. 9, 690 (1991).
16. A. I. Akhiezer, I. A. Akhiezer, R. V. Polovin, A. G. Stienko, K. N. Stepanov, *Elektrodinamika plazmy*, Nauka, Moskva, 1974.
17. J. E. Scharer, *Phys. Fluids* 10, 652 (1967).

STUDIA UNIVERSITATIS BABES-BOLYAI, PHYSICA, XLII, 2, 1997

CHAOS IN A NONLINEAR DYNAMO MODEL (I)

S. CODREANU[1], M. F. DANCA[2]

ABSTRACT. A model of the magnetic field reversals of the earth is analitically and numerically studied.

INTRODUCTION

It is known that the magnetic pole reversals of the earth have taken place in an irregular manner. To study a such behavior, different dynami models have been proposed [1], [2]. In this work we get a detalied analitical and numerical analysis of a nonlinear dynamo model.

DYNAMO MODEL

The mechanism of the reversal of the earth's magnetic field can be ilustrated by dynamo configuration depicted in Fig. 1. Two conducting rotating disc are connected to two coils so that the current in each coil feeds the magnetic field of the other. Each circuit has the same self-inductance L and resistence R and the discs are driven by the same constant torque G.

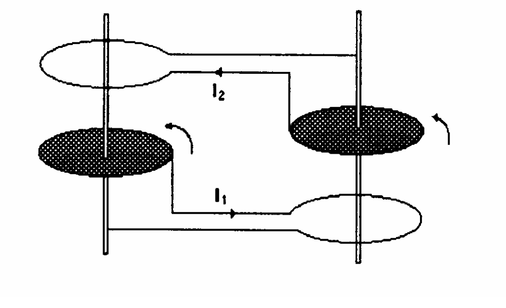

FIg. 1. Diagram of the dynamic

---

[1] Babes-Bolyai University, Dept. of Theoretical Physics, Cluj-Napoca, Romania
[2] Spiru Haret High School, Cluj-Napoca, Romania

The currents I_1 and I_2 in the circuits and the voltages V_1 and V_2 are connected by the well known relations for the R, L circuits:

$$\begin{aligned} RI_1 + L\frac{dI_1}{dt} &= V_1 \\ RI_2 + L\frac{dI_2}{dt} &= V_2 \end{aligned} \tag{1}$$

The voltage generated in each circuit depends on the magnetic field set up by the current in the other. Furthermore, the current in each coil sets up a magnetic field $\overline{B}$, which cuts the corresponding discs in a perpendicular manner.

As the disc rotates through an angle θ, the flux along the radial direction is

$$\Phi = \theta \int_0^{\rho} Brdr = \alpha\theta \tag{2}$$

where α is the value of the integral and ρ is the disc ray.

Thus we can appreciate V_1 and V_2 as

$$V_1=\alpha_1\omega_1 \qquad \text{and } V_2=\alpha_2\omega_2 \tag{3}$$

where $\omega_1=d\theta_1/dt$ and $\omega_2=d\theta_2/dt$ are the angular velocities of the rotating discs.

But, the value of the integral in (2) depends on the current, because the magnetic field changes with I. We can write α_1 and α_2 as:

$$\alpha_1 = MI_2 \qquad \alpha_2 = MI_1 \tag{4}$$

where M is the mutual inductance.

The system of equations (1) becomes

$$\begin{aligned} RI_1 + L\frac{dI_1}{dt} &= MI_1\omega_1 \\ RI_2 + L\frac{dI_2}{dt} &= MI_2\omega_2 \end{aligned} \tag{5}$$

Let consider C the moment of inertia of each disc. Then the rotational torque of one disc is

$$C\frac{d\omega_1}{dt} = G - \alpha_1 I_1$$

or

$$C\frac{d\omega_1}{dt} = G - MI_1 I_2 \tag{6}$$

where G is the constant applied torque and the last term is the opposing magnetic torque.

Symilarly to (6), for the other disc we can write

$$C\frac{d\omega_2}{dt} = G - MI_2 I_1 \tag{7}$$

From (6) and (7) it is easy to see that

$$\omega_1 - \omega_2 = \text{ constant} \tag{8}$$

The system of equations (5-7) can be rescaled if we consider

$$\begin{aligned} I_{1,2} &= \left(\frac{G}{M}\right)^{1/2} x_{1,2} \\ \omega_{1,2} &= \left(\frac{GL}{CM}\right)^{1/2} x_{3,4} \end{aligned} \tag{9}$$

and

$$t = \left(\frac{CL}{GM}\right)^{1/2} \tau$$

We can also assign the constant in (8) as

$$\omega_1 - \omega_2 = \left(\frac{GL}{CM}\right)^{1/2} b \tag{10}$$

it follows that

$$\begin{aligned}\frac{dx_1}{d\tau} &= x_2x_3 - ax_1\\ \frac{dx_2}{d\tau} &= x_1x_4 - ax_2\\ \frac{dx_3}{d\tau} &= 1 - x_1x_2\\ \frac{dx_4}{d\tau} &= 1 - x_1x_2\end{aligned} \qquad (11)$$

with

$$a = R\left(\frac{LC}{GM}\right)^{1/2}$$

By taken into account, from (9) and (10), that

$$x_3 - x_4 = b$$

the system (11)becomes a system of autonomous differential equations:

$$\begin{aligned}\overset{o}{X}_1 &= x_2x_3 - ax_1\\ \overset{o}{X}_2 &= x_1(x_3 - b) - ax_2\\ \overset{o}{X}_3 &= 1 - x_1x_2\end{aligned} \qquad (12)$$

where the dot means d/dr.

BEHAVIOUR PF THE AUTONOMOUS SYSTEM

The nonlinear system (12), written as

$$\overset{0}{\vec{X}} = \vec{f}\left(\vec{X}\right) \qquad (13)$$

with $\vec{X}(x_1,x_2,x_3)$, allows a chaotic behaviour. Furthermore $\nabla\ \vec{f} < 0$ for $a > 0$. This means that the volume in the phase space contracts and the system has an attractor.

The fixed points (the equilibrium stateas) of the system are found by setting the righthand side of the vector equation (13) equal zero. We obtain

$$\overset{\rightarrow *}{X}_{1,2}\left(\pm k_1, \pm\frac{1}{k_1}, ak_1^2\right) \quad \text{with} \quad k_1^2 = \frac{1}{2a}\left(b + \sqrt{b^2 + 4a^2}\right)$$

and (14, 15)

$$\overset{\rightarrow *}{X}_{3,4}\left(\pm k_2, \pm\frac{1}{k_2}, ak_2^2\right) \quad \text{with} \quad k_2^2 = \frac{1}{2a}\left(b + \sqrt{b^2 + 4a^2}\right)$$

We will retain only the fixed points $\overset{\rightarrow *}{X}_{1,2}$, because $\overset{\rightarrow *}{X}_{3,4}$ are unvalid for a > 0. The stability of the equilibrium states $\overset{\rightarrow *}{X}_{1,2}$ is investigated with the usual linearized technique. Thus the Jacobian of the linearized system about $\overset{\rightarrow *}{X}_{1,2}$ is:

$$\begin{bmatrix} -a & ak^2 & \frac{1}{k} \\ \frac{a}{k^2} & -a & k \\ -\frac{1}{k} & -k & 0 \end{bmatrix} \tag{16}$$

where we made the notation $k_1 = k$.

The corresponding eigenvalues equation has the form:

$$\lambda^3 + 2a\lambda^2 + \left(k^2 + \frac{1}{k^2}\right)\lambda + 2a\left(k^2 + \frac{1}{k^2}\right) = 0 \tag{17}$$

with the solutions:

$$\lambda_1 = -2a$$

(18)

$$\lambda_{2,3} = \pm i\left(k^2 + \frac{1}{k^2}\right)^{1/2}$$

The eigenvalues $\lambda_{2,3}$ have zero real parts. It follows that the fixed points $\overset{\rightarrow *}{X}_{1,2}$ are not hyperbolic and we cannot say anything about the system by means of linearization. To obtain informations about the behaviour of this nonlinear system, a numerical integration of the equations is necessary.

NUMERICAL INTEGRATION

The system of equation (12) has been numerically integrated by using the Local Iterative Linearization (LIL) method, decribed in [6], [7]. It shows that the system has different behaviour for different values of the parameters and that there is a sensible dependence of the initial conditions. This sensibility can be seen, for example, in the Figures 2 (a,b) for the same values of the parameters a and b, but with a slight difference of the initial conditions. It seems that the orbit chosses an equilibrium or another from $\overset{\rightarrow *}{X}_{1,2}$.

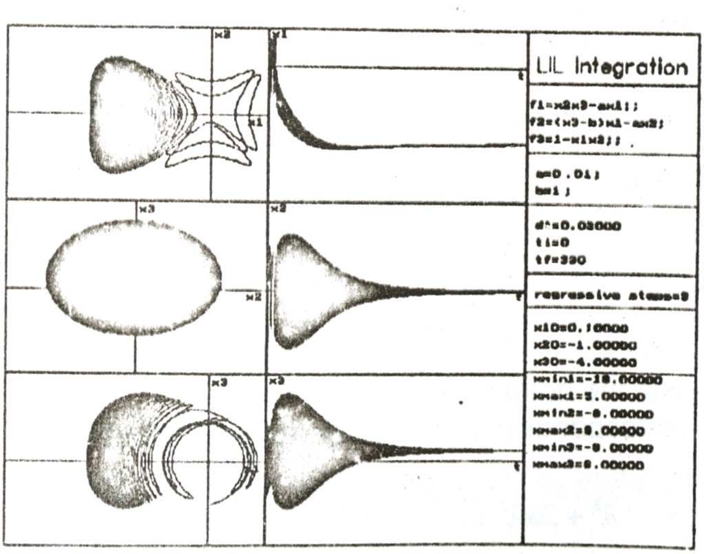

```
LIL Integration
f1=x2x3-ax1;;
f2=(x3-b)x1-ax2;
f3=1-x1x2;;
a=0.01;
b=1;
d^=0.02000
ti=0
tf=390
regressive steps=9
x10=0.10000
x20=-1.00000
x30=-4.00000
xmin1=-10.00000
xmax1=5.00000
xmin2=-8.00000
xmax2=8.00000
xmin3=-8.00000
xmax3=8.00000
```

Fig. 2a An equilibrium state of the system

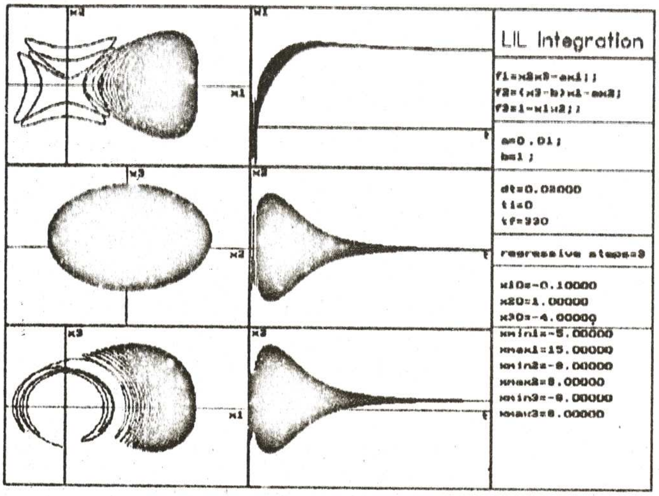

Fig. 2b. An equilibrium state of the system

For another values of the parameters, the behavior of the system is oscillatory. This can be observed in the Figure 3, where the projections of the orbit on the phase planes are the limit cycles. The values of the parameters and also the initial conditions are indicated on the figure.

We have obtained also the chaotic behaviour of the system. As can be seen from the Figure 4, the orbit encircle one fixed point a number of times, then switches to encircle the other one and sudden switches again back. The number of the encircles about a fixed point and also the switching are unpredictible. The orbits are never captured by either fixed point and the limiting behaviour is chaotic.

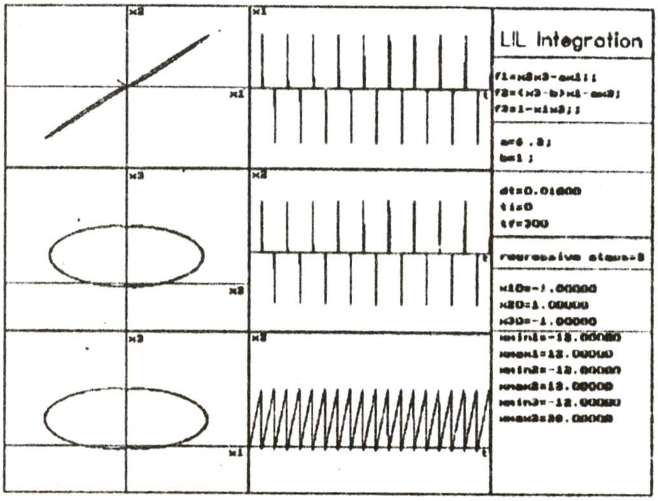

```
f1=x2x3-ax1;;
f2=(x3-b)x1-ax2;
f3=1-x1x2;;
a=6 .3;
b=1 ;
dt=0.01000
ti=0
tf=300
regressive steps=3
x10=-1.00000
x20=1.00000
x30=-1.00000
xmin1=-12.00000
xmax1=12.00000
xmin2=-12.00000
xmax2=12.00000
xmin3=-12.00000
xmax3=20.00000
```

Fig.3. A limit-cycle of the system

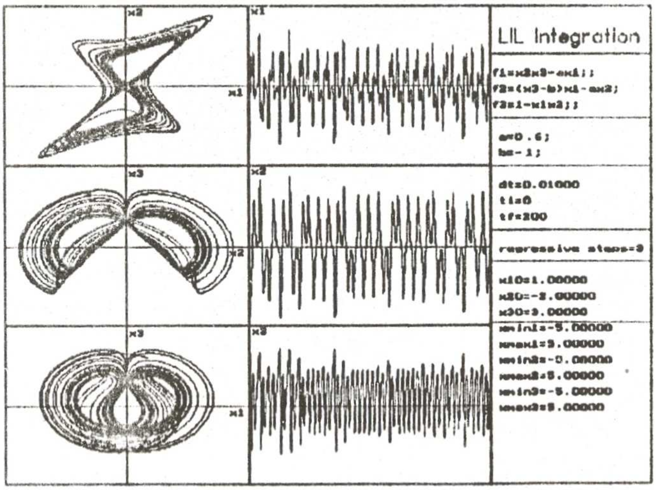

```
f1=x2x3-ax1;;
f2=(x3-b)x1-ax2;
f3=1-x1x2;;
a=0 .6;
b=- 1;
dt=0.01000
ti=0
tf=200
regressive steps=3
x10=1.00000
x20=-2.00000
x30=3.00000
xmin1=-5.00000
xmax1=5.00000
xmin2=-5.00000
xmax2=5.00000
xmin3=-5.00000
xmax3=5.00000
```

Fig.4. The chaotic behaviour of the system

CONCLUSIONS

In this work we present a study of a nonlinear dynamo model for the mechanism of the reversal of the eart's magnetic field. The analysis reveals a rich behaviour of the considered system, which depends on the values of the parameters. The equilibrium states are unstable and the orbits spiral outward from one fixed point for some time, then switch to spiraling outward from other unstable fixed point. The limiting behaviour of the system is chaotic.

REFERENCES

1. A. E. Cook, P. H. Roberts, *The Rikitake Two-Disc Dynamo System*, Proc. Camb. Phil. Soc. 68, 547, 1970.
2. E. C. Bullard, *The Disc Dynamo,* Am. Inst. of Physics Conf. Proc. 46, 373, 1978.
3. L. Kvasz, D. Sokoloff, A. Shukurov, *A steady state of the disc dynamo,* Geophysicaland Astrophysical Fluid Dynamics, vol. 65, Nr.1, 231, 1992.
4. W. Marzocchi, G. Gonzato, F. Mulargia, *Rikitake geodynamomodel analysed in terms of classical time*, series statistics, Physics of the Earth and Planetary Interiors vol. 88, Nr. 2, 83, 1995.
5. R. Hide, *Structural instability of the Rikitake disc dynamo*, Geophysical Research Lettersvol. 22, Nr. 9, 1057, 1995.
6. T. Coloşi, S. Codreanu, I. Naşcu, S. Darie, *Numerical modeling and stimulations of dynamical systems,* ed. Casa Cărţii de Ştiinţă, 1995.
7. M. F. Danca, doctorthesis, *Technical University of Cluj, 1997.*

STUDIA UNIVERSITATIS BABES-BOLYAI, PHYSICA, XLII, 2, 1997

CHAOS IN A NONLINEAR DYNAMO MODEL (II)

M. F. DANCA[1], S. CODREANU[2]

ABSTRACT. A model of the magnetic field reversals of the earth, which presents a chaotic behavior, is analysed and a procedure of suppression of chaos is presented.

INTRODUCTION

The irregularity of the magnetic pole reversals of the earth is nowadays studied by means of the models. One of them is presented in the part I of this work. As can be observed, this model, as a nonlinear system of three autonomous differential equations, can display a rich dinamics, including a chaotic behavior.

Because the system cannot be investigated by means of usual linearization, we used a numerical integration of the equations, which was quite revealing. For different values of the system parameters, there are different behavior. The most interesting behavior is the bistable pole-reversing one, that is aperiodic. A possible stabilization can be obtain by using a control procedure, which acts on the system variables.

NUMERICAL RESULTS

The model is described by the flow:

$$\begin{aligned} \overset{o}{x}_1 &= x_2 x_3 - a x_1 \\ \overset{o}{x}_2 &= x_1 (x_3 - b) - a x_2 \\ \overset{o}{x}_3 &= 1 - x_1 x_2 \end{aligned} \qquad (1)$$

where *a* and *b* are the constant parameters. The system is a dissipative one if *a* > 0, so we have chose only the positive values of *a*.

---

[1] Spiru Haret High School, Cluj-Napoca, Romania
[2] Babeş-Bolyai University, Dept. of Theoretical Physics, Cluj-Napoca, Romania

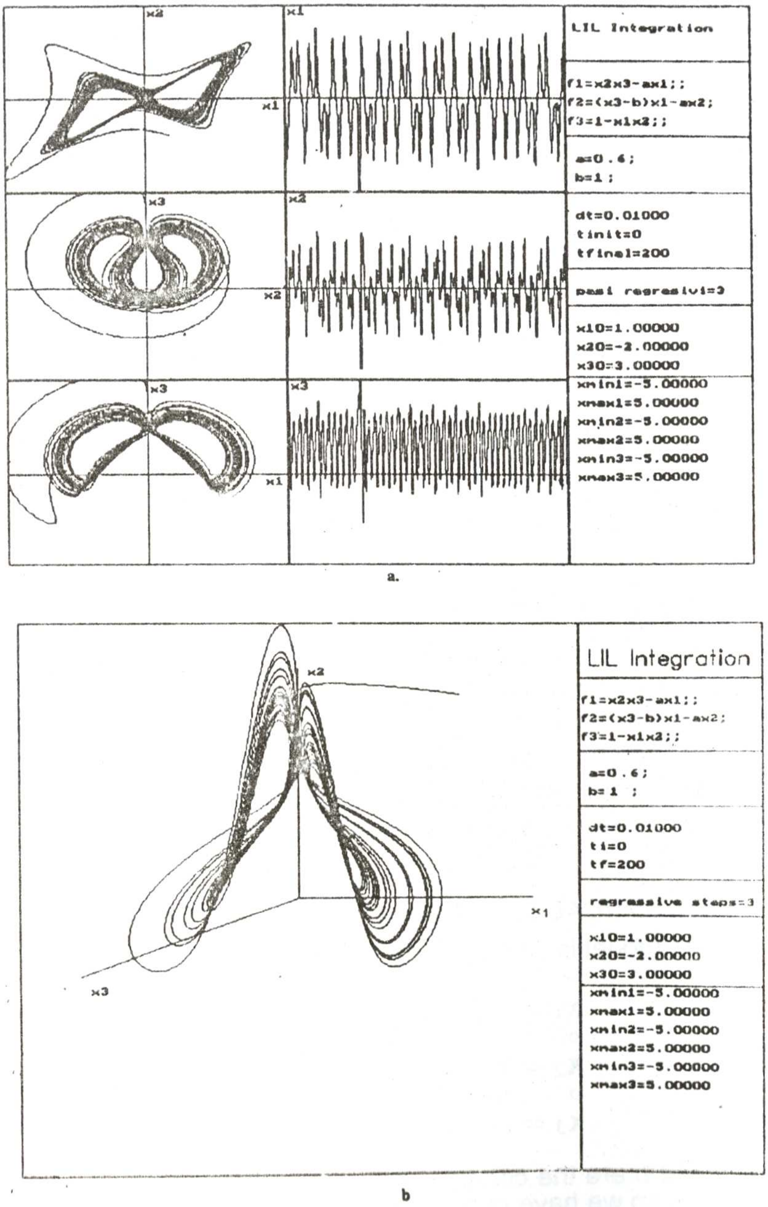

```
LIL Integration

f1=x2x3-ax1;;
f2=(x3-b)x1-ax2;
f3=1-x1x2;;

a=0.6;
b=1;

dt=0.01000
tinit=0
tfinal=200

pasi regresivi=3

x10=1.00000
x20=-2.00000
x30=3.00000
xmin1=-5.00000
xmax1=5.00000
xmin2=-5.00000
xmax2=5.00000
xmin3=-5.00000
xmax3=5.00000
```

```
LIL Integration

f1=x2x3-ax1;;
f2=(x3-b)x1-ax2;
f3=1-x1x2;;

a=0.6;
b= 1  ;

dt=0.01000
ti=0
tf=200

regressive steps=3

x10=1.00000
x20=-2.00000
x30=3.00000
xmin1=-5.00000
xmax1=5.00000
xmin2=-5.00000
xmax2=5.00000
xmin3=-5.00000
xmax3=5.00000
```

Fig. 1 (a, b). A chaotic orbit of the dynamo system:
a - projections in the phase planes; b - orbit in the the 3-dimensional phase space.

The numerical integration of the equations, by means of the LIL technique [1], [2] revealed a chaotic behavior for some values of the parameters. Figure 1 (a, b) shows the projections of the phase space orbit in the phase plans and also the orbit in the 3-dimensional phase plane. The orbit spirals outward from one unstable fixed point for some time, then switches to spiraling outward from the other unstable fixed point.

The number of circuits around of each point is unpredictable and the limiting behavior is chaotic. (This dynamics is similar to those of the well known Lorentz model [3]).

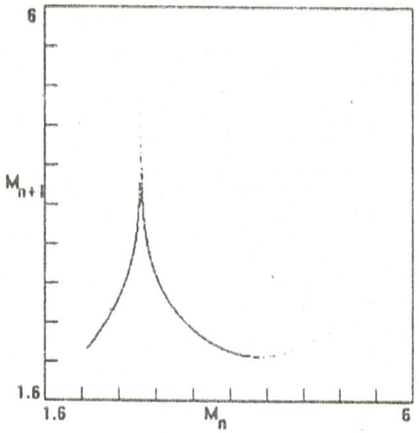

Fig. 2. An approximate one dimensional map function

One way of analysing this motion is to obtain the sequence M_n of the nth maximum of the function $x_3(t)$.The points M_n of this sequence form a return map. In the Figure 2 we have plotted M_{n+1} versus M_n. One can see that the points tend to fall on an approximate one-dimensional map function. Furthermore the magnitude of the slope $\left| dM_{n+1}/dM_n \right|$ for this map is grater that 1 in the range visited by the orbit. It means that the Lyapunov exponent is positive, which indicates the presence of chaos. We note the similarity with the situation for the tent map [4.]

CONTROL ALGORITHM

It is known that the property of the chaotic systems to be very sensitive to the initial conditions permits the use of small perturbations to control chaos. The idea of controlling deterministic chaos behaviors has been introduced in 1987 by Hübler, Reiser and Lüscher [5]. They have changed the dynamics of the system by adding a suitable term to the driving force, such that the system behavior became a stable periodic motion.

A different control method was proposed by Ott, Grebogi and Yorke (O.G.Y) in 1990 [6]. They have shown that is possible to obtain a regular or periodic behavior by making small time dependent perturbations in some accessible system parameters.

Another method of controlling chaos has been recently proposed by Güémez and Matías (G. M.) [7], [8]. This method allows to stabilize chaotic behaviors by performing changes in the variables of the system.

In this work we have used the G. M. control algorithm, which consists in the application every Δn iterations of a feedback to the system variables x_i of the form.

$$x_i \to x_i(1+\gamma)$$

where γ is the intensity of the feedback, which can be positive or negative.

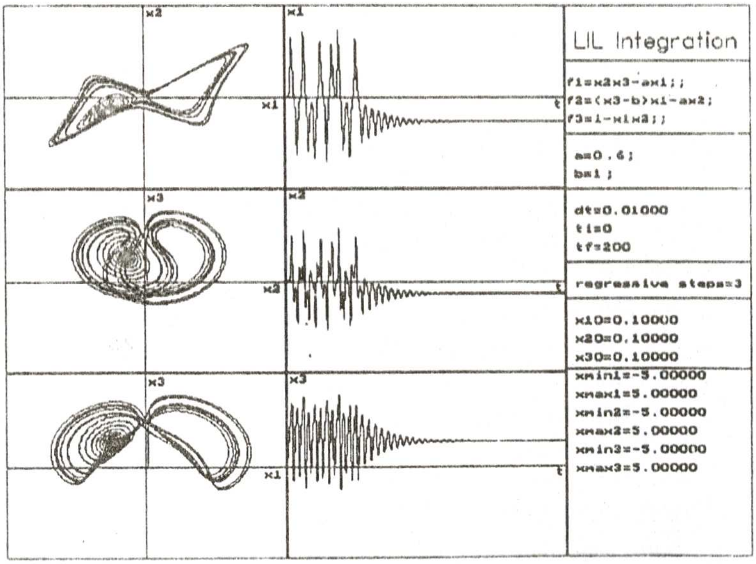

```
f1=x2x3-ax1;;
f2=(x3-b)x1-ax2;
f3=1-x1x2;;
a=0.6;
b=1 ;
dt=0.01000
ti=0
tf=200
regressive steps=3
x10=0.10000
x20=0.10000
x30=0.10000
xmin1=-5.00000
xmax1=5.00000
xmin2=-5.00000
xmax2=5.00000
xmin3=-5.00000
xmax3=5.00000
```

Fig. 3. The stabilization of the steady-state

Thus by appropriately choosing Δn and γ we was able to obtain a steady state of system, for the values of the parameters in the chaotic region. This is illustrated in the Figure 3 where $\Delta n=1$ and $\gamma=-0,01$.

CONCLUSIONS

In this work we present numerical evidences of the chaotic behavior in a dynamic model for the mechanism of the reversal of the earth's magnetic field. This behavior can be suppressed by using the G. M. control procedure. The obtained results indicate, at least from a theoretical point of view, that the irregular manner of this reversal could be under control.

REFERENCES

1. T. Coloşi, S. Codreanu, I. Nascu, S. Darie, *Numerical modeling and simulation of dynamical systems*, Ed. Casa Cărții de Şt., 1995.
2. M. F. Danca, doctorthesis, Technical University of Cluj, 1997.
3. E. Lorentz, *Deterministic nonperiodic flow*, I. Atmos, Sci., 20, 130, 1963.
4. R. May, *Simple mathematical models with a very complicated dynamics*, Nature 261, 459, 1976.
5. A. Hübler, G. Reiser, E. Lüscher, *Helv. Phys. Acta*, 60, 226, 1987.
6. E. Ott, C. Grebogi, I. A. Yorke, *Controlling chaos*, Phys. Rev. Lett. 64, 1196, 1990.
7. J. Güémez, M. A. Matías, Phys. Lewtt A 181, 29, 1993.
8. J. Güémez, M. A. Matías, Phys. Rev. E 52, R2145, 1995.

STUDIA UNIVERSITATIS BABES-BOLYAI, PHYSICA, XLII, 2, 1997

CONTRIBUTIONS TO THE STUDY OF THE EXCESS INTERNAL PRESSURE IN BINARY MIXTURES OF ORGANIC LIQUIDS

D. AUSLÄNDER*, I. LENART*, A. CIUPE*

ABSTRACT. Internal pressure is of great importance for the study of the liquid state. In a mixture of liquids, there are deviations of internal pressure from its evaluation based on the additivity of the internal pressure of the component liquids. The excess internal pressure represents the relative measure of the intensity of the interactions between the molecules of different natures of the mixture components, as compared with the intensity of the interactions between identical molecules of the components. The relationships presented in this paper have been verified on the binary systems benzene - carbon tetrachloride, benzene - ethilene dichloride at temperatures ranging from 20°C to 70°C as well as on acetone - chlorophorme and acetone - carbon sulphide at temperatures from 20°C to 50°C.

INTRODUCTION

The internal pressure is defined as the variation of the internal energy with respect to the volume, at a constant temperature. The internal pressure is a consequence of the aggregate intermolecular interactions in liquids. Hence, by evaluating this parameter, one can obtain information about the liquid phase both in the equilibrium state and while certain processes take place.

In a singular liquid, with identical molecules, one assumes the hypothesis of additivity of the internal pressures coresponding to different types of intermolecular interactions according to the properties of the component molecules.

As far as mixtures are concerned, there are deviations of the internal pressure from its evaluation based on the additivity of the internal pressures of the component liquids. These deviations (known as

---

* Department of Physics, Babes-Bolyai University of Cluj-Napoca, Romania

excess internal pressure P_i^E) point out the interactions between the molecules of the system components.

THEORY

The internal pressure in a liquid is defined by

$$P_i = \left(\frac{\partial U}{\partial V}\right)_T \quad (1)$$

and can be written in the following computational form:

$$P_i = \frac{1}{\gamma}\alpha T \rho c^2 \quad (2)$$

here $\gamma = \frac{C_P}{C_V}$, α is the dilatation coefficient of the liquid, ρ is its density, T is the temperature, and c is the propagation velocity of the ultrasound in the corresponding liquid. In the alove formulations, P_i corresponds to the aggregate intermolecular interactions in the considered liquid.

In general, the description of the thermodynamic properties of real mixtures is based on the evaluation of the deviations with respect to ideal systems.

Taking into consideration the internal pressure as a characteristic parameter, the excess internal pressure in a binary mixture is expresed as follows:

$$P_i^E = P_i^{mix} - \left(\chi_1 P_{i(1)} + \chi_2 P_{i(2)}\right) \quad (3)$$

Relation (3) expresses the excess internal pressure, the symbol "mix" indicating the mixture term.

EXPERIMENTAL

Our research was focused on the behaviour of the following systems: C_6H_6-CCl_4, C_6H_6-$C_2H_4Cl_2$, $CO(CH_3)_2$-$CHCl_3$, $CO(CH_3)_2$-CS_2, the intermolecular interactions are differentiated according to the polar or non polar character of the molecules of the component liquids.

The internal pressures of the components and of the mixtures were computed. according to (2), and the excess values according to (3), after determining the quantities in (2) [1], [2], [3].

The values of $\gamma = \frac{c_P}{c_V}$ were obtained from the formula:

$$\gamma = 1 + \frac{M \cdot \alpha^2 c^2 T}{c_P} \tag{4}$$

The measurements were extended to a wide range of concentrations and temperatures.

RESULTS

The obtained data are presented in Table 1. Most mixtures have negative excess internal pressure.

Table 1

T K	Conc.	P_i atm according to (2)	P_i^E atm according to (3)
	χ_{CCl_4}	C_6H_6 - CCl_4	
293	0.2	3680	+ 37
303		3582	+ 31
313		3489	+ 28
323		3389	+ 20
333		3289	+ 4
343		3169	- 27
293	0.4	3602	+ 16
303		3519	+ 28
313		3425	+ 24
323		3329	+ 22
333		3227	+ 5
343		3117	- 14
293	0.6	3515	- 15
303		3427	- 5
313		3342	+ 1
323		3254	+ 9
333		3154	- 5
343		3054	- 12

293	0.8	3447	- 26
303		3352	- 20
313		3272	- 9
323		3178	- 5
333		3081	- 4
343		2982	- 18
	$\chi_{C_2H_4Cl_2}$	C_6H_6 - $C_2H_4Cl_2$	
293	0.2	3756	- 41
303		3674	- 40
313		3595	- 29
323		3492	- 42
333		3399	- 50
343		3301	- 58
293	0.4	3816	- 77
303		3736	- 80
313		3648	- 80
323		3564	- 73
333		3461	- 87
343		3345	- 113
293	0.6	3920	- 70
303		3828	- 92
313		3729	- 101
323		3657	- 83
333		3551	- 98
343		3454	- 102
293	0.8	4022	- 65
303		3959	- 63
313		3871	- 63
323		3779	- 64
333		3679	- 69
343		3566	- 88
	χ_{CHCl_3}	$CO(CH_3)_2$ - $CHCl_3$	
293	0.2	3390	- 27
303		3315	- 2
313		3232	+ 5
323		3128	+ 4
333		-	-
293	0.4	3380	- 85
303		3299	- 74
313		3218	- 67
323		3135	- 53

293	0.6	3420	- 93
303		3366	- 62
313		3288	- 54
323		3205	-47
293	0.8	3554	- 7
303		3470	- 14
313		3376	- 23
323		3285	- 31
	χ_{CS_2}	$CO(CH_3)_2$ - CS_2	
293	0.2	3337	- 113
303		3237	- 112
313		3153	- 107
293	0.4	3423	- 107
303		3287	- 150
313		3195	- 154
293	0.6	3481	- 129
303		3366	- 159
313		3245	- 193
293	0.8	3608	- 84
303		3532	- 81
313		3398	- 131

The increase in temperature has a different effect on the excess internal pressure, depending on the concentration and the properties of the system.

Analysing the data in Table 1, we note the following ordering of the mixtures by increasing excess internal pressure

$$[C_6H_6\text{-}CCl_4] \rightarrow [CO(CH_3)_2\text{-}CHCl_3] \rightarrow [C_6H_6\text{-}C_2H_4Cl_2] \rightarrow [CO(CH_3)_2\text{-}CS_2]$$

To illustrate the above remark, we present the variation of the excess internal pressure of the studied mixtures with respect to concentration, at different temperatures (see fig. 1, 2, 3 and 4).

DISCUSSIONS

The excess thermodynamic parameter of the internal pressure represents the relative measure of the intensity of the interactions between the molecules of different natures of the mixture components, as compared with the intensity of the interactions between identical molecules of the components.

In a binary system, formed by the molecular components of type A as solvent and type B as solute, the internal pressure of the mixture is given by the following relation (by additivity):

$$P_i^{mix} = P_{i(A,B)}^{mix} + P_{i(A,A)}^{mix} + P_{i(B,B)}^{mix}$$

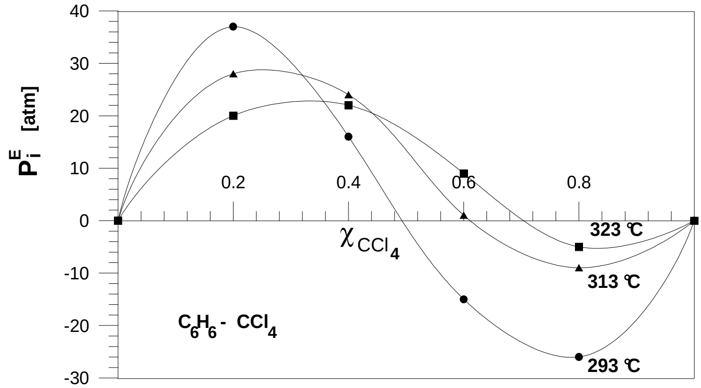

Fig. 1

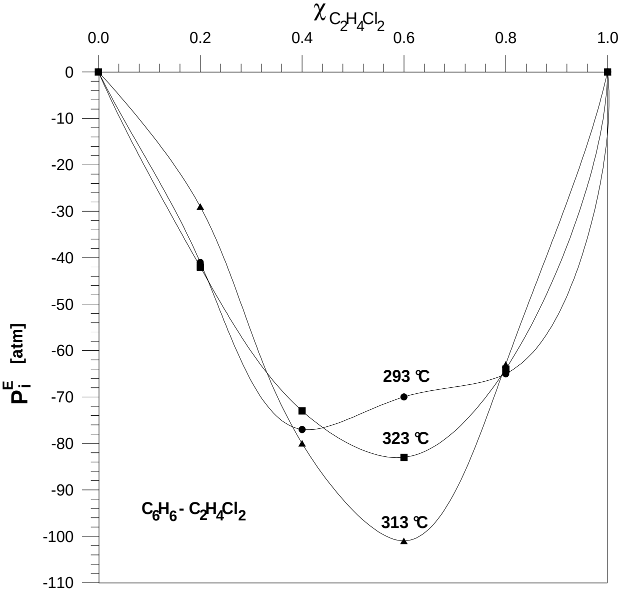

Fig. 2

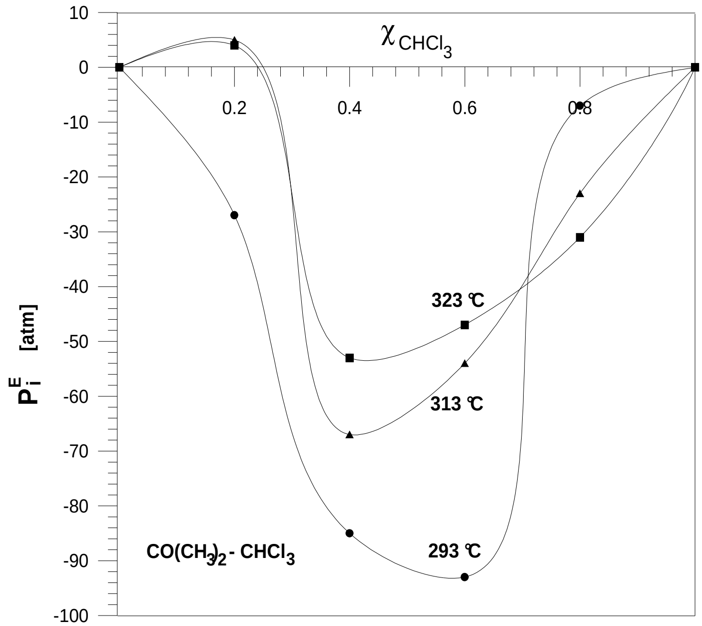

Fig. 3

Thus, (3) becomes

$$P_i^E = P_{i(A,B)}^{mix} + P_{i(A,A)}^{mix} + P_{i(B,B)}^{mix} - \left(P_{i(A,A)}^{id} + P_{i(B,B)}^{id}\right)$$

or

$$P_i^E = P_{i(A,B)}^{mix} - \Delta P_{i(A,A+B,B)}^{id-mix} \qquad (5)$$

here the first term in the right-hand side represents the internal pressure corresponding to the mixed interactions in the mixture, and the second term the modification of the internal pressure of the ideal mixture (due to mixing). The interactions between the molecules of the two components arise by partial annihilation of the interactions between identical melecules, whence $\Delta P_i > 0$.

The formation of a mixture is accompanied by two phenomena:
1) the decrease of the molecular density of the components, by the distribution of the molecules in the volume of the mixture and that of the preexistent internal pressures in the component liquids.

2) the reciprocal screening of molecules A and B determined by the homogeneization of the systems and hence the limitation of the number of molecules taking part in interactions of type $(A,A)^{mix}$ and $(B,B)^{mix}$.

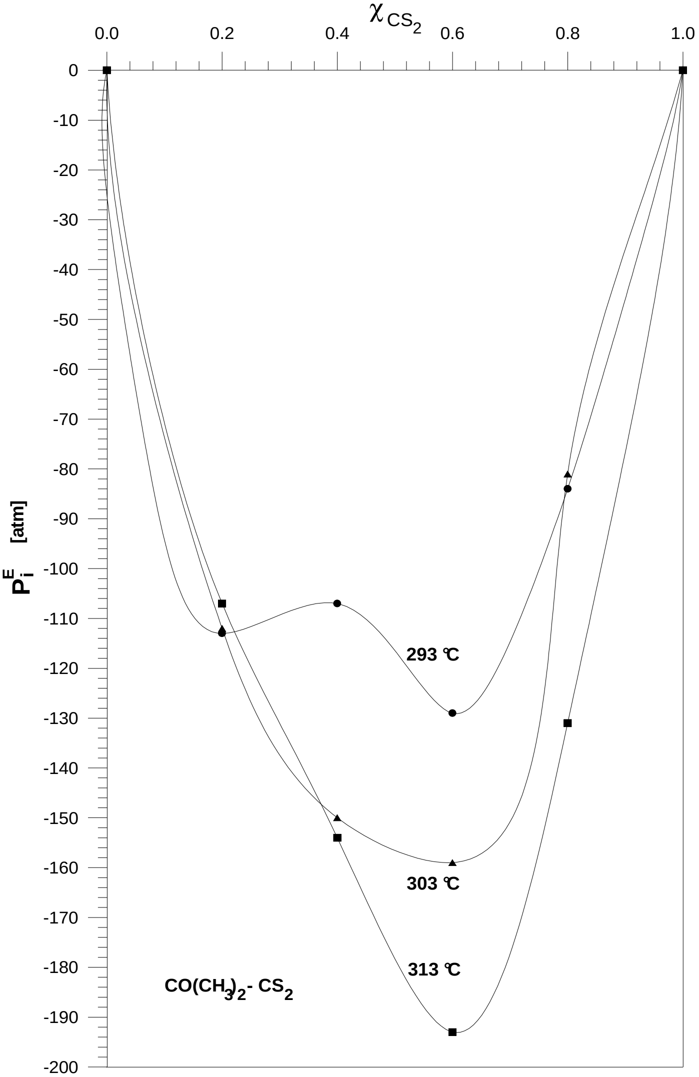

Fig. 4

Both mechanisms favour the increase of $P_{i(A,B)}^{mix}$ and the decrease of the internal pressures $P_{i(A,A)}^{mix}$ and $P_{i(B,B)}^{mix}$ thus contributing to the increase of the difference ΔP_i.

The intensity of the mentioned effects decrease with the increase in the concentration of each component in part, being at the some time amplified by the increase of the number of molecules taking part in interactions.

Taking into account the nonpolar character of the component molecules, the system C_6H_6-CCl_4 evolves with respect to concentration under the influence of the dispersion interactions. It was observed the presence of a positive excess up to χ_{CCl_4} equal to approximately 0.5; in this range, the internal pressure $P_{i(A\beta)}^{mix}$ dominates DP_i. For values of the concentration greater than 0.5, the excess is negative and the term DP_i dominates.

In the two intervals there is a maximum at $\chi_{CCl_4} = 0.2$ and a minimum at $\chi_{CCl_4} = 0.8$. In order to improve the phenomenological interpretation of the curve obtained from experimental data, $P_i^E = f(\chi_{CCl_4})$ have to assume the hypothesis of formation in the system of certain molecular complexes, which determines the decrease of P_i^E with $P_{i(A,B)}^{compl.}$.

Hence, (5) becomes

$$P_i^E = P_{i(A,B)}^{mix} - P_{i(A,B)}^{compl.} - \Delta P_i \tag{6}$$

In consequence, the increase of P_i^E is slowed in the first interval, and we have a reduced maximum at the concentration $\chi = 0.2$. Then, the decrease of P_i^E becomes more prominent due to the increase with concentration of the last two terms in (6). One obtains P_i^E =0 for

$$P_i^{mix} = P_{i(A,B)}^{compl.} + \Delta P_i \tag{7}$$

As the concentration increases, the excess pressure decreases more rapidly due to the dominance of the contribution of the last two terms in (6), until a minimum is reached; then all the terms decrease to zero.

The validity of the model is confirmed by the data obtained by ultraviolet spectroscopy, observing the formation of a molecular complex in the mixture C_6H_6-CCl_4. It was observed that the mixing process is accompanied by a volume contraction of 0.13 % [4], [5].

The other three systems are characterized by strong interactions emphasized by $P_i^E < 0$ in the entire concentration range, with a minimum at approximately $\chi = 0.5$. The terms $P_{i(A,B)}^{compl.}$ and ΔP_i give the predominant contribution to the variation of the excess of the internal pressure with respect to concentration. In the mixture C_6H_6-$C_2H_4Cl_2$, the molecules of $C_2H_4Cl_2$ are subject to orientation interactions of isomers with dipol-moment different from zero. Thus induction interactions arise between the molecules of C_6H_6 with high polarizability and the molecules of $C_2H_4Cl_2$.

The excess internal pressure in the system $CO(CH_3)_2$ -$CHCl_3$, formed by molecules with dipolmoment $\mu_{CO(CH_3)_2} = 2.88D$, respectively $\mu_{CHCl_3} = 1.02D$ reflects the presence of intermolecular interactions by hydrogen bounding [6]. It was observed the presence of a volume concentration of 0.23 % upon mixing [4].

The variation of the excess internal pressure with concentration in the system $CO(CH_3)_2$ - CS_2 has a maximum value with respect to the presented mixtures. This indicates the formation of certain compounds from the molecules of the components [7].

The increase of temperature has a different effect on the intermolecular interactions in the mixture. The global effect depends on the ratio of the degrees in which the pressures coresponding to the terms determining the value of the excess pressure are affected.

In general, we note the decrease of P_i^E in the positive range, with the increase of temperature, and a tendency of inverse variation of the negative excess with the exception of the system $CO(CH_3)_2$ - $CHCl_3$.

By intensifying the vibrational effect, the increase of temperature determines the decrease of the internal pressure coresponding to the interactions $(A,B)^{mix}$, $(A,A+B,B)^{id}$ and $(A,A+B,B)^{mix}$. The structural component has the same effect on the internal pressure of the interaction $(A,B)^{compl.}$.

The vibrational effect influences the interactions $(A,A)^{mix}$ and $(B,B)^{mix}$ the some direction as the decrease of the molecular density and the screening at the formation of the mixture.

The increase of the temperature determines a more prominent decrease of the internal pressure coresponding to the types $(A,A+B,B)^{ed.}$ as compared to the internal pressure of the types $(A,A+B,B)^{mix}$. This contributes to the decrease of ΔP_i with respect to temperature.

Since the interactions of the molecular compounds are stronger than the other interactions know as week interaction, one can assume that the formation of the complexes influences the interactions of type $(A,B)^{mix}$.

Consequently, the increase of $P_{i(A,B)}^{compl.}$ with concentration slows the increase of $P_{i(A,B)}^{mix}$, which evolves slower, as well as the increase of ΔP_i ; thus, the effect of ΔP_i , which modifies the sense of variation of P_i^E, takes place at higher concentration than that corresponding to the maximum.

Correspondingly, the condition $P_i^E = 0$ will hold for concentration which increase with the temperature. Obviously, in this way, the values of P_i^{max} decrease with temperature.

The decrease of the slope of P_i^E between the maximum and the minimum is determined by the slower and slower increase of ΔP_i with concentration while the temperature increases; the interval corresponds to the maximum value of $P_{i(A,B)}^{compl.}$. According to the mechanisms of the proposed model, the values of the minimal of P_i^E decrease with temperature, and appear at concentrations which increase with temperature.

For example, to an increase in temperature from 293 K to 333 K corresponds a decrease of the maximum value of P_i^E from 37 atm to 4 atm and a modification of the minimum value from -15 atm to -5 atm.

Since the least affected term by the increase of temperature is $p_{i(A,B)}^{compl.}$ this amplifies the predominant character with respect to the other internal pressure, until the appearance of a negative excess of the internal pressure in the entire concentration range.

In the system C_6H_6-$C_2H_4Cl_2$, the variation with temperature of the excess internal pressure is relatively insignificant with respect to the variation with concentration.

In the system $CO(CH_3)_2$ - $CHCl_3$ these is a decrease of p_i^E with temperature due to the decrease of the percentage of hydrogen bonds.

REFERENCES

1. Ausländer D., Lenart I., Ciupe A., Studia Univ. Babes-Bolyai, Physica, XXXVII, 2, 1992, 103.
2. Lenart I., Ciupe A., Ausländer D., Caietul de Acustica al Academiei Române nr. 24, 1994, 147.
3. Ausländer D., Lenart I., Ciupe A., Acustica, 81, 1995, 71.
4. Murgulescu I. G., Segal E., Introducere în chimia fizica, vol. II, 1, Bucuresti, 1979.
5. Mishra R. L., Pandey J. D., Acustica, 36, 1977, 342.
6. Stavely L. A. K., Tupman W. I., Hart K. R., Trans. Farad. Soc., 51, 1955, 323.
7. Low D. I. R., Moelwyn-Hughes E. A., Proc. Roy. Soc., London, 267A, 1962, 384.